Nanostructural Engineering of Optical Interfero-metric Biosensors Based on Nanoporous Anodic Alumina

Gerard Macias Sotuela

Dipòsit Legal: T 772-2015

Gerard Macias Sotuela

Nanostructural Engineering of Optical Interfero-metric Biosensors Based on Nanoporous Anodic Alumina

Ph.D. Thesis

Supervised by:

Prof. Lluís Francesc Marsal Garví

Departament d'Enginyeria Electrònica Elèctrica i Automàtica

Nanoelectronic and Photonic Systems (NePhoS)

UNIVERSITAT ROVIRA I VIRGILI

Tarragona

2015

UNIVERSITAT ROVIRA I VIRGILI

Departament d'Enginyeria Electrònica Elèctrica i Automàtica

Escola Tècnica Superior d'Enginyeria

Avda. Països Catalans, 26

43007 Tarragona, Spain

Phone: +34 977 55 96 10

Fax: +34 977 55 96 05

I STATE that the present study, entitled "Nanostructural Engineering of Optical Interferometric Biosensors Based on Nanoporous anodic Alumina", presented by Gerard Macias Sotuela for the award of the degree of Doctor, has been carried out under my supervision at the Department of Electrical, Electronic and Automatic Control Engineering of this University, and that it fulfills all the requirements to be eligible for the International Doctorate Award.

Tarragona, 3rd of February 2015.

Doctoral Thesis Supervisor

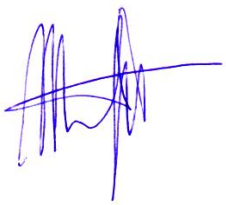

Prof. Lluís F. Marsal Garví

ACKNOWLEDGEMENTS

Becoming a Doctor is pretty much like an adventure. From day one of this fascinating journey you are pushed away from your comfort zone. Trying to expand the limits of human knowledge is not an easy task. It requires a great deal of hard work, time, discussions and imagination to try to innovate in the competitive world of science. Luckily, you are never alone in this trip. As the time passes by, you meet a lot of people. And with time, you discover how some of them have been crucial during the Ph.D. studentship. Thanks to them, the work presented in this Ph.D. thesis has been possible and I would like to express them my gratitude.

First of all, I would like to thank my supervisor, Prof. Lluís F. Marsal, for without his support, advices and guidance this Ph.D. thesis would have been impossible. I would like acknowledge also the financial support of Universitat Rovira i Virgili, which allowed me to pursue my Ph.D.

I would also like to express my gratitude to Dr. Abel Santos for instructing me into the amazing world of nanoporous anodic alumina. Thanks also to Dr. Pilar Formentín for helping me out with the chemistry issues during the beginning of my studentship. And also, special thanks to Dr. Josep Ferré-Borrull for his help with the optical setups and his constructive comments on my work.

To my colleagues of the NePhoS group, former and present, thank you for your kindness and the good vibes throughout these years, especially

to my contemporary Ph.D. student fellows Maria A., Pedro G., Victor B., and Peilin H. We spent two wonderful years in lab 332. I enjoyed every single day, sharing ideas, discussing results and performing the sacred ritual of coffee break. Coffee time is not going to be the same without you anymore. Thanks also to my colleagues from lab 235 Maria P., Fetene M. and François L. with whom I shared office during the last year of my Ph.D.

I am grateful also to Dr. Frédérique Cunin, for giving me the opportunity of working in her facilities during the three months I spent in Montpellier. During my contribution to the project of pSi microparticles for bone regeneration, not only did I broaden my knowledge on electrochemically etched nanomaterials, but also on surface chemistry modification, and several characterization techniques which I will definitely use in my future works if they are available. Thanks also to Dr. Jean-Olivier Durand for helping with the functionalization of pSi, and also to the colleagues from the dentistry department Dr. Frédéric Cuisiner, Matthieu R. and Pierre-Yves for the in vivo and in vitro experiments. Especial thanks to Arnaud C. for showing me how to fabricate pSi micro and nanoparticles and showing me the functionalization processes. I cannot forget all the people from the MACS lab who made my stage very pleasant and helped me with my French. Arnaud, Bilel, Champs, Carl and Zhu Yang, thank you for those afternoons playing Imperial, and thank you Mayra, for you allowed my brain to rest every now and then from the effort of pattering in French.

To the people from the Microscopy Department of the Servei de Recursos Científics i Tècnics (SRCiT), for without them most of the work presented here would have never been possible, thank you. Lukas,

Mercè, Mariana and Rita, thanks for teaching me how to use the SEM and your advice on how to take better pictures.

Finally, I would like to thank my parents, for they are a source of unconditional love, support, faith and trust throughout all my life. And to Marina, for you are my best friend, my lover and my safe place. Thank you for being by my side throughout all these years, helping me, supporting me, encouraging me and believing in me.

"The most exciting phrase to hear in science, the one that heralds new discoveries, is not 'Eureka!' but 'That's funny…'."

Isaac Asimov

"The important thing is not to stop questioning.

Curiosity has its own reason for existing."

Albert Einstein

CONTENTS

Contents

Contents

Contents

CHAPTER I

INTRODUCTION

1.1. BACKGROUND

The recent rise of technological methods for structuring materials at the nanoscale has attracted much interest in the scientific community. The ability to modify matter at the nanometer level has opened scientist the possibility to develop and study nanomaterials which, due to their nanostructural features display new exotic effects.

Even though nanotechnology is here, real life applications are still to be developed. One particular field in which nanotechnology may play a major role in future discoveries is biology. The complex reactions that make life possible consist in physico-chemical interactions occurring at the nanoscale level. Therefore, the ability to control both the structure and the chemical features of materials in the nanoscopic range is of great interest in biomedical applications such as drug delivery, tissue engineering or biosensing.

From the applications mentioned, biosensing is especially interesting for its tremendous possibilities. The first biosensor developed, the glucose biosensor, revolutionized medicine by providing diabetic patients the possibility to gain some control over their condition with a simple test that allowed them to monitor their glucose level throughout the day and adjust insulin dosage accordingly. The great success of this first biosensor has resulted in a great commercial market for these devices that is expected to exceed 14000 million USD in the following years. From this first glucose sensor, research on biosensing has advanced significantly and has broadened the applications of the biosensors developed beyond point-of-care devices. Nowadays, scientific works in which biosensors are present include diverse topics such as cellular interaction studies or drug discovery.

The application of novel nanostructuring methods to existing biosensing techniques show promising results in the development of more sensitive and smaller devices which may revolutionize once again the biomedical industry.

1.2. OBJECTIVES

The main aim of this thesis consists in the development of optical biosensors which are able to detect the analyte of interest by monitoring the interferometric pattern arising from the phase difference between the top and bottom reflection occurring when a nanostructured transparent thin film is illuminated with white light.

For this purpose, nanoporous anodic alumina (NAA) was used as the thin film. Therefore, the first objective during the course of this Ph.D. was to understand the fabrication procedure for thin films of NAA and establish a stable and repeatable protocol based on self-ordered pore arrays.

Another important objective was to learn, understand and perform an appropriate characterization for the NAA thin films. The main core of the characterization techniques used throughout this Ph.D. thesis consists mainly on scanning electron microscopy (SEM) picture analysis as well as optical characterization such as reflectometry and transmission spectroscopy in the UV-Vis-NIR or photoluminescenc spectroscopy.

Apart from these two objectives presented, the development, testing and optimization of innovative optical interferometric structures based on NAA for biosensing purposes were the main goals. To fulfill this ambition, three struc-

tures were studied during the Ph.D. studentship: monolayers, double layers, and 1-D photonic crystals (rugate filters).

1.3. STRUCTURE OF THE THESIS

The following chapters of this Ph.D. thesis are organized as follows:

Chapter II presents the main concepts of biosensing. After a brief historical introduction highlighting the main breakthroughs in the field and the ideal composition of a biosensing device, the most common techniques used for the detection of biochemical interaction events are presented. Finally, the basic theory regarding biosensing as well as the main applications of biosensor devices in recent years are discussed.

Chapter III is second introductory chapter dedicated to NAA. The history of anodic alumina is detailed as well as the most common fabrication procedures. Apart from that, structural characterization with SEM as well as optical characterization by means of reflectance and photoluminescence spectroscopy are presented in order to outline the optical properties of NAA and its correlation with the nanoscopic features.

Chapter IV shows all the work made during the Ph.D. related with NAA thin monolayer films. The basics of RIfS biosensing using NAA single layers are explained, along with the key features that can be used to tune the optical properties of the thin film. Finally, an optimization study of the NAA structure is presented theoretically along with an experimental validation of one of the most crucial parameters: the pore diameter.

Chapter V shows the work related with NAA double layers. The principle of action of double layer biosensors with the ability to self-referenciate, and the data processing algorithm used are explained in detail. An optimal NAA double layer interferometer structure based on size exclusion self-referenciation is proposed based on the knowledge presented in chapter IV and experimental results from NAA double layers manufactured under different conditions. Finally, the proposed structure was tested to assess its size exclusion performance and the results are discussed.

Chapter VI presents an innovative NAA photonic structure: the rugate filter. Some of the basic details on how photonic crystals work are presented as an introduction. Also, the fabrication procedure developed is explained and the critical parameters involved in the performance of the reflection band arising from the multilayered structure are studied. Finally, one rugate filter structure is tested to assess its sensing possibilities and an optimum rugate filter structure is proposed.

Finally, Chapter VII closes the Ph.D. thesis by briefly summarizing all the work done and making some concluding remarks.

CHAPTER II

BIOSENSING FUNDAMENTALS

2.1. HISTORY OF BIOSENSING

The amazing field of biosensors started back in the 1950s by the hand of Leland C. Clark with the invention of the oxygen electrode [1]. This electrode measured oxygen concentration on a catalytic platinum surface by the following reaction:

$$O_2 + 4e^- + 2H_2O \rightarrow 4(OH)^- \quad (2.1)$$

With this electrode, Clark intended to monitor and control oxygen concentration in blood and tissues. The device consisted in a platinum working electrode and a silver counter electrode immersed in a saturated potassium chloride solution. Oxygen from the patient would diffuse through a semipermeable membrane by osmosis thus producing a shift in the current measured.

About a decade later, Clark and Lyons wanted to broaden the applications of the oxygen electrode and develop "smart" sensors. To achieve this goal, they proposed the use of enzymes in order to give the electrochemical sensors a selective response. The idea was exemplified by entrapping glucose oxidase (GOx) in the semipermeable membrane of the oxygen electrode. The resulting device responded to glucose according to the following reaction:

$$C_6H_{12}O_6 + O_2 + H_2O \underset{GOx}{\rightarrow} H_2O_2 + C_6H_{12}O_7 \quad (2.2)$$

The enzymatic oxidation of glucose into gluconic acid resulted in a decrease of the oxygen concentration that could be detected with a Clark's oxygen electrode [2]. The first biosensor was invented.

In 1970, Bergveld developed the first ion-sensitive field-effect transistor (ISFET) [3]. Charge detection in ISFET transistors was based on metal-oxide-

semiconductor field-effect transistors (MOSFET). MOSFETs are devices consisting on a silicon substrate with two terminals for the source and drain of electrons, and an insulating oxide on top of them. In MOSFETs, the insulating oxide is covered with a metal that acts as a gate. When a potential is applied to this gate, it will induce a conducting channel in the silicon which can be measured as a resistance between the source and the drain. However, the ISFET had no metal to act as a gate. Instead, the channel was induced by the oxide charge of the silicon dioxide insulator. When the ISFET is immersed in an aqueous solution, the silicon dioxide will hydrate and the induced conducting channel will depend on the ion activity in the solution adjacent to the oxide. This structure was proved for the detection of NaCl at a fixed pH of 4.6. The results showed a linear dependency between the current in the drain (ID) and the molarity of the NaCl solution, thus proving the concept.

The same year, Guilbault and Montalvo developed the first potentiometric biosensor [4]. It consisted on a thin film of urease immobilized in acrylamide gel deposited on top of an ammonium sensitive electrode. Urease catalyzed the decomposition of urea into ammonium, which was detected by the electrode. The results showed that the steady-state potential developed by the electrode was proportional to the logarithm of the urea concentration.

In 1974, Mosbach and Danielsson report the first heat-sensitive biosensor [5]. When an enzyme meets its specific substrate and the catalytic reaction occurs, heat is produced. Based on this concept, Mosbach and Danielsson developed their heat-sensitive biosensor. This biosensor consisted on a thermistor coated with a thin layer of a selective enzyme to ensure the closest distance between the heating source and the detector. As expected, the results showed a clear relationship between the temperature measured by the biofunctionalized thermistor and the amount of substrate in the solution.

One year later, Diviés designed the first "microbial" electrode [6]. In this work, an oxygen electrode was modified with a cellulosic pellicle of *Gluconacetobacter xylinus* (formerly known as *Acetobacter xylinum*). The results showed that this "microbial" electrode was able to detect ethanol at concentrations below 0.4 mM within a pH range between 2.5 and 7.

At the same time, Lubbers and Opitz coined the term "optode" with their work in the optical detection of pO_2/pCO_2 [7]. In this work, O_2 and CO_2 pressures were determined by changes in the fluorescent signals of pyrene butyric acid and beta-methylumbelliferone respectively. The fluorescent labels were separated from the measuring medium by a gas permeable membrane. The results showed a linear response in the range between 10-70 Torr for pCO_2 and between 0 and 300 Torr for pO_2 with a response time of 3 s.

One of the most important breakthroughs in optical biosensing occurred in 1983. This year, Liedberg et al. developed the first surface plasmon resonance (SPR) biosensor [8]. The experiment consisted in a thin film of silver deposited on top of a microscope slide and embedded in a flow cell with a chamber height of 2 mm. With this setup, Liedberg et al. flowed the antigen, in this case an immunoglobulin G (IgG) and after a washing step, the antibody was flowed into the cell (a-IgG). The results showed a shift in the position of the SPR as a result of biomolecule dosing. With this simple setup a-IgG was possible to be detected at concentrations down to 2 $\mu g \cdot ml^{-1}$.

Further improvements in the area of glucose biosensing came in 1984. Cass et al. improved the glucose sensor concept by the use of electron mediators [9]. Previous glucose sensors based on the oxygen electrode were sensible to oxygen concentration in blood and samples had to be treated with oxygen saturated buffers prior to measurements. Electron mediators avoid this problem. In this work, Cass et al. coated a graphite electrode with a thin layer of 1,1'-

dimethylferrocene and immobilized glucose oxidase on top of it. In order to produce the ferrocinium ion needed for electron mediation between the redox center of the enzyme and the electrode, a potential of 160 mV had to be applied. The results showed a linear response between 1-30 mM of glucose.

In the late 1980s, Gauglitz and Krausse-Bonte reported the use of interference refractometry for the development of high-performance liquid chromatography sensors [10]. In their article, the theoretical basis of interference refractometry is explained and real-time measurements of the refractive index dispersion of water showed the possibility of measuring changes in refractive index units (RIU) lower than 0.00008 RIU.

Table 1.1. Historical breakthroughs in biosensing.

Year	Historical advancement
1956	Clark L. C. develops the oxygen electrode (Clark's electrode).
1962	Clark L. C. reports the first amperometric biosensor for the detection of glucose using a modified Clark's electrode
1970	Bergveld P. develops the first ion-sensitive field-effect transistor (ISFET) for measurements of ion activities in biological environments
1970	Guilbault and Montalvo develop the first potentiometric biosensor for the detection of urea
1974	Mosbach and Danielsson report the first heat-sensitive enzyme sensor (thermistor)
1975	Divis develops the first microbial sensor for the detection of alcohol
1975	Lubbers and Opitz develop the first optical biosensor (optode) for the measurement of pCO_2/pO_2
1983	Liedberg et al. develop the first surface plasmon resonance (SPR) biosensor based on biomolecular affinity
1984	Cass et al. report the first direct interaction between the redox centre of glucose oxidase and the electrode
1988	Gauglitz and Krause-Bonte report the basics of the reflectometric interference spectroscopy (RIfS)

2.2. WHAT IS A BIOSENSOR?

2.2.1. DEFINITION OF BIOSENSOR

The international union of pure and applied chemistry (IUPAC) defines biosensor as follows [11]:

"A device that uses specific biochemical reactions mediated by isolated enzymes, immunosystems, tissues, organelles or whole cells to detect chemical compounds usually by electrical, thermal or optical signals."

2.2.2. PARTS OF A BIOSENSOR

A biosensor is composed of the following parts:

Recognition element: a molecule that specifically reacts with the target analyte. Some examples of recognition elements would be DNA, antibodies, antigens, enzymes and aptamers.

Biosensor surface: surface to which the recognition element is attached. Adequate selection of the material for the biosensor surface is of critical importance as it can limit the available chemical methods to attach the recognition element as well as define the detection strategy.

Transducer: sensing mechanism that will transform the biochemical interaction between the target analyte and the recognition element present in the sensing surface into a readable signal (electronic signal). This transduction is normally electrical, mechanical, optical or calorimetrical.

Signal processing package: software with a specific algorithm that is able to monitor the signal obtained by the transducer and transform it into the response of the biosensor.

Display: user interface that shows the result of detection of the target analyte displaying its concentration.

A schematic representation of the components of a biosensor is shown in figure 2.1.

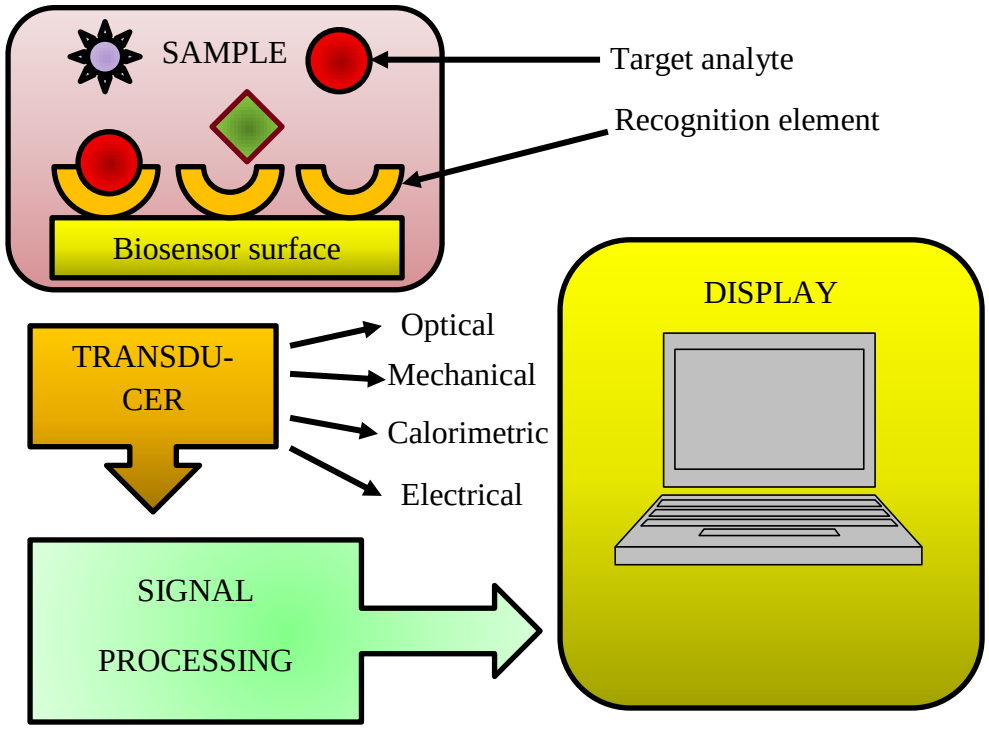

Figure 2.1. Schematic representation of the components of a biosensor. Note that the possible transducers depicted here are not the only ones available, but the most common.

2.2.3. TYPES OF BIOSENSORS

Biosensors may be divided according to either the biochemical interaction on which they are based or in the detection method used.

Biochemical interaction

Catalytic reaction

This kind of biosensors was the first to be developed. They use enzymes that cleave the target analyte (commonly known in this case as substrate) as the recognition element. They are designed to, instead of detecting the analyte, sense the concentration of either:

a) One of the byproducts of the enzyme-based catalysis.

An example would be the urea biosensor [4]. As explained in section 2.1, this biosensor consists of a urease-modified ammonia-selective electrode. When urease meets its substrate (urea) the following reaction occurs:

$$(NH_2)_2CO + H_2O \xrightarrow[urease]{} CO_2 + 2NH_3 \qquad (2.3)$$

The ammonia resulting from urease activity is measured by the ammonia-selective electrode and the response correlates with the amount of urea present in the sample.

b) One of the reagents required for the enzymatic reaction.

This is the case of the glucose biosensor developed by Clark and Lyons based on a GOx-modified oxygen-specific electrode [2]. As it can be observed in equation 2.2, glucose oxidase activity requires oxygen. As a result of the reaction, oxygen concentration in the sample diminishes. This reduction in oxygen concentration is measured by the electrode and correlates with the amount of glucose in the sample.

c) Amount of electrons mediated.

Electronic enzymatic biosensors may use an intermediate layer between the enzyme and the electrode that acts as an electron mediator between the enzyme's redox center and the electrode [9]. In this method, when the enzymatic reaction takes place, this intermediate layer transfers electrons from the enxyme to the electrode producing an increase in the current measured which can be used to detect the analyte concentration. Nowadays, this method is the most used for glucose biosensors as it avoids the necessity of pretreating the sample with oxygen-saturated solutions to eliminate background.

Affinity reaction

Affinity-based biosensors rely on the tendency of two substances A and B to form a compound AB. This reaction is reversible and the strength of the binding of the two substances is governed by its dissociation constant (K_D) as explained in eq.2.4:

$$A + B \overset{K_D}{\leftrightarrow} AB \qquad (2.4)$$

This is the case of biosensors based on antigens, antibodies, DNA and aptamers.

Detection method

Biosensors can also be categorized depending on their principle of action.

Electrical

Electrical biosensors rely on measurements of the electrical properties of the sensor surface (i.e. voltage, current, resistance and capacitance). The major advantages of electrical biosensors are their low cost, low power consumption and ease of miniaturization. The sensitivity of electrical biosensors is inferior to other techniques (such as optical techniques), but sufficient for most applications, especially when small instruments are required [12]. Depending on their principle of action, electrical biosensors can be defined as:

a) Potentiometric

This kind of biosensor is based on measurements of the potential difference between two electrodes: a reference electrode and a biofunctionalized electrode. When the biofunctionalized electrode meets its specific analyte, a shift in the voltage measured is detected and correlated with the concentration of the analyte. The transducers are typically ion-selective electrodes [13]. Several approaches have been used lately to improve this kind of biosensors including

electrode nanostructuring [14], nanoparticle-coated electrodes [15], graphene electrodes [16], recombinant enzymes [17] to name a few.

b) Amperometric

Amperometric biosensors were the first biosensors to be developed [2]. This kind of biosensors measure electron transport processes. The signal from these biosensors comes from a biochemical reaction that is involved in a redox reaction that can be monitored using an electrochemical cell. For this reason, the vast majority of amperometric biosensors are enzyme-based [18]. They normally work in a three electrode configuration (working, counter and reference) and measure the shifts in current upon biochemical reaction between the analyte and the recognition element immobilized in the working electrode. Recent studies on amperometric biosensing have been focused on improving the working electrode by using new materials such as carbon nanotubes [19] and nanoparticles [20] as well as exploring new enzyme immobilization techniques such as layer-by-layer (LbL) [21].

c) Conductometric/impedimetric

Contrary to amperometric and potentiometric biosensors in which work under DC conditions, conductometric/impedimetric biosensors work under AC conditions in order to extract the impedance/conductance of the electrodes [12]. They work with interdigitated electrodes but due to the parallel conductance of the sample solution, differential measurement with a second non-biofunctionalized impedimetric sensor is required [13]. Recent works related to impedimetric biosensors try to increase its sensitivity using a variety of methods such as nanoparticle deposition on top of the electrode [22], graphene oxide as

the electrode material [23], nanostructuring of the electrode [24] or protein separation using magnetic beads [25].

d) Capacitive

Another possibility for developing AC biosensors is by means of capacitance measurements. The simplest form of a capacitor consists in two metallic plates separated by a dielectric and its total capacitance is given by eq. 2.5.

$$C = \varepsilon_r \varepsilon_0 \frac{A}{d} \qquad (2.5)$$

Where ε_r is the relative permittivity of the dielectric material, ε_0 is the permittivity of vacuum, A is the area of the metallic plates and d is the distance between the two plates.

There exist two types of capacitance biosensors [26]:

i. Electrode-solution capacitors:

In this kind of capacitive biosensors, the working electrode is functionalized with the recognition element while the counter remains unaltered. In this case, each of the layers adhering to the working electrode can act as a capacitive layer. Thus, the binding of the analyte to the receptor results in an additional capacitive layer that increases the total capacitance [27].

ii. Interdigitate electrodes (IDE):

This kind of capacitive biosensor measures differences in the dielectric constant of the medium between the electrodes. This kind of capacitive biosensor has grown interest in the past few years. Compared to the electrode-solution configuration, IDE have a higher surface area for analyte binding. In order to reduce faradaic currents between the electrodes and provide an appropriate surface for biofunctionalization, IDE are typically covered by a thin insulating layer [26]. Current advances in IDE capacitive biosensors include the use of nanoparticles [28] and the development of new surface biofunctionalization techniques such as molecularly imprinted polymers [29].

Mechanical

Mechanical biosensors detect changes in the mass of the sensing surface. They do so by measuring the displacement or vibrational state of the sensing element by electric means. For this reason, mechanical biosensors are often referred to as electromechanical biosensors. Below, we discuss the three main approaches that have been developed for electromechanical biosensing [30].

a) Quartz crystal microbalance (QCM):

QCM biosensors consist of a quartz crystal disk with piezoelectric behavior and two metal contacts on opposite faces. When an alternating electric field is applied to a piezoelectric material, a transverse vibrational wave is generated. The resonant frequency of the wave is linearly related with the mass of the crystal as explained in eq. 2.6:

$$\Delta f_L = -\frac{2f_0^2}{A\sqrt{\rho_q \mu_q}}\Delta m = -S_f \Delta m \quad (2.6)$$

Where Δf_L is the measured shift in resonant frequency, f_0 is the original resonant frequency (i.e. the intrinsic crystal resonant frequency), Δm is the added mass, A is the area of the crystal, ρ_q is the density and μ_q the shear modulus of quartz and S_f is the sensitivity of the system.

Recent works regarding QCM biosensors try to improve their sensitivity by growing nanorods on top of the sensing surface [31], enhance its sensitivity by gold nanoparticle post-treatments [32], and explore new functionalization routes such as lipid-based methods [33] or molecularly imprinted polymers [34].

b) Surface acoustic wave (SAW)

SAW biosensors consist of two pairs of IDE, one working as an emitter and the other working as a receiver, separated by a piezoelectric material that will act as the biosensing surface. When an alternating electric field is applied to the transmitter pair, a periodic surface strain is generated and a surface acoustic wave is created. The frequency of this SAW is given by eq. 2.7:

$$f = \frac{v_p}{d} \quad (2.7)$$

Where f is the frequency, v_p is the propagation velocity of the SAW and d is the distance between the IDEs.

When the analyte binds the receptor attached to the piezoelectric material, the mass increment causes a decrease in the frequency of the SAW.

Current work on SAW biosensors focused on nanostructuring the surface to achieve higher surface area for analyte binding [35], work under SAW-induced

droplet streaming to prevent biofouling due to nonspecific binding [36], use ZnO instead of quartz as the piezoelectric material to enhance the micro and nanostructural possibilities of the sensing area [37], and nanostructure surface functionalization to obtain more sensitive surfaces thanks to the equal spacing between receptor molecules [38].

c) Cantilever

Cantilever-based mechanical biosensors appeared in the 1990s as an evolution of atomic force microscopy (AFM) tips for chemical and biochemical detection. Similarly to AFM tips for non-conductive samples, they can work in two different modes.

i. Bending mode

The bending mode (also known as static-mode) is homologous to AFM contact mode and measures the deflection of a beam upon analyte binding. This deflection is produced by the mass of the analyte binding to the beam producing a differential surface stress. The deflection of the cantilever can be calculated by eq. 2.8:

$$\Delta z = \frac{3l^2(1-\upsilon)}{Et^2}\Delta\sigma \qquad (2.8)$$

Where Δz is the deflection, l is the length of the cantilever, υ is Poisson coefficient, E is Young's modulus, t is the thickness of the cantilever and Δσ is the differential surface stress.

In order to measure cantilever deflection, various methods have been used including optical (optical lever, interferometry) as well as electrical (piezoelectric, impedance and capacitance) techniques. Recent works report improvements in bending-mode cantilever biosensors by means of novel approaches such as the use of magnetic nanoparticles [39] or screen printed single stranded peptide nucleic acids (ssPNA)[40].

ii. Resonant mode

Cantilevers working under resonant mode conditions are homologous to AFM tips working in non-contact mode. These biosensors require an external force to make the cantilever vibrate at its resonance frequency. Upon analyte binding, the biosensors resonance frequency decreases due to the added mass as explained in eq. 2.9:

$$\Delta m = \frac{\frac{3EI_Z}{L^3}}{4\pi^2}\left(\frac{1}{f_m^2} - \frac{1}{f_0^2}\right) \tag{2.9}$$

Where Δm is the increment in mass, E is the Young's modulus, I_z is the moment of inertia, L is the length of the cantilever and f_0 and f_m are the resonance frequencies before and after analyte binding respectively.

The main disadvantage of this kind of biosensors is the reduction of its quality factor (Q-factor) in liquid due to viscous drag force which commonly results in complex drying steps after analyte uptake. Nevertheless, real-time measurements in liquid have been reported successfully which enables the study of biomolecular reactions with dynamic-mode cantilever biosensors [41]. Lately, various novel approaches have been reported for dynamic-mode cantilevers including the use of bioprinted myotubes as the actuators for the cantilever vibration

[42] and electrokinetical adsorption of analytes onto the cantilever for improved detection [43].

Optical

Optical biosensors can be divided into three categories depending on their mode of action namely fluorescence, microrefractometry and microreflectometry [44]. This kind of biosensors are very interesting due to their inherent advantages such as stability in aggressive environments, multiplexing and miniaturization potential and, specially, their high immunity to electromagnetic (EM) interferences [45].

a) Fluorescence

This was the first technique to be developed. It consists in attaching a fluorescent label to a receptor (typically an antibody) and measuring the amount of light emitted by the label. This technique is very sensitive but it is costly, time-consuming, requires specialized personnel and labelling affects binding affinity between analyte and receptor [44]. Most clinical detection techniques such as colorimetry or enzyme-linked immunosorbent assay (ELISA) are based on fluorescence techinques.

Recent developments on fluorescence-based techniques focus in Förster (sometimes also referred to as fluorescence) resonance energy transfer (FRET). FRET bases on the energy transfer between two light-sensitive materials (such as fluorophores). This process occurs when the donor material, in its excited state, is close enough to the acceptor material so as to transfer energy through a non-radiative process resulting in light emission of the acceptor material [46]. The separation between the two materials is crucial in FRET, as the energy transfer efficiency rapidly decays with increasing distance as given by eq. 2.10:

$$E = \frac{{R_0}^6}{{R_0}^6 + R^6} \tag{2.10}$$

Where E is the FRET efficiency, R is the distance between the donor and the acceptor and R_0 is the critical energy transfer distance (Förster radius) for FRET which is defined as the distance for 50% efficiency.

This distance dependence of FRET has been used for the development of biosensors by either FRET quenching (off state) [47] or FRET emission (on state) [48].

b) Microrefractometry

This group of techniques measure changes in the refractive index at the interface between two adjacent materials by measuring the properties of the generated evanescent waves. Evanescent waves appear at the interface of the two mediums as a result of the fact that the electric and magnetic fields cannot be discontinuous at the boundary. This generates a near-field wave whose intensity decays exponentially with increasing distance from the interface. Due to the exponential decay of the evanescent wave, there is inhomogeneous signal penetration into the analyte solution. This means that the changes registered by the device are limited to surface events up to few nanometers away from the sensor's surface [44]. Due to the characteristics of evanescent wave excitation, experimental setups for microrefractometric optical biosensors tend to be bulky, as they typically require the use of prisms for coupling light into the device. Another disadvantage of microrefrctometric biosensors is the fact that they are very sensitive to temperature changes, leading to the requirement of a very good temperature control during the biosensing experiment or the use of a reference sensor to correct for environmental fluctuations.

The first developed and most common example of evanescent wave biosensor is SPR [8] Recent reports are focusing towards localized SPR (LSPR) by using metal nanoparticles to be able to excite surface plasmons without the need of bulky optical setups [45, 49]. However, numerous other microrefractometric techniques have been developed over the past few years such as grating couplers [50], resonant mirrors [51], Mach-Zender Interferometers [52], Young interferometer [53], or microstructured optical fiber (MOF) Bragg gratings [54].

c) Microreflectometry

This method is also known as reflectomectric interference spectroscopy (RIfS). In its origin, microreflectometry concentrated on measuring tiny changes in the physical thickness of the interaction layer by measuring the position of the oscillations arising in a thin film due to constructive and destructive interference upon white light illumination [10]. This approach is independent of the thickness of the biomolecular layer as the evanescent field is not crucial for the signal.

Reflectometry-based optical biosensing, unlike microrefractometric-based optical techniques, is almost independent of temperature thanks to the fact that temperature-related volume expansion is typically compensated by a decrease in the overall refractive index [44].

Lately, RIfS research has shifted to work with porous materials such as pSi [55], pSiO2 [56], pTiO [57] and NAA [58]. The advantage of using porous materials is that due to their inherent porosity, changes in the interference spectrum can be monitored as shifts in the effective refractive index. This enabled the use of more complex optical architechtures such as double-layer interferometers [59], rugate filters [60], or microcavities [61].

Magnetic

Magnetic biosensors offer a unique approach to biosensing. Over the past few years, biofunctionalized magnetic nanoparticles have been used for analyte separation and enhancement of other biosensing techniques such as cantilever-based biosensors [39]. Nevertheless, it is possible to detect analytes using various direct magnetic measurements with high sensitivity due to the lack of significant magnetic background in biological samples. This fact enables the manipulation and detection of target analytes without significantly affecting their biological activity [62].

a) Magnetic permeability

One possible way to detect the analytes is by means of magnetic permeability measurements. This can be performed by either measuring the permeability of a coil in a balanced Maxwell-Wien bridege configuration [63] or by measuring the resonant frequency of a coil in a resonant inductor-capacitor (LC) circuit (frequency- dependent magnetometer) [64].

b) Magnetic remanence

This technique bases on the magnetization decay of superparamagnetic nanoparticles upon exposure of a pulsed magnetic field. Thanks to the fact that unbound nanoparticles relax very fast, they do not contribute to the signal and the response of the sensor is mainly related with bound magnetic nanoparticles [62].This measurement is typically performed using a superconducting quantum interference device (SQUID). This device offers the highest sensitivity and largest dynamic range of all the magnetic measurement techniques. Thanks to these

properties, it has been possible to develop SQUID-based magnetic imaging methods [65] which are faster and cheaper than magnetic resonance imaging (MRI) as an in vivo detection of cancerous tumors and whose sensitivity may overcome that of MRI in the future [66].

d) Magnetoresistance

Magnetoresistance measurements are based on the findings of William Thompson (Lord Kelvin) in 1857 in which he observed how iron subjected to a magnetic field resulted in an increase of its electrical resistance [67]. This effect is known as anisotropic magnetoresistance (AMR). The sensitivity of this technique is governed by magnetoresisitive ratio (eq. 2.11):

$$MR_{ratio} = \frac{\Delta R}{R} = \frac{R - R_{Hsat}}{R_{Hsat}} \cdot 100 \qquad (2.11)$$

Where R is the measured resistance and R_{Hsat} is the minimum resistance in a saturation field.

Current techniques for magnetoresistance measurements include:

Giant magnetorisistance (GMR): they consist on the measurement of the resistance in magnetic and nonmagnetic metal thin-film multilayers. Two main approaches have been developed using this technique:

1. ***Coupled multilayer:*** this consists in a magnetic/nonmagnetic/ magnetic stack whose thicknesses allow exchange coupling between the magnetic layers. This configuration allows changing the moments of the magnetic layers from anti-parallel to parallel resulting in a decrease of the overall resistance of the

GMR. This approach allows MR ratios between 4 and 9% upon magnetic field exposure.

2. ***Spin-valve:*** this device is multilayer stack consisting of an antiferromagnetic layer, a ferromagnetic layer, a nonmagnetic layer and a ferromagnetic layer. In this configuration, the nonmagnetic spacer layer (typically Cu) is deposited thick enough to prevent any magnetic coupling between the ferromagnetic layers and the antiferromagnetic layer forces the magnetization of the adjacent ferromagnetic layer in a particular direction resulting in an exchange bias. This design results in a very sensitive device with MR ratios between 6 and 15% upon magnetic exposure.

Lately, GMR biosensors have focused on the spin-valve configuration due to their higher MR ratios. Amon the latest reports a GMR-based cell counter capable of sorting cells depending on their magnetic moments is one of the most interesting [68].

Anisotropic magnetoresistance (AMR): AMR technology has been taken over by GMR technology as its MR ratio is typically around 2 % [62]. However, GMR miniaturization at the micron scales due to lateral fringe coupling. In order to overcome this issue an AMR biosensor based on a micrometric ring for single bead detection was developed [69]. The principle of operation is based on the fact that the magnetization of the ring without any magnetic bead around is circumferential but, when a magnetic bead is placed in the center, the magnetic field becomes radial and reduces the ring's resistance.

Despite this miniaturization advancement, the MR ratio is below 1 %. For this reason most recent works in magnetic biosensing do not use AMR technology and focus on other magnetic detection techniques.

Magnetic tunnel junction (MTJ): this technique is also known as tunneling magnetoresistance (TMR). Their configuration is similar to that of spin-valve GMR but instead of having Cu as a spacer layer, they have a thin insulator layer of just a few nanometers. Their working principle bases on a quantum mechanical phenomenon in which electrons can tunnel between two ferromagnetic materials separated by a thin insulating layer. This effect is favored when the two ferromagnets are in the magnetized in the same direction. Their MR ratio is between 20 and 70 % in sensors with amorphous Al_2O_3 as the insulating material [70] and can be further increased to above 200 % if MgO is used as the tunnel barrier due to its spin-filtering properties [71]. This makes them the most sensitive MR sensors available. Recent reports on TMR biosensors focus on the use of electromagnetic traps to concentrate the analyte in the sensor [72].

e) Hall effect

Hall effect biosensors are based on the fact that the charge carriers in a current-carrying conductor under the influence of a magnetic field are pushed to one side of the conductor. This generates a measurable electric field (i.e. Hall voltage) which is perpendicular to both the magnetic field and the applied current [62]. This effect can be used to detect biofunctionalized magnetic micro and nanoparticles and stablish the analyte concentration as a function of the induced Hall voltage, whose magnitude is given by eq.2.12:

$$V_H = \frac{IH}{t} R_H \qquad (2.12)$$

Where V_H is Hall voltage induced by the magnetic field, I is the current flowing through the device, H is the magnetic field strength, t is the thickness of the region affected by the hall effect, and R_H is the Hall coefficient.

Thanks to the miniaturization techniques available, microscale planar Hall effect (PHE) biosensors have been developed. Recent studies regarding PHE biosensing include using electric field distributions to concentrate the magnetic nanoparticles [73], determine biomolecular binding using PHE for determining the Brownian relaxation of the nanoparticles [74] and the use of aptamers as recognition elements [75].

Calorimetric

Calorimetric biosensors (also called enzyme thermistors) were developed in 1974 by Mosbach and Danielsson as heat-sensitive enzyme biosensors [5]. They are based on the measurement of temperature changes due to an enzymatic catalytic reaction with a thermistor. One of the main advantages of the enzyme thermistors is the ability of increasing the system's sensitivity by combining multiple enzymes which increase the total heat produced. An example would be the combination of glucose oxidase, which generates gluconic acid and hydrogen peroxide, and catalase that transforms hydrogen peroxide into water and oxygen [76]. In order to broaden their possible applications, thermometric enzyme-linked immunosorbent assay (TELISA) has been developed as a novel technique for detection of immunocomplexes based on enzyme thermistors [77].

2.3. AFFINITY BIOSENSING

We have already discussed in previous sections that there are two biosensing trends: catalytic (i.e. enzymes) and affinity based. Despite the fact that numerous biosensors in literature are enzyme-based, there is an increasing interest in the development of affinity-based devices. Affinity biosensors have a wider range of possible receptors (antibodies, antigens, cells, DNA, aptamers, etc) than catalytic devices which are limited by the available enzymes in the market. This makes affinity sensors applicable to fields ranging from environmental sciences to drug discovery.

2.3.1. BIOSENSING UNDER EQUILIBRIUM CONDITIONS

As explained in section 2.2.3, affinity reactions occur when an analyte A interacts with a receptor B to form the complex AB in a non-covalent and reversible manner as shown in eq. 2.4. Therefore, in an affinity reaction A and B are associate (bind) and dissociate (unbind) at the same time until either equilibrium is reached (i.e. $A_{binding} = A_{unbinding}$) or all the available sites are occupied. Thus, binding of the analyte to form the AB complex depends on the amount of available free receptors in a concentration driven reaction that follows a Langmuir isotherm model [78]:

$$A = \frac{A_{max}[A]}{K_D + [A]} \tag{2.13}$$

Where A is the amount of analyte captured under equilibrium conditions, A_{max} is the maximum amount of analyte that can be captured by the receptor, [A] is the concentration of the analyte and K_D is the affinity constant of the biochemical reaction. This equation is applicable to a biosensor's calibration curve

in which A would be the response of the biosensing device at concentration [A] and A_{max} the response under saturation conditions.

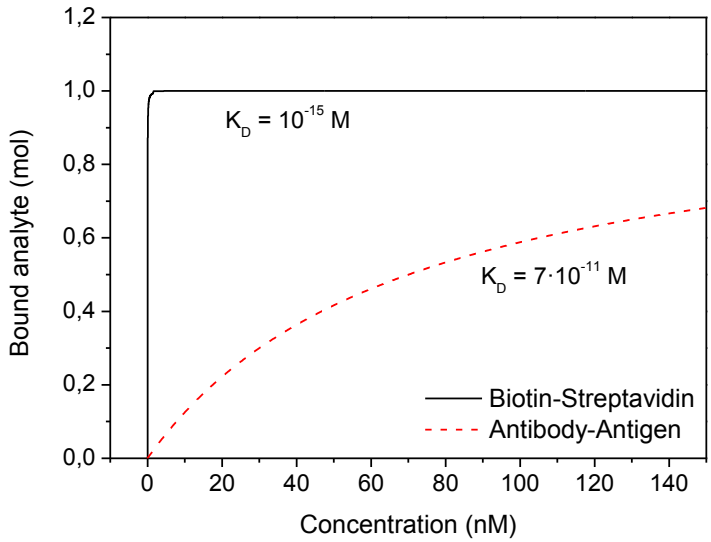

Figure 2.2. Theoretical Langmuir isotherm for biotin-streptavidin binding (black line) and antibody-antigen binding (red line) to a surface coated with enough binding sites for 1 mol of the respective analyte.

Fig. 2.2 shows two examples of the Langmuir isotherm for two well-known affinity reaction: biotin-streptavidin ($K_D \approx 10^{-15}$ M) and antibody-antigen ($K_D \approx 7 \cdot 10^{-11}$ M). For comparative reasons we assumed a surface capable of binding 1 mol of the respective analytes. These theoretical curves allow us to observe graphically the effect of the available binding sites on a biosensor's surface on its detection performance. It can be noted how, as the available binding sites are occupied, it becomes more difficult for the analyte to bind its specific receptor due to steric crowding leading to a lesser sensitive response when analyte con-

centrations are close to the saturation conditions. However, we can also see that K_D plays a key role on the biosensor's sensitivity slope as it can be observed by comparing the Langmuir isotherms of both biotin-streptavidin and antibody-antigen reactions. Finally, the latest factor implicated on the biosensor's response is the amount of available receptors on the active surface (A_{max}) which is strongly associated with surface coverage obtained and covalent binding techniques used [78].

2.3.2. REAL-TIME BIOSENSING KINETICS

Theory

Real-time detection of analytes by means of affinity biochemical interactions are governed mainly by two processes: the association process and the dissociation process.

During the association process the analyte of interest binds to the receptor present on the biosensing surface. This binding event occurs by means of non-covalent intermolecular interactions such as hydrogen bonding, electrostatic interactions, hydrophobic interactions and Van der Waals forces.

During the dissociation process, the analyte solution is completely removed from the biosensing surface. This environmental change results in the separation of the receptor-analyte complex by affecting the strength of the non-covalent intermolecular interactions. The rate at which the analyte will separate from the receptor depends on the affinity between the two analyte and the receptor.

Fig. 2.3 shows an ideal real-time measurement of an affinity biochemical reaction. Real-time monitorization consists in four distinct regions: a baseline (fig.

2.3I), an association (fig. 2.3II) curve, a stable equilibrium region (fig. 2.3III) and dissociation curve (fig. 2.3IV). In the following sections, we are going to discuss the equations related to the association and dissociation as well as the difference between theory and reality.

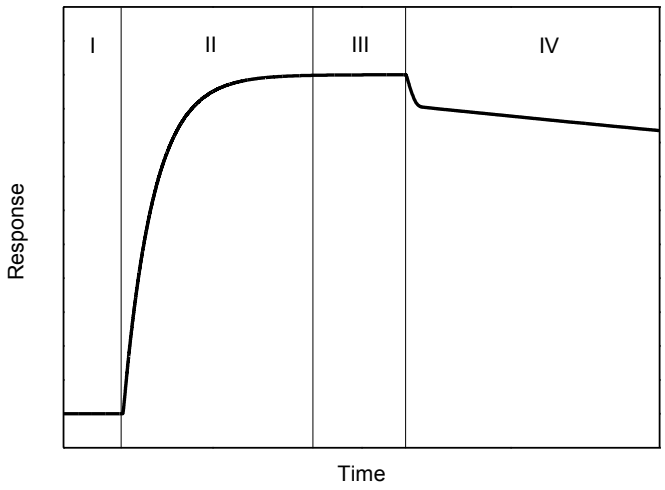

Figure 2.3. Theoretical real-time biosensing curve. I represents the baseline, II represents the binding event, III represents the equilibrium region, and IV represents the dissociation of the analyte.

Association

According to the Langmuir isotherm model explained in the previous section, the sensor response during real-time measurements in biosensing experiments should follow a negative exponential trend as shown in eq. 2.14 [79]:

$$R = \frac{R_{max}\,[A]}{K_D + [A]}\left(1 - e^{-k_{on}t}\right) \tag{2.14}$$

Where R is the sensor response at time t, R_{max} is the sensor response under saturation conditions, K_D is the dissociation constant, [A] is the analyte concentration, and k_{on} is the on rate of the sensor.

Since in an affinity reaction the equilibrium can be achieved by either occupying all the available binding sites or by equilibrating the amount of analyte binding and the amount of analyte unbinding in a concentration-dependent fashion, k_{on} will be expressed as [79]:

$$k_{on} = k_{ass}[A] - k_{diss} \tag{2.15}$$

Where k_{on} is the on rate, k_{ass} and k_{diss} are the association (binding rate) and dissociation (unbinding rate) rates of the biochemical reaction respectively, and [A] is the analyte concentration.

The association and dissociation rates are very important factors in the characterization of affinity biochemical interactions. They define the dissociation constant (eq. 2.16) of the reaction and thus define the affinity between two biomolecules.

$$K_D = \frac{k_{diss}}{k_{ass}} \tag{2.16}$$

Where K_D is the dissociation constant, and k_{ass} and k_{diss} are the association and dissociation rates of the biochemical reaction.

Dissociation

In affinity-based sensing, once the analyte-containing solution is removed from the sensor's surface and replaced by clean buffer solutions, bound analytes will start to dissociate from their respective receptors following an exponential trend (eq. 2.17) [79].

$$R = (R_0 - R_\infty)e^{-k_{off}t} + R_\infty \quad (2.17)$$

Where R_0 is the initial response of the biosensor, R_∞ is the response of the biosensor at the final analyte concentration, k_{off} is the off rate of the sensor and t is time.

Due to the fact that during dissociation it is assumed that no rebinding occurs, $k_{off} = k_{diss}$.

Experimental fittings

Despite the fact that the theory of biomolecular binding explains accurately the kinetics of biosensing, these equations fail to fit real experimental data during association experiments. Actually, the best fittings are achieved by superimposing two negative exponentials instead of the one predicted by the theoretical model as explained in eq. 2.18. This second exponential is related with the ability to transport the analyte onto the sensing surface (i.e. flow rate of the analyte solution) [79].

$$R = \frac{R_{max}\,[A]}{K_D + [A]}\left(1 - e^{-k_{on_1}t}\right) + B\left(1 - e^{-k_{on_2}t}\right) \quad (2.18)$$

Where R is the sensor response at time t, R_{max} is the sensor response under saturation conditions, K_D is the dissociation constant, [A] is the analyte concentration, B is a constant that depends on the analyte's mass transport, and k_{on1} and k_{on2} are the on rates of the sensor being the first one correlated to the affinity of the biomolecules and the second with the mass transport.

Biosensing using initial rate analysis (IRA)

Biosensing under equilibrium conditions may take several minutes or even hours depending on the biosensor architecture, especially when the analyte concentration is extremely small. One of the advantages of real-time sensing is the possibility of determining the analyte concentration by analyzing their kinetic behavior [79]. We can do so by deriving eq. 2.14:

$$\frac{\partial R}{\partial t} = \frac{R_{max}[A]}{K_D+[A]} k_{on}(1 - e^{-k_{on}t}) \tag{2.19}$$

For small t (i.e. the initial linear region of the association curve), eq. 2.19 turns into:

$$\frac{\partial R}{\partial t} = \frac{R_{max}[A]}{K_D+[A]} k_{on} \tag{2.20}$$

Applying eq. 2.15 and 2.16 to eq. 2.20 leads to the following expression:

$$\frac{\partial R}{\partial t} = R_{max}[A]k_{ass} \tag{2.21}$$

Eq. 2.21 shows how the initial region of the biosensing curve is governed by the saturation signal of the sensor and the association rate of the biochemical reaction in a linear fashion. Therefore, it is possible to determine the concentra-

tion of the analyte by observing the initial linear region of the association curve, which is particularly interesting for enhancing the speed of the sensor response.

2.4. APPLICATIONS OF BIOSENSORS

The emerging field of biosensors is still growing and despite what many people may think, its application is not limited to clinical diagnosis. In fact, biosensors are applicable to a number of fields such as drug discovery [80], cellular studies [81], environmental monitorization [82], food processing [13], chemical and biochemical sensing [83], forensics [84], clinical diagnosis [85] and point-of-care use [86].

Chapter II

CHAPTER III

NANOPOROUS ANODIC ALUMINA FUNDAMENTALS

3.1. HISTORY OF NANOPOROUS ANODIC ALUMINA

The field of metal anodization started back in the 1920s and was used for commercial purposes as a method for generating a protective and/or decorative layer on top of the metal. In 1923, Bengough and Stuart patented the first anodization process for aluminum consisting in a chromic acid-based anodization [87]. Later, in 1927, Gower and O'Brien patented the first sulfuric acid-based anodization which is nowadays the most common anodizing electrolyte used in industry [88]. In 1936, Carboni invented a method for coloring the resulting NAA film for aesthetic purposes consisting in a combination of sulfuric acid anodization and an alternating current process in a metal salt solution [89].

The invention of the electron microscope in 1938 and its further commercialization in 1939 allowed further development of NAA technology. In 1953, Keller et al. characterized, for the first time, the structure of NAA. In this work, Keller and coworkers described the characteristic hexagonally close-packed pores and the bottom barrier layer of NAA. Also, they demonstrated the relationship between the applied potential and interpore distance [90]. The first detailed description of the state of the art of NAA was published in 1969 by Diggle et al. [91]. In this review, structural features, anion incorporation, water content and formation mechanisms of both barrier and porous-type alumina were thoroughly discussed. Following the work of Keller et al., Thompson and Woods' studies of NAA using electron microscopy techniques resulted in a deeper comprehension of the structural properties of NAA as well as its growth mechanisms [92, 93, 94, 95, 96, 97, 98, 99].

A major breakthrough was achieved in 1995 by Masuda and Fukuda with the discovery of nanopore self-ordering by means of a two-step anodization procedure [100]. This technique was later optimized by Nielsch et al. in 2002 for the

three most common electrolytes (i.e. sulfuric, oxalic and phosphoric acids). In this work they observed how self-ordering was achieved when the porosity of the NAA layer was around 10 % [101].

Lately, NAA technology has been focused on the development of 3D nanopore structures by in-depth modulation of pore diameter. To date, several voltage-dependent techniques have been developed such as pulse [102, 103, 104] and cyclic [105, 106, 107] anodization and also recently, current control techniques have emerged [108, 109].

3.2. BASICS OF NANOPOROUS ANODIC ALUMINA FABRICATION

3.2.1. ELECTROCHEMISTRY OF NANOPOROUS ANODIC ALUMINA FORMATION

Thermodynamics

When an aluminum film is either exposed to air or water, it spontaneously reacts forming a thin layer of aluminum oxide. This phenomenon has been ascribed to the large negative Gibb's free energy change [110].

$$2Al(s) + \frac{3}{2}O_2(g) \rightarrow Al_2O_3(s); \quad \Delta G^\circ = -1582\ kJmol^{-1} \tag{3.1}$$

$$2Al(s) + 3H_2O\ (l) \rightarrow Al_2O_3(s) + H_2(g); \quad \Delta G^\circ = -871\ kJmol^{-1} \tag{3.2}$$

However, when aluminum films are electrochemically anodized, the process can be described by the following redox equations [111]:

1. At the anode (i.e. the aluminum film) grows an oxide film (aluminum-aluminum oxide interface):

$$2Al(s) + 3H_2O(l) = Al_2O_3(s) + 6H^+ + 6e^- \quad (3.3)$$

2. At the cathode (cathode-electrolyte interface) hydrogen evolves:

$$6H^+ + 6e^- = 3H_2(g) \quad (3.4.)$$

Kinetics

The current density measured during the anodization of the aluminum foil can be expressed as follows:

$$j = j_a + j_c + j_e \quad (3.5)$$

Where j_a, j_c and j_e are the contributing current densities of the anions, cations and electrons respectively. Given the extremely high electronic resistivity of alumina ($\rho_{alumina} = 10^{14}\ \Omega\cdot cm$), j_e becomes negligible leaving the current density expression as:

$$j = j_a + j_c \quad (3.6)$$

Therefore, the anodization of aluminum strongly depends on the transport of Al^{3+} and O^{2-} ions.

3.2.2. PORE FORMATION THEORIES

In order to understand the process of pore formation, it is necessary to take a look at the current density-time (*j*-*t*) transient. Figure 4.1 shows the first 500 s of the fabrication of a NAA layer using conventional potentiostatic anodization in

oxalic acid (0.3 M, 40V and 5°C). Four different stages can be appreciated during the initial stages of aluminum anodization. In stage I, current density drops rapidly due to the formation of a solid alumina layer. After this point, two main theories have emerged in order to explain the mechanism of pore formation: the electric field instability model and the convection model.

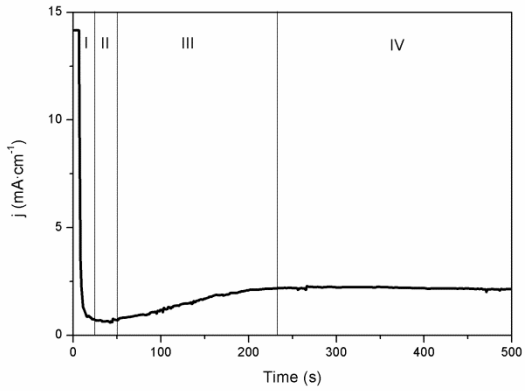

Figure 3.1. Current density-time transient of the first 500 s during the anodization of a high-purity aluminum foil under potentiostatic conditions in 0.3 M oxalic acid at 40 V and 5°C. Regions I, II, III and IV represent each of the stages of NAA formation.

The electric field instability model

This model is the most accepted among the scientific community [112, 113, 113, 115, 116, 117, 118, 118, 120]. This theory claims that the mechanism of pore formation in NAA is analogous to that of porous silicon. Essentially, it bases on the fact that after the formation of the solid alumina layer in stage I, elec-

tric field instabilities start to appear leading to the formation of pores. Assuming this model, pore growth would continue as follows:

In stage II, current density reaches its minimum value. At this point, instabilities in the electric field results in localized partial dissolution of the alumina layer formed in stage I. These spots where partial dissolution started to occur in stage II serve as nucleation centers for pore formation in stage III, where pore generation increases the current density measured. Finally, in stage IV, current density reaches its maximum value and starts to slowly and asymptotically decrease to a constant value, where pores grow in a steady-state manner.

The convection model

The convection model is based on the similarity between the honeycomb structure of NAA and the structure of Rayleigh-Bénard convection cells (R-BCC) [121, 122, 123]. R-BCC are dissipative structures appearing under critical temperature gradients in thin films of viscous fluids. The resulting "cells" typically present a hexagonal ordering. This ordering may seem to break the second law of thermodynamics, but in fact, it is the reflection of the system's tendency to arrange in the minimum energy possible.

Figure 3.2. A shows the typical R-BCC achieved in a thin film of viscous liquid in a petri dish, and figure 4.2. B shows a typical top SEM view of a NAA sample. Both systems show a similar ordering behavior. Defects in the ordering in both images arise from defects in the substrate (i.e. the petri dish in figure 3.2. A and the aluminum bulk in figure 4.2. B). For this reason, Pashchanka and Schneider modeled pore formation in NAA as a R-BCC [121].

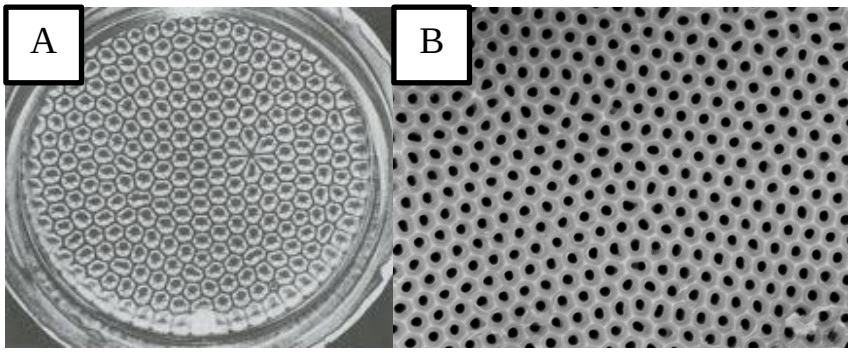

Figure 3.2. Comparison between A) Rayleigh-Bénard convetion cells in a viscous liquid and B) honeycomb pattern from NAA manufactured in conventional oxalic acid anodization.

According to this model, the j-t transient depicted in figure 3.1. could be explained as follows:

In step I, along with the formation of thin layer of solid anodic alumina, negative charges are attracted to the anode creating a charge gradient. In step II, the charge gradient reaches its critical value after which current starts to rise again. This current rise present in step III is the result of the diffusion of anions in the opposite direction, starting the convective process. Finally, in step IV, the competition between the attraction and diffusion of anions leads to the formation of R-BCC and a steady-state growth of the nanopores is achieved.

3.2.3. ORDERING OF PORES

In NAA, pore ordering can be achieved by two main techniques: nano imprint lithography (NIL), for perfectly ordered NAA; and two step anodization, for self-ordered NAA.

Perfect ordering using Nano Imprint Lithography (NIL)

NIL bases on the fact that pores in NAA nucleate at defect sites in the aluminum substrate [124, 125, 126]. Taking advantage of this feature, NIL creates an ordered array of surface defects in order to promote pore nucleation at specific locations thus resulting in a perfectly ordered array of nanopores.

Figure 3.3. shows the steps of NIL for perfectly ordered NAA (PONAA). The first step consists in pressing a Si_3N_4, SiC or Ni master stamp consisting in an array of pyramids onto a polished aluminum substrate. This step results in an ordered array of inverted pyramids (nanoindentations) which will serve as nucleating sites for the NAA pores. Subsequently, the aluminum substrate is anodized under the appropriate conditions so as to ensure perfect ordering.

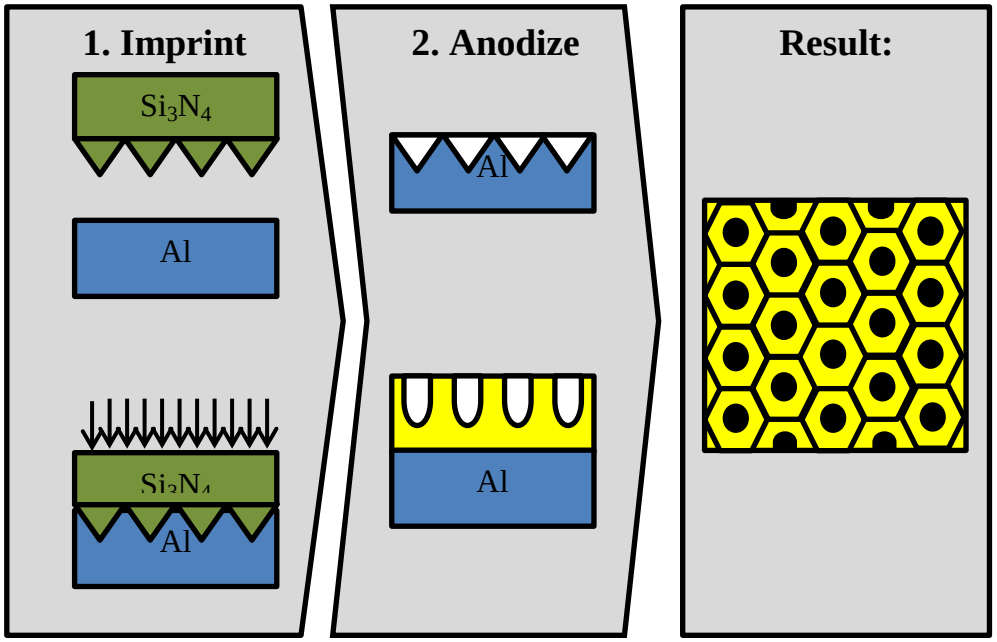

Figure 3.3. Schematic procedure to obtain PONAA using NIL.

The advantages of this procedure are the reduced time required to fabricate PONAA and the possibility of fabricating arrays of nanopores with lattices other than hexagonal (i.e. square lattice). However, this procedure is limited by the actual microfabrication techniques available and an expensive master stamp. In order to overcome these disadvantages, a new technique combining laser interference lithography (LIL) and hard anodization has been developed recently [127]. This technique allows to fabricate PONAA with aspect ratios higher than 500 in a cost-effective manner.

Self-ordering of pores using two-step anodization

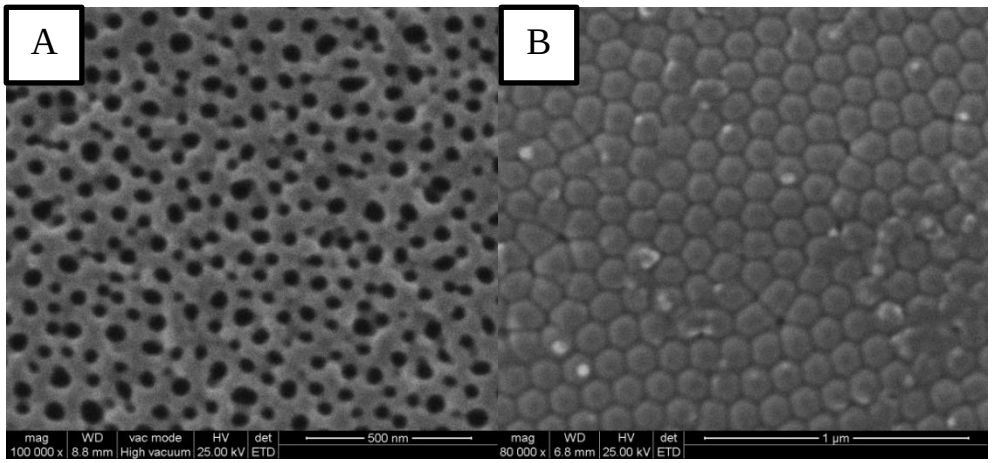

Figure 3.4. SEM micrographs of A) top of a disordered NAA sample and B) bottom of the sample after selective dissolution of the aluminum substrate showing the closed pore tips**.**

The method for obtaining self-ordered NAA (SONAA) by means of two-step anodization was discovered by Masuda and Fukuda back in 1995 [100]. In their experiments, they observed that after a long anodization, the bottom of the pores was ordered in domains of pores with a hexagonal lattice.

Figure 3.4. shows SEM micrographs from the top (figure 3.4.A) and bottom (figure 3.4.B) of a first step after selective dissolution of the aluminum bulk. The hexagonal arrangement of the pores' bottom is preserved on the aluminum substrate after selective dissolution of alumina. This texture left on the aluminum serves as nucleating centers for pore formation in the next anodization step.

The experimental procedure for the fabrication of SONAA via two-step anodization is depicted in figure 3.5.

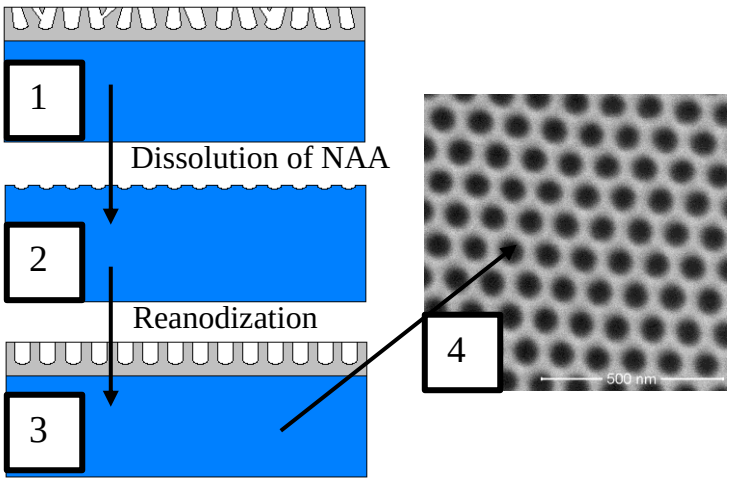

Figure 3.5. Schematic representation of the fabrication procedure of SONAA using two step anodization. 1) Disordered porous layer resulting from the 1st anodization step, 2) nanostructured Al foil obtained after selective dissolution of the disordered NAA layer, 3) self-ordered NAA layer obtained in the 2nd anodization, and 4) SEM micrograph of the top view of a SONAA.

The origin of the self-ordering: the mechanical stress model

The self-ordering phenomenon in NAA has been attributed to a mechanical stress at the metal/oxide interface [128, 129]. During the anodization, since the density of Al_2O_3 is lower than metallic aluminum by a factor of 2, the volume of the oxide formed expands about twice the original volume of the aluminum substrate. This volume expansion (ξ) creates a compressive stress at the metal/oxide interface. This compressive stress generates repulsive forces that lead to pore ordering. However, if ξ is maximal ($\xi_{max} \approx 2$), the anodization process will result in a barrier-like alumina layer. If the stress is very small ($\xi < 1.2$), the repulsive forces generated by the compressive stress are insufficient to promote the self-ordering phenomenon and a disordered pore structure is achieved. Therefore, in order to achieve pore self-ordering, a moderate volume expansion of $\xi \approx 1.2$ is required.

3.2.4. ANODIZATION PARAMETERS

Potential

One of the most limiting factors during the anodization of aluminum is the applied potential (U). This parameter is linearly proportional to the interpore distance (D_{int}) as shown in equation 3.7.

$$D_{int} = kU \tag{3.7}$$

Where k is the proportionality constant. This linear correlation has been experimentally elucidated as: $k \approx 2.5\ nmV^{-1}$ for mild anodization (MA) regime [92, 101], and $k \approx 2.0\ nmV^{-1}$ for hard anodization (HA) regime [102].

Barrier layer thickness (t_{BLA}) has also been correlated with D_{int}, and has been estimated to be half its value ($t_{BLA} = 0.5\ D_{int}$) [102].

Electrolyte

Electrolyte composition is crucial for the fabrication of high-quality NAA films [101]. Even though several exotic acids such as tartaric and formic acid have been tried lately, NAA fabrication is traditionally performed in either sulfuric, oxalic or phosphoric acid. Sulfuric acid is used for anodization at low potentials (typically 20 V for MA and 40 V for HA), oxalic acid is used for intermediate potentials (i.e. 40 V for MA and 120 V for HA) and phosphoric acid is used for high potentials (i.e. 160-195 V). This division is related with the properties of each acid and mainly, on their pH and conductivity. pH directly affects the pore size. The lower the pH, the lower the potential required for pore formation. Thus, a lower pH allows the fabrication of smaller pores. The effect of electrolyte conductivity is also important. Highly conductive electrolytes like sulfuric acid are limited to low potentials due to the high current developed and the resulting heat generated by Joule's effect.

Temperature

Temperature has a direct effect on the anodization of aluminum foils. Higher temperatures result in wider pores due to the stronger dissolution of the formed

alumina in acidic electrolytes. This is one of the reasons for which temperature has to be kept below room temperature during the electrochemical etching. The other reason is to avoid heat generation at the pore tips due to Joule's effect. Localized heat results in inhomogeneous oxide growth that leads to oxide breakdown (also known as "burning" of the NAA sample). This "burning" effect is more common at high potentials, where localized heat is prone to produce inhomogeneous electric fields. On the other hand, lower temperatures result in slower growth rates. Also, if the temperature is below 0 °C and water-based electrolytes are used, freezing of the electrolyte might occur. Typical operating temperatures are 5 °C for sulfuric and oxalic acids under MA conditions, and 0 °C for phosphoric acid under MA conditions and sulfuric and oxalic acids under HA conditions.

Viscosity

Recently, it has been discovered that the viscosity of the electrolyte has a direct effect on the resulting nanostructure. This effect is related with the reduction of the electrophoretic velocity (υ) of the ions as expressed in equation 3.8 [130].

$$\upsilon = \frac{\epsilon \zeta E}{\pi \eta} \tag{3.8}$$

Where ϵ, ζ, E, and η are the dielectric coefficient, zeta potential, electric field, and the viscosity coefficient, respectively.

This reduction of υ reduces the current density developed during the anodization. This reduces the growth rate of NAA but also reduces Joule's effect and prevents localized heating at pore tips. For this reason, increasing the viscosity

of the electrolyte helps to avoid oxide breakdown, especially at high electric fields.

Ethyleneglycol (EG), polyethyleneglycol (PEG) and glycerol are the common additives used for adjusting the electrolyte viscosity. These chemicals, apart from reducing υ, they also prevent chemical dissolution of the porous structure by the electrolyte, thus reducing the porosity of the resulting NAA film [131].

Apart from stabilization of anodization at high potentials and reduction of porosity, it has been proved to have a direct effect on D_{int}. An experiment in which 0.3M oxalica acid electrolytes with glycerol concentrations between 0 (water-based electrolye) and 100 % (glycerol-based electrolyte) revealed that higher viscosities result in larger D_{int} [132]. This dependence was linear to the logarithm of the resulting viscosity. Moreover, they found that for a glycerol-based electrolyte no pores were generated and a barrier-type alumina layer was produced.

Aluminum substrate

In order to obtain high-quality NAA films, high purity aluminum foils are required (≥ 99.99 %). The presence of impurities in the aluminum substrate leads to defects in the structure that may be due to volume expansion differences or electric field disturbances. Recently, it has been reported how aluminum foils with a lower purity (99.8 %) present differences with respect to the highest purity foils (99.999 %) [133]. In this work, it was observed how lower purity leads to slightly smaller and branched pores and how this effect increased with the electric field.

3.3. FABRICATION PROCEDURE OF NANOPOROUS ANODIC ALUMINA

3.3.1. EXPERIMENTAL SETUP

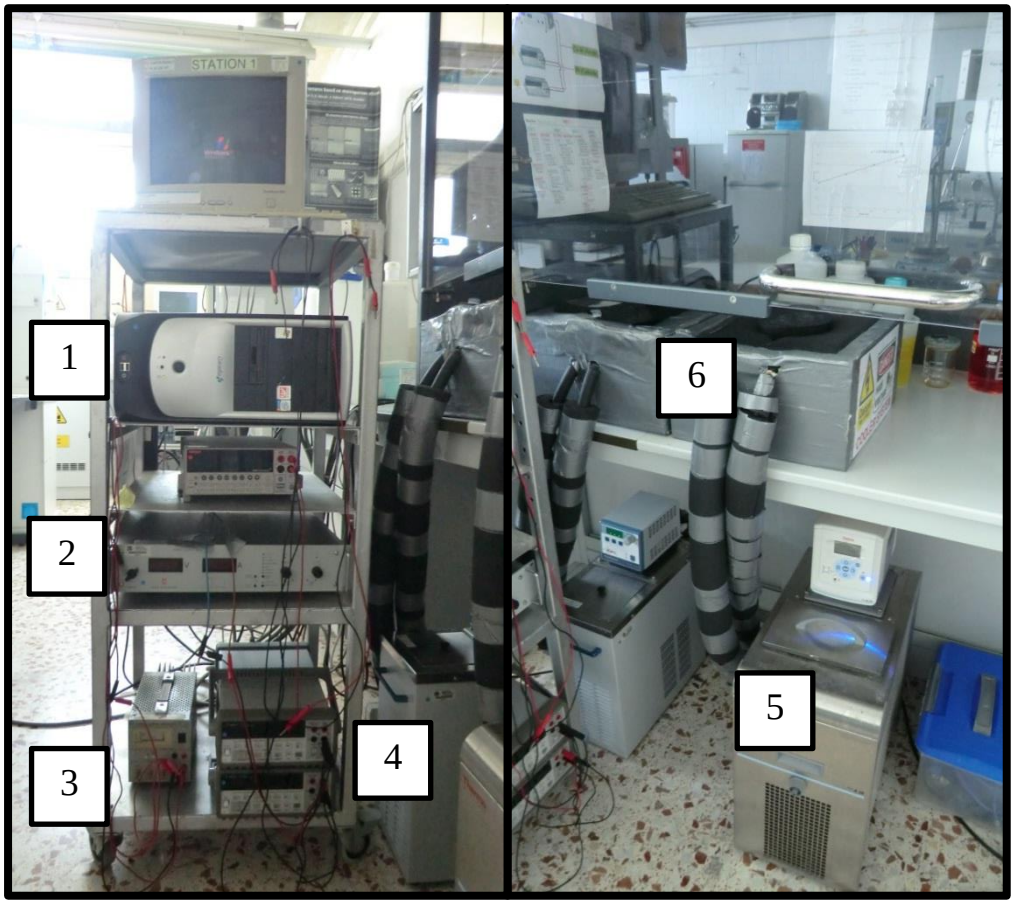

Figure 3.6. Experimental equipment required for the fabrication of NAA films. 1: personal computer; 2: power supplies for anodization; 3: power supply for the stirrer; 4: multimeters; 5: cooling systems for anodizations; and 6: cooling plates for refrigeration of the electrochemical cells.

The experimental setup available in our research facilities for the fabrication of NAA films is presented in figure 3.6. The setup consists in a power supply controlled with a personal computer, a power supply for the electrolyte stirring and a cooling system to maintain the temperature of the anodization cell below room temperature. In order to ensure more productivity and prevent delays in the results due to maintenance or breakdowns, the setup is duplicated.

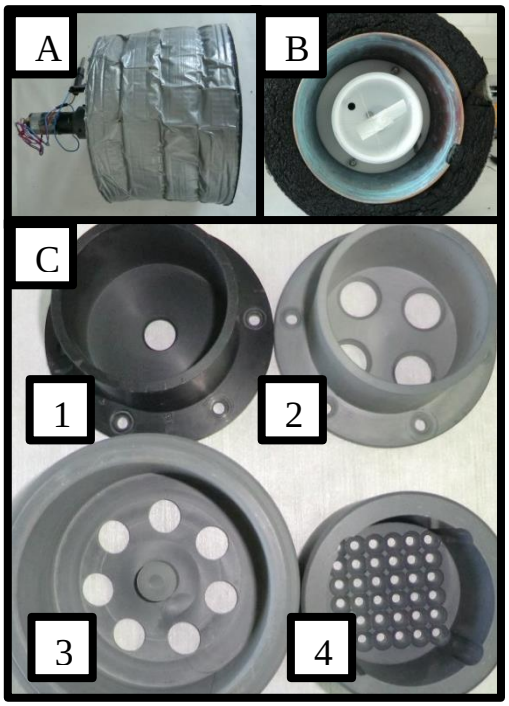

Figure 3.7. Electrochemical anodization cell used for the fabrication of NAA films. A) side view of the cathode; B) bottom view of the cathode; C)cells for 1: single sample anodization, 2: quadruple sample anodization, 3: 7 sample anodization and 4: 36 array anodization.

Our lab has been dedicated to improve the electrochemical anodization cell continuously. Figure 3.7 shows the actual anodization cell. Our anode consists in a copper plate and our cathode (figure 3.7A and 3.7B) consists in a platinum

mesh placed in a Teflon holder. The cathode is coupled with a stirrer to remove the hydrogen bubbles generated during the anodization and a metal cylinder covered by a thermal insulator to maintain the electrolyte below room temperature. Figure 3.7C shows the four kinds of anodization cells available in our lab. Our equipment allows us to perform from single anodization to 36 arrays of NAA films

3.3.2. SOFTWARE

The control over the anodization of aluminum sheets was performed with custom-made LabView-based programs. Figure 3.8 shows a screen capture of a program designed for the fabrication of NAA monolayers. Accurate control of the characteristics is achieved by adjusting the voltage and controlling either the anodization time or the total charge passing through the anodization cell.

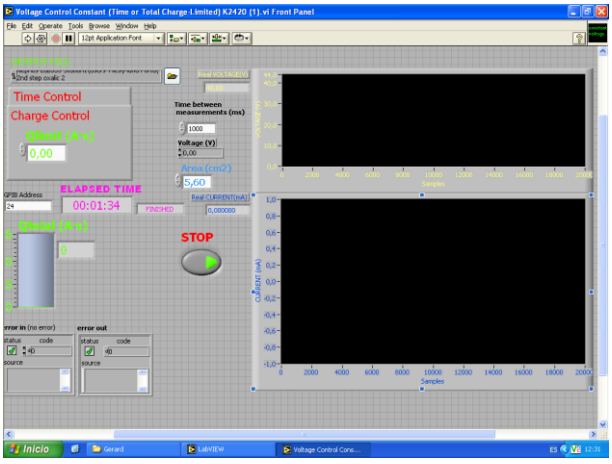

Figure 3.8. LabView-based software used for the fabrication of NAA films.

3.3.3. PRETREATMENT

As purchased aluminum foils do not possess the requirements to obtain highly ordered NAA thin films. This is so due to their fabrication procedure. During manufacturing, Al foils develop high roughness and their grain size is typically too small to obtain large domains. Therefore, Al substrates must be pretreated to ensure high-quality NAA films.

Annealing

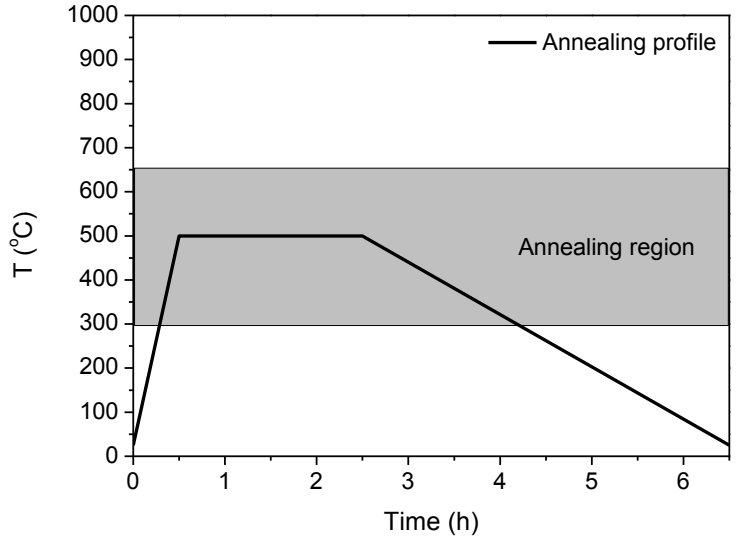

Figure 3.9. Typical annealing temperature profile. Blue (dotted) and red (dashed) lines show the recrystallization and melting temperatures for Al.

The process of annealing is a well-known thermal treatment used to eliminate material stress. This temperature profile is represented in figure 3.9. It consists in a fast increment of the temperature of the metal to an intermediate value be-

tween its recrystallization and its melting temperatures followed by a slow decrease. Typically, this process uses temperatures close to the recrystallization value for shorter times as big grains are not desirable for mechanical purposes. However, for the fabrication of highly ordered NAA films, we require huge grains, as this will lead to larger self-ordered domains [134]. Figure 3.10 shows a photograph of a high-purity Al foil after annealing showing a grain size of 1-2 mm^2.

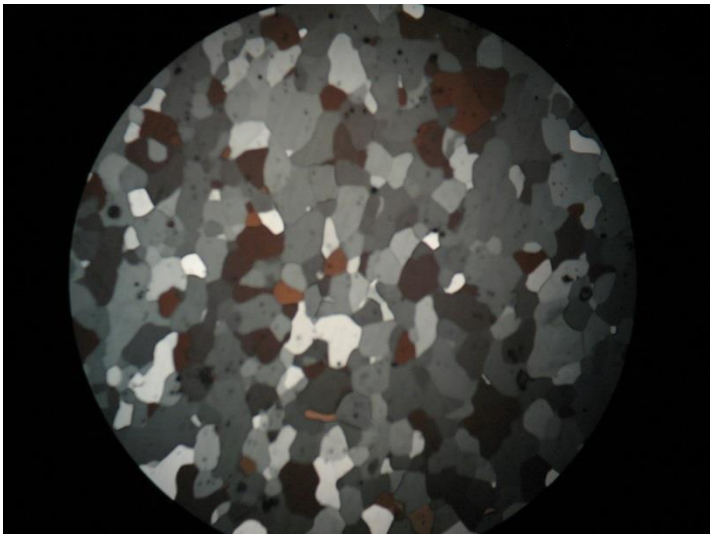

Figure 3.10. Photograph of a high-purity aluminum foil after annealing. The foil was chemically etched in order to reveal the grain structure. The resulting grains had an area of 1-2 mm^2.

Polishing

The growth of NAA is perpendicular to the substrate. For this reason, flat surfaces with a very low roughness are required to develop self-ordered films. In our group, three polishing techniques have been tried: mechanical, chemical and electrochemical.

Mechanical polishing

Mechanical polishing is probably one of the best options to obtain large flat surfaces with a low level of defects. This technique is desirable when flatness is crucial (i.e. template synthesis). It can be performed either manually or automatically. However, it is slow. It requires decreasing the grain size of the abrasive material slowly to achieve good results. Furthermore, it is limited to the grain sizes of both sandpaper and colloidal solutions. Therefore, based on the available colloidal suspensions in the market, the minimum roughness that can be achieved is roughly 100 nm.

Chemical polishing

Chemical polishing of Al substrates has been proposed as an alternative to electrochemical polishing in an attempt to overcome its low throughput and requirement of complex equipment [135]. Moreover, it avoids the hazards related with perchloric acid. This process consists in immersing the Al substrate in a mixture of 15 parts of nitric acid 68 % wt and 85 parts of phosphoric acid 85 % wt. for 5 minutes followed by neutralization of the sample in 1 M sodium hydroxide for 20 min. This process results in a roughness comparable to that of electrochemical polishing without the need of power supplies or the dangerous perchloric acid.

Electrochemical polishing

Electrochemical polishing (also known as electropolishing) is the most widespread technique for polishing Al foils. It is a fast technique that results in a mir-

ror-like finish. Several electrolytes are available for electropolishing, but the 1:4 v:v mixture of perchloric acid in ethanol is the most popular. However, this technique has some disadvantages. Perchloric acid is a strong oxidant and must be handled with extreme caution. The preparation of the electropolishing mixture has to be done below 0 °C as there is risk of explosion due to the heat generated during the mixing. Also, alternated stirring is required in order to obtain high-quality surfaces. For most applications, electropolishing is appropriate, but should be avoided if extreme flatness is crucial, as the stirring affects the homogeneity of the Al dissolution leaving a macroscale shape that affects the flatness.

3.3.4. ANODIZATION

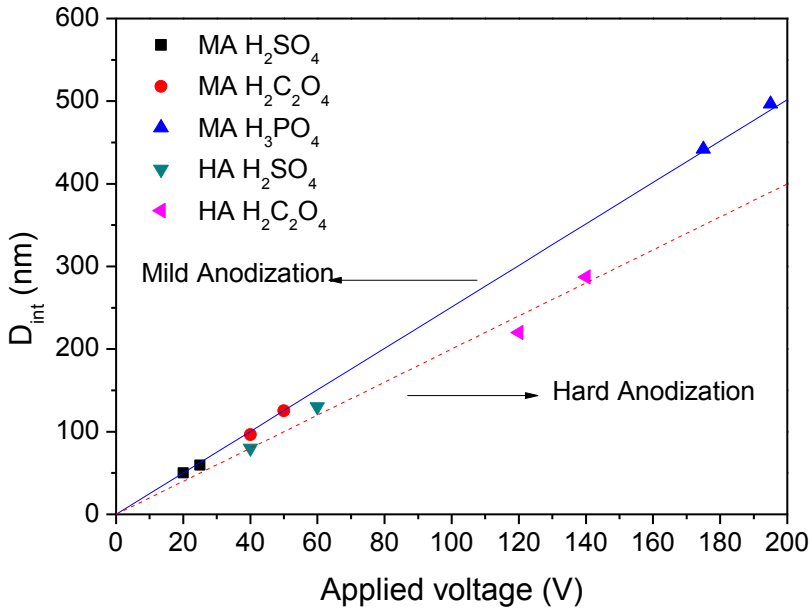

Figure 3.11. Experimental correlation of D_{int} and applied voltage for sulfuric, oxalic and phosphoric acids under MA conditions; and sulfuric and oxalic acid

under HA conditions. Blue and red lines are the linear fittings for MA and HA regimes respectively.

At our labs, two kinds of Al anodization procedures were made: mild anodization (MA) and hard anodization (HA). Figure 3.11 shows typical anodization regimes for sulfuric, oxalic and phosphoric acids.

Mild anodization

MA is based on anodization of Al foils under potentiostatic conditions and small potentials. It is characterized by the slow linear growth of the NAA film. Multiple domains of self-ordered pore arrays can be obtained under MA conditions by the two-step anodization procedure [100]. Its j-t transient is homologous to the one presented in figure 3.1. The self-ordering of this structure is governed by the 10 % porosity rule [101]. All our biosensing experiments were performed using NAA fabricated under MA conditions.

Hard anodization

HA appeared as an alternative to MA to produce NAA films fast and opened new self-ordering regimes for oxalic and sulfuric acids (see figure 3.11). Contrarily to MA, the growth of the NAA films is not linear and the resulting films display porosities around 3.3 % [102]. It must be noted that the fracture is also different, in NAA fabricated under MA conditions films break through the pores while NAA fabricated under HA conditions breaj at cell boundaries. Figure 3.12 shows the j-t transient profile of a NAA sample fabricated under HA conditions.

Due to the high electric field, HA must start with the generation of a protective layer of disordered NAA by starting the anodization under MA conditions (region I). This protective film minimizes oxide breakdown at high electric fields and enables uniform film growth. Once this protective layer is created, voltage is slowly increased at a rate of $0.5V \cdot s^{-1}$ (region II). This region is known as transient anodization (TA) and is performed to ensure homogeneous nucleation of pores for high-field anodization. During stage II, a steady increase of the generated current can be observed. Finally, the HA voltage is achieved and maintained throughout the rest of the anodization (region III). In this stage, current density decreases exponentially due to hindered diffusion of the ionic species (O^{2-}, OH^{-} and Al^{3+}).

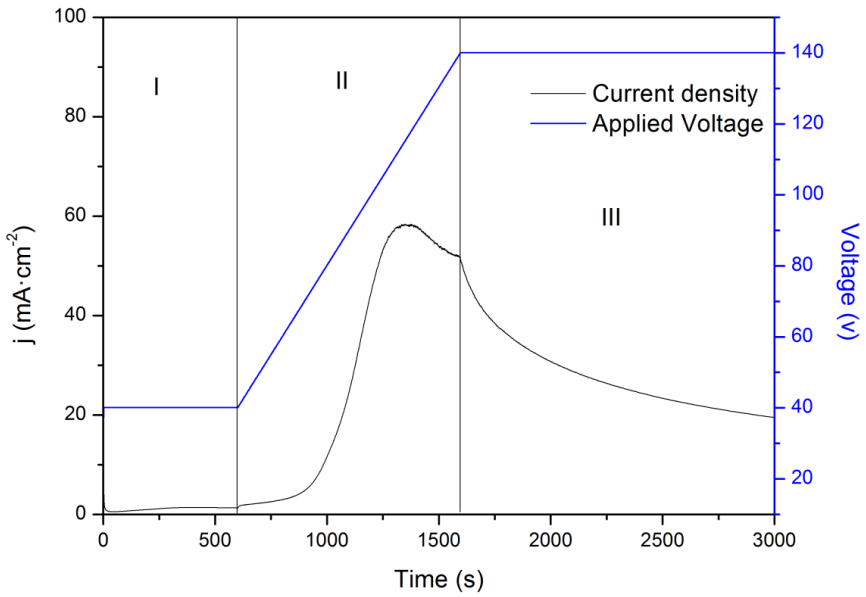

Figure 3.12. j-t transient of a NAA sample fabricated in 0.3 M oxalic acid at 1 °C under HA conditions. I: MA voltage for the generation of a protective NAA layer; II: gradual increase of the applied voltage to reach the HA value; and III: anodization under HA voltage.

The resulting structure of the NAA manufactured under HA conditions consists in a three-layer structure of:

a) disordered porous layer with a smaller interpore distance (protective layer generated during the MA in stage I)

b) a transition layer in with a high degree of pore merging (layer generated during the TA in stage II)

c) a self-ordered porous layer with a small porosity (3.3-3.4 %) and a larger interpore distance (layer generated during the HA in stage III).

The high electric field applied promotes fast self-ordering due to the strong repulsive forces generated between pores. The self-ordering in HA is strongly dependent on the electric field applied and higher voltages lead to more ordered pores [102, 136].

3.4. CHARACTERIZATION OF NANOPOROUS ANODIC ALUMINA

3.4.1. STRUCTURAL CHARACTERIZATION

Qualitative characteristics of NAA

As we explained in previous sections, NAA manufactured by the two-step anodization procedure results in self-ordered arrays of pores arranged in domains of different orientations. Figure 3.13A shows a high-quality SEM micrograph of an array of pores within the same domain. These pores are distributed in a honeycomb fashion and present two distinct oxide layers. The regions corresponding to the pores, the outer oxide layer and the inner oxide layer are delimited by blue, green and red lines respectively in figure 3.13B. This duplex

oxide structure is a result of the anodization process. The inner layer consists of "pure alumina" while the outer layer is anion-contaminated. Under optimum self-ordering regimes, the ratio between the thickness of the "pure alumina" layer on the pore wall (τ_{in}) and the thickness of the outer oxide layer of the pore wall (τ_{out}) is constant regardless of the applied voltage or electrolyte used and equal to $\tau_{in} / \tau_{out} = 0.2 \pm 0.02$ [101]. The high degree of ordering of the sample can be perceived in the 2D fast Fourier transform (FFT) of the SEM (figure 3.13C). The low degree of evenly scattered FFT maximums in the power spectrum accounts for the high degree of ordering of the structure. Figure 3.13D shows an SEM cross-section of the bottom region of the NAA sample. Straight uniform and parallel nanochannels can be appreciated. These nanochannels are truncated at the end by a hemispherical cap of dense non-porous alumina layer.

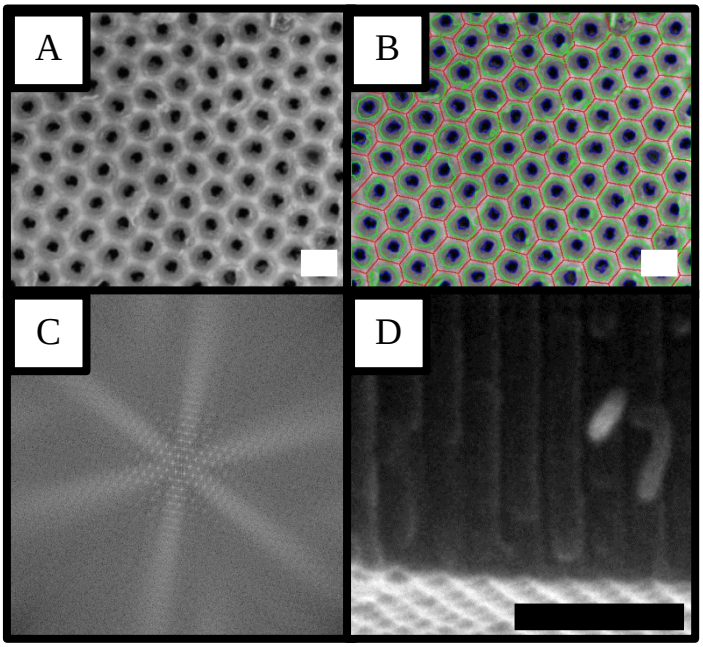

Figure 3.13. Structural characterization of NAA. A) SEM top-view of an as-produced NAA fabricated in 0.3M oxalic acid under MA conditions; B)image processing of A) depicting the pore diameter (blue lines), anion incorporated layer (green lines) and cell size (red lines); C) shows the 2D FFT of A) demon-

strating the high degree of self-ordering of the structure; and D) shows the bottom part of the cross section of the NAA sample, it can be observed that pores are capped by a thick barrier layer of alumina.

Calibration of pore growth

From SEM analysis calibration of pore growth can be easily elucidated with proper cross-sections. To estimate layer thickness it is crucial that the resulting layer is clearly visible from top to bottom. For this reason, bending of the NAA sample to induce cracking should be avoided for thick samples (i.e. >500 nm). Another important factor to take into account is that the micrograph must be taken perpendicularly to the cross section. Otherwise, false measurements may be obtained due to the unknown tilting angle. The best procedure to obtain such good cross-sections is by selective partial dissolution of the Al bulk in HCl:CuCl saturated solution and subsequent cut of the free-standing NAA membrane close to the remaining Al substrate.

Traditionally, pore growth calibration has been performed relying on the time dependence of the electrochemical reaction (see figure 3.14). However, this is only reliable if the anodization parameters (i.e. voltage, electrolyte composition and temperature) are constant throughout all experiments. This forces to have several calibration curves, one for each electrolyte and voltage associated. Besides, temperature is especially tricky to be perfectly maintained throughout the experiments regardless of the refrigerating system, especially during summer season. For this reason, total charge calibration has been developed in our group (see figure 3.15). Total charge calibration is based on the fact that the anodization of aluminum is mainly governed by the migration of ionic species (i.e. mainly O^{2-}, OH^{-} and Al^{3+}) to the respective electrodes. Therefore, the resulting

current developed in the electrochemical cell during the anodization process is directly proportional to the amount of alumina generated. Thus, this calibration is independent of the anodization parameters as the total charge passed through the electrodes will give us the information about the amount of NAA produced regardless of the electrolyte, temperature, voltage or time. However, this calibration is completely uncertain about the time required for the development of a specific NAA layer thickness, which makes experiment timing tricky if a time-dependent calibration is not available.

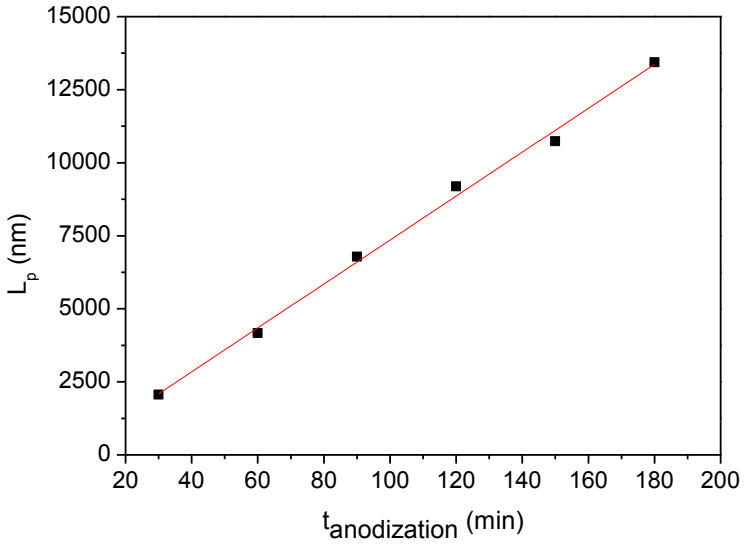

Figure 3.14. Calibration curve of the thickness of NAA for mild anodization in oxalic acid based on time dependence.

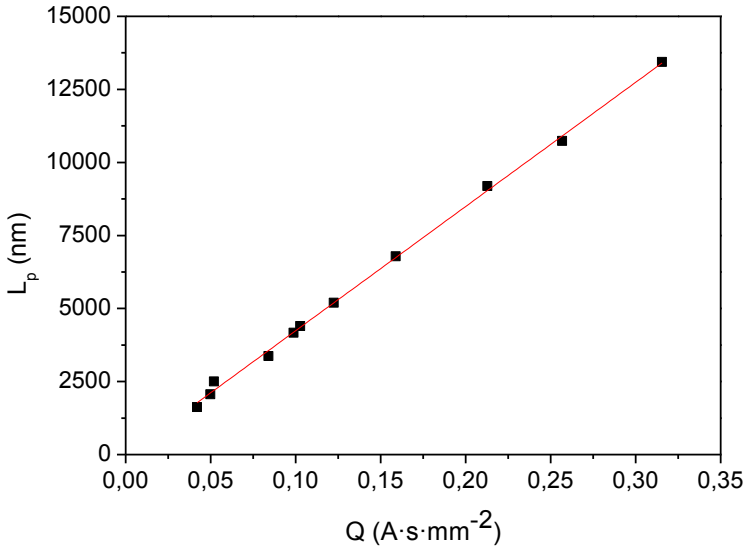

Figure 3.15. Calibration curve of NAA growth based on total charge density. This curve allows a precise control over the growth of NAA independently of electrolyte composition, applied voltage or process temperature.

Calibration of pore widening post-treatments

In order to have full control over the characteristics of NAA, pore diameter calibration is required. The most common technique to achieve NAA with different porosities is by wet chemical etching in phosphoric acid [137, 138, 139, 140, 141]. This post-treatment allows good control over the pore diameter and can be easily calibrated by image analysis of SEM top-views. However, it must be taken into account that the porosity variation for a specific pore widening time (t_{pw}) is strongly dependent on the applied voltage [141]. This could be attributed to the homogeneous dissolution rate of the pore walls. Given a specific dissolution rate, lower voltages result in higher pore density, smaller interpore distance and thinner pore walls. Therefore, the thinner pore walls obtained at

lower voltages result in a faster increase of the porosity by pore widening post-treatments. Another phenomenon that could be attributed for this difference is the variability of electrolyte-associated contamination in the outer oxide layer with the applied voltage. The applied voltage has a direct influence on the amount of electrolyte anions embedded in NAA. This effect can be easily appreciated when comparing samples fabricated in MA and HA conditions in which NAA obtained under high electric fields resulted in a lower anion concentration in the oxide matrix [102]. Therefore, the applied voltage has a direct effect on the oxide composition and thus, on the pore widening rate. This dependency of the pore widening on the applied voltage can be used to our advantage to produce complex NAA samples [142].

During our work, we centered our attention on the fabrication of NAA fabricated in 0.3 M oxalic acid under MA conditions due to its suitable properties for optical biosensing. Figure 3.16 shows the results from the calibration of the pore widening post-treatments in 5 % wt. phosphoric acid at 35 °C. Figure 3.16a and 3.16b show the pore diameter and porosity variation as a function of t_{pw} respectively. Pore diameter obtained after each t_{pw} have more dispersion than the corresponding porosity. This is due to the fact that our method for measuring the porosity from SEM micrographs takes into account the differences in the cell size of each pore and thus, provides a better estimation of the porosity (see appendix A). Interpore distance (figure 3.16c) is not affected by pore widening post-treatments. However, the etching rate (figure 3.16d) is dependent on the t_{pw}. It can be observed that, as alumina is etched, different etching rates are achieved and how the etching rate decays when the etching reaches the inner anion-free alumina layer. This confirms the effect of electrolyte contaminants in the oxide matrix on the pore widening post-treatments.

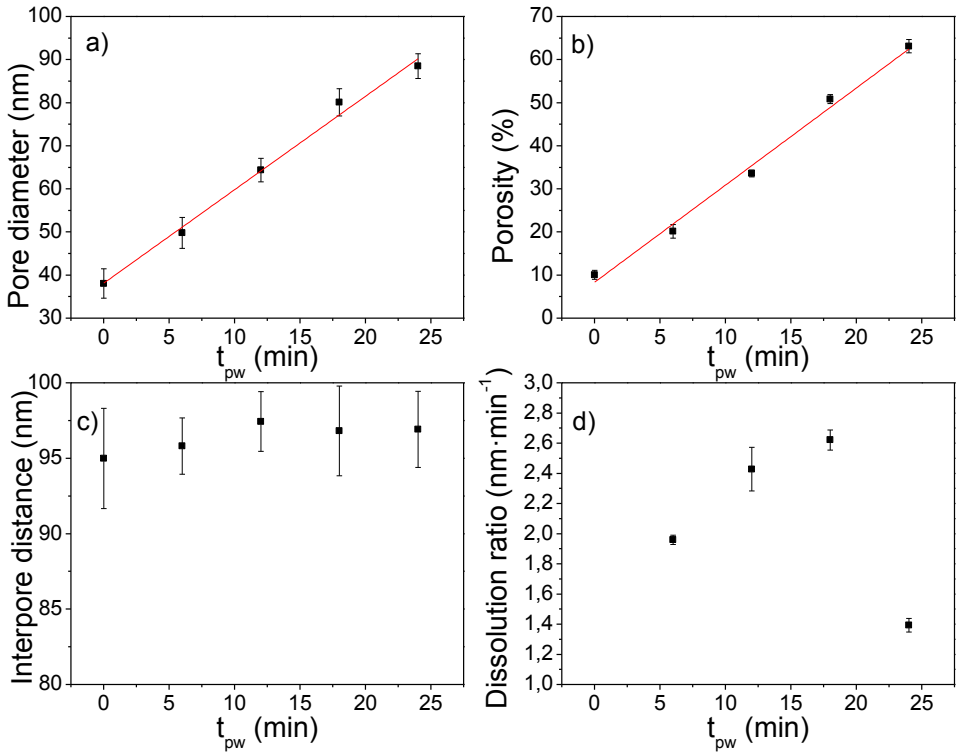

Figure 3.16. Calibration of pore widening post-treatments in NAA manufactured under mild oxalic acid anodization. a) shows the variation of the pore diameter with increasing pore widening time, b) shows the increase of porosity with the increasing pore widening time, c) shows how interpore distance is not affected by the pore widening process and d) shows the different pore widening rates demonstrating that pore wall composition affects the dissolution rates.

3.4.2. OPTICAL CHARACTERIZATION

One of the most important characteristics of NAA is the ability to tune its optical properties by adjusting its structural characteristics. In the following sections, these optical properties will be discussed in detail.

Reflectance

UV-Vis reflectance spectroscopy is the most adequate technique to elucidate the optical characteristics of NAA. This is so due to the high reflectivity of the Al bulk beneath the porous oxide layer. Nevertheless, the properties of this Al substrate can be also be tuned by electrochemical etching. Figure 3.17 shows the reflectance properties of several kinds of Al substrates. As purchased aluminum foils display a low reflectivity of just 40-45 %. This low reflectivity is associated to the high roughness of the foils as a result of the rolling manufacturing procedure. This roughness is of the order of microns which results in a decrease of the reflectance efficiency. Electropolished Al sheets display the highest reflectance of all the studied substrates, even higher than that of our Al calibration mirror. This is due to the extremely low roughness left on the Al after the electrochemical polishing process, which is of the order of just a few nanometers. For comparison, two Al foils were anodized in 0.3 M oxalic acid at 40 V and 5 °C and in 1 % wt. phosphoric acid at 174 V and 0 °C. The resulting NAA films were selectively dissolved in a mixture of 6 % wt phosphoric and 1.8 % wt. chromic acid at 70 °C for 3 h. The reflectance of these textured Al foils was measured and the resulting responses are displayed also in figure 3.17. The aluminum patterned at 40 V showed a slightly lower reflectivity than the electropolished sample. This is a result of the increase of roughness from a few nanometers to some tens of nanometers. However, the aluminum patterned at 174 V displayed a distinct stop-band around 350 nm. This band is a result of the high distance between the pits left on the substrate as a result of the high field anodization (i.e. 440 nm). Since this distance is similar to the wavelength of light, light scattering occurs giving the sample a bluish color and this distinct reflectance curve.

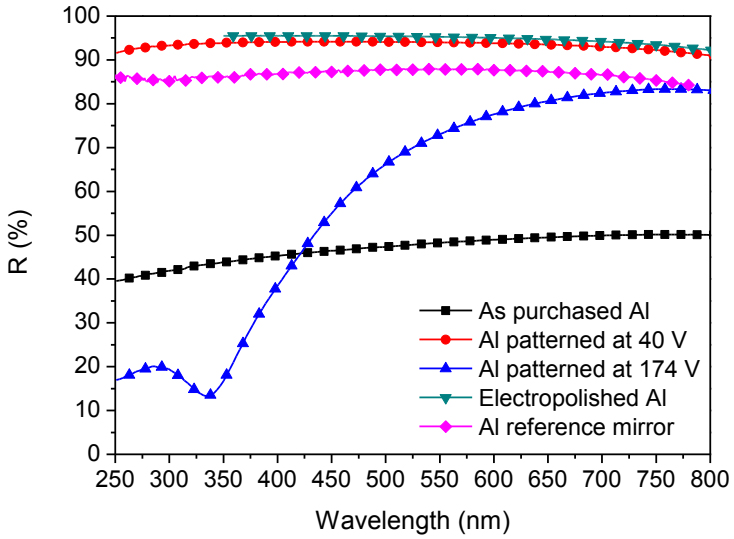

Figure 3.17. Reflectance spectra of different kinds of aluminum substrates. As purchased aluminum foils display a very low reflectivity due to the high roughness, while electropolished foils display the highest reflectivity. Concavities left on the aluminum substrate due to self-ordering decrease their reflectivity due to scattering losses.

Since our goal was to develop optical biosensors based on NAA, we also checked the reflectance properties of the porous oxide films fabricated in both oxalic and phosphoric acid. The results are displayed in figure 3.18. It can be observed how in both cases, overall reflectivity decays as wavelengths approach the ultraviolet region. This can be associated to absorption of the oxide film. In the case of NAA manufactured in phosphoric acid, it can be observed how the scattering present in the Al substrate (see figure 3.17) widens and with just 5 µm, the overall reflectance within the 300-600 nm range falls to 10 %. Moreover, the Fabry-Pérot (F-P) oscillations arising from constructive and destructive interference of the light reflecting at both interfaces of the NAA film are almost

imperceptible in the phosphoric acid sample. This features forced us to work with NAA manufactured in oxalic acid to ensure enough interferences for biosensing.

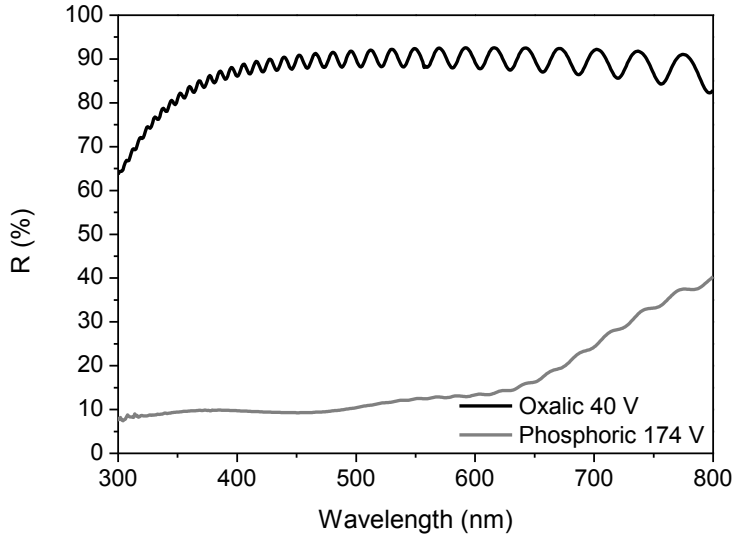

Figure 3.18. Reflectance spectra of 4-µm thick NAA thin films fabricated in oxalic acid 0.3 M at 40 V and 5 °C and with phosphoric acid 1 % wt. at 174 V and 0 °C.

With the aid of a fiber optic spectrophotometer, homogeneity studies of NAA sample fabrication can be performed. To do so, a 36 array of NAA samples were simultaneously anodized. Subsequently, this array was measured with the fiber optic spectrometer and 9 spots of a diameter of roughly 1 mm were measured in each of the NAA of the array. The resulting spectra was analyzed and the effective optical thickness (EOT = 2nL) was obtained. Figure 3.19, shows an EOT map of the samples present in the 36 array. Results show that the samples fabri-

cated simultaneously are highly reproducible. Statistical analysis revealed that a dispersion of just 1.6 % in the EOT was appreciated among the samples. Moreover, if we look at the EOT map, we can observe a redder region displaced from the center of the array. This redder region accounts for a slightly larger EOT in the samples and correlates with the position of the stirrer in the cathode of the electrochemical anodization cell (see figure 3.7b).

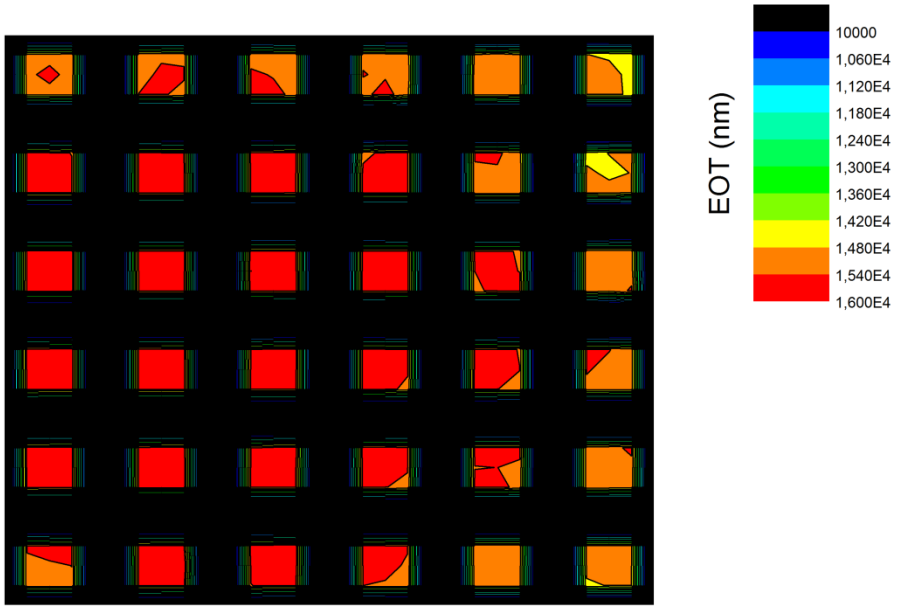

Figure 3.19. EOT map obtained from several measurements on an array of 36 as produced NAA samples. The resulting samples are highly reproducible and display a dispersion of just 1,6 %. The redder region observed correlates with the position of the stirrer in the anodization cell.

Also, with a fiber optic spectrophotometer, it is possible to elucidate the repeatability of the pore widening post-treatment with phosphoric acid. To do so,

the array of 36 NAA samples depicted in figure 3.19 was divided into three sections, and pores were widened for each of the sections for t_{pw} = 0 min, t_{pw} = 10 min and t_{pw} = 20 min. The resulting samples were measured and the obtained EOTs are displayed in figure 3.20. Blue squares represent samples treated for t_{pw} = 20 min, green/yellow samples were treated for t_{pw} = 10 min and red/orange samples are as produced samples (i.e. t_{pw} = 0 min). Figure 3.20 shows that the pore widening treatment is highly repeatable with just a dispersion of 1.6 % for as produced samples (which is in good agreement with the results from figure 3.19), 1.4 % for t_{pw} = 10 min, and 1.8 % for t_{pw} = 20 min.

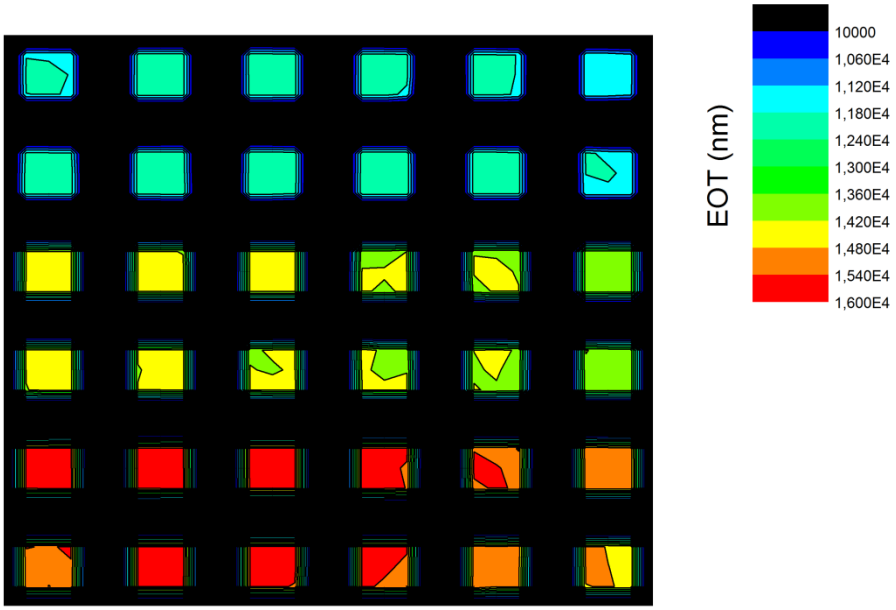

Figure 3.20. EOT map of a 36 NAA array after applying a pore widening post treatment for t_{pw} = 0 min (red and orange region), t_{pw} = 10 min (yellow and green region) and t_{pw} = 20 min (blue region). The results obtained show a high reproducibility with a dispersion of 1,6, 1,4 and 1,8 % respectively.

Nevertheless, even though the EOT maps display homogeneities higher than 98 %, this is not enough repeatability for biosensing as increments in EOT (ΔE-

OT) are typically < 1%. Real-time sensing of exactly the same spot overcomes this issue. Since the measured spot is always the same, sample's inhomogeneity does not affect the measurement and all the ΔEOT registered can be adscribed to changes in the properties of the NAA film. Therefore, if proper functionalization has been applied to the pores' surface, ΔEOT will account for the biochemical interaction between the receptor attach to the pores and its specific analyte.

Apart from the repeatability assessment, these 2-D graphs allow us to see the EOT of the samples depending on the exact spot on the sample.Therefore, if enough spectrometer channels are available, dispersion within and between samples can be measured, which is particularly interesting for the development of sensing platforms.

Photoluminescence

Back in 1999, it was found that NAA fabricated in either oxalic or sulfuric acid displayed a strong blue photoluminescence upon UV illumination [143]. From then on, efforts have been focused on studying the properties and applications of the photoluminescence of NAA [144, 145, 146, 147, 148, 149, 150, 151, 152, 153, 154, 155]. Photoluminescence (PL) behavior has been reported for sulfuric, oxalic acids and recently, malonic acid. NAA fabricated under conventional two-step oxalic acid anodization has been the most studied for having the strongest PL response [143]. Figure 3.21 shows the PL from as produced NAA films with different thicknesses.

The oscillations displayed are a result of the F-P interferences due to the thin nature of the NAA films. It can be appreciated how photoluminescence increases with layer thickness. The PL emission of NAA results from the sum of two

different emissions. Most of the authors coincide in the fact that one of these emissions (centered around 420 nm) comes from ionized oxygen vacancies (also known as F^+ centers) in the porous matrix, while the second peak (also known as F centers, centered around 480 nm) is associated with oxalate impurities embedded in the oxide [147, 153].

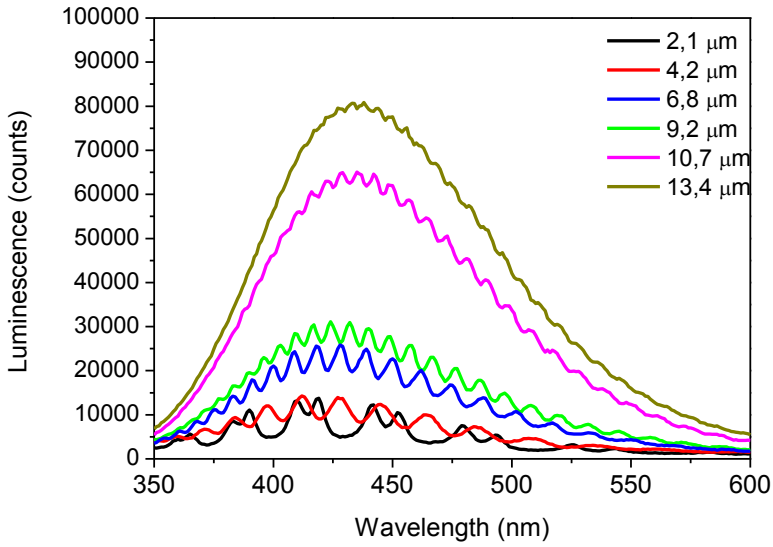

Figure 3.21. Photoluminescence spectra of NAA samples manufactured in oxalic acid with different thicknesses. The resulting spectra display F-P oscillations due to the thin nature of the NAA films.

Effect of annealing

The PL response of NAA has been reported to be enhanced with heating post treatments [145, 151, 153]. Thermal annealing increases the PL intensity until 500 °C. This increase has been associated to an increase of the amount of F^+

centers [143] as well as chemical modification of the oxalate impurities [147]. Further increase of the temperature leads to an abrupt decrease in the PL response due to annihilation of the F^+ centers due to oxygen migration and conversion of oxalate anions to CO_2.

Effect of etch treatment

Apart from annealing, wet chemical etching of the pores in NAA can also alter the PL emission. In an initial work, it was reported that increasing the etching time resulted in an increment of the PL intensity [149]. This increase was associated to a better excitation of the F^+ centers situated deeper in the pore walls. However, this work was based on thick NAA films (i.e. $\geq$ 24 μm). In our lab we performed a similar experiment with multiple thicknesses. Figure 3.22 and 3.23 display the results.

The color map depicted in figure 3.22 shows the photoluminescence distribution of a total of 30 samples with thicknesses ranging from 2.5 to 14 μm and etched with 5 % wt. phosphoric acid at 35 °C for up to 24 min. Results show a considerable increment of the photoluminescence intensity as a function of the anodization time as expected by the increasing amount of luminescent material. Apart from that, for thick samples it is observed that after an initial decrease of the PL signal, increased emission is observed between 10 and 20 min of etching followed by a sharper decrease of the photoluminescence for longer etching times. This is in good agreement with the previously reported results [149].

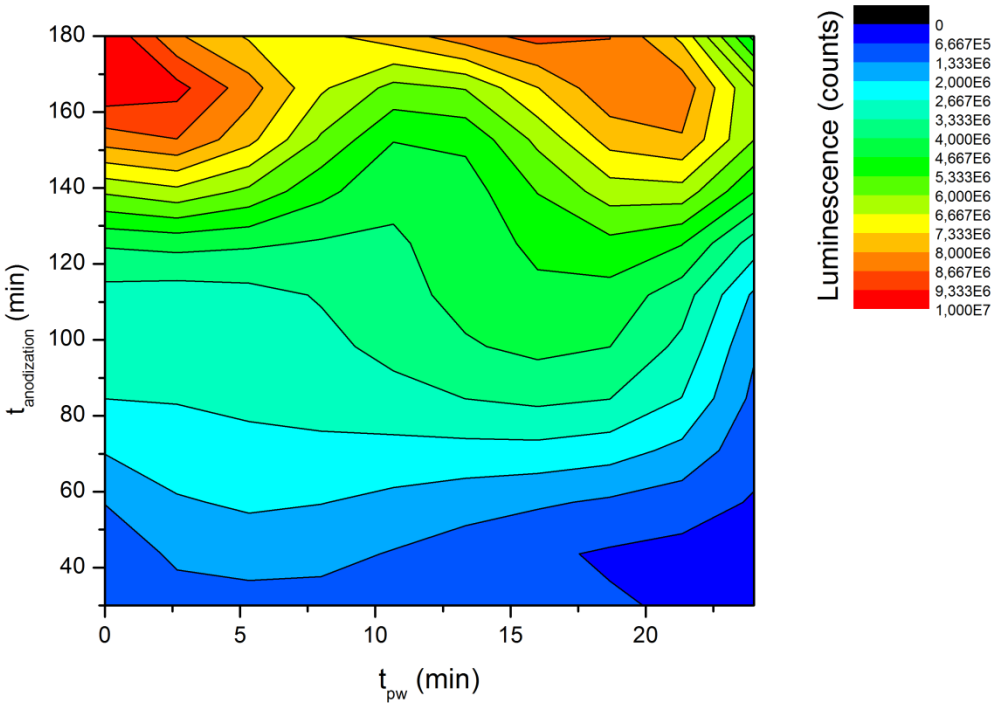

Figure 3.22. Contour plot showing the effect of pore widening on the photoluminescence of NAA thin films fabricated in oxalic acid with different thicknesses.

Figure 3.23 shows the increment in the PL response of the NAA films with increasing etching treatments. It can be observed that longer etching times do not always result in an increment of the PL emission. In fact, for samples around 2 -2.5 µm, the emission reduces with the etching time. As the film thickness increases, regions in which the emission of the sample increases with wet chemical etching of the pores start to appear. The time range of these regions depends on the anodization time. As samples become thicker, more etching is required to observe an increment in the PL emission. This is in good agreement with previously reported results based on samples anodized for 4 h [149]. The reasons for these differences in the PL response as a function pore wall etching are related with the total amount of luminescent centers available. F^+ centers are located

deeper in the pore wall while oxalate impurities are available in the outer oxide layer. Dissolution of pore walls allows better excitation of luminescent centers inside pore walls (i.e. mainly F^+ centers). However, if the sample's thickness is too thin, the total number of F^+ centers is reduced and most of the photoluminescence available is related with the oxalate species present in the outer oxide layer. Thus, if sample thickness is too thin, pore widening post-treatments will result in a decrease of the overall photoluminescence. Nevertheless, if sample thickness is thick enough, the enhanced excitation of luminescent centers located deeper at the pore walls will result in an enhancement of the overall photoluminescence.

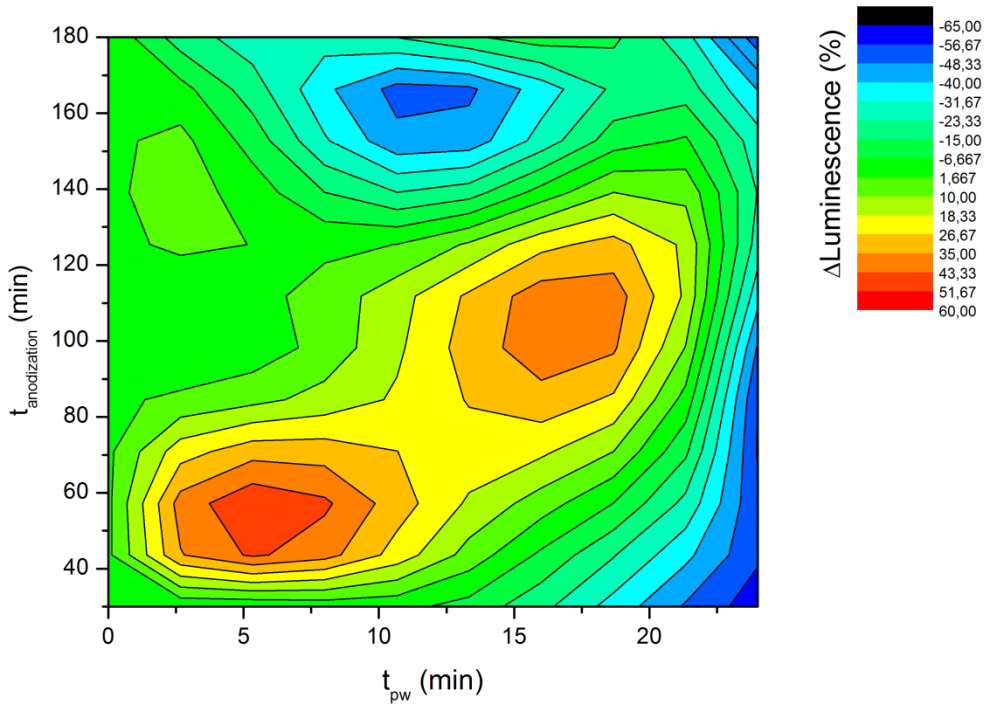

Figure 3.23. Contour plot displaying the increment induced in the photoluminescence intensity of NAA thin films with different thicknesses by pore widening post treatments.

Refractive index

With the data from SEM, reflectance UV-Vis spectroscopy and PL analysis it is possible to elucidate the effective refractive index (n_{eff}) of NAA thin films as well as the refractive index of the alumina bulk (n_{bulk}).

n_{eff} of NAA thin films can be obtained from the position of the interferences by the Fabry-Pérot relationship (eq. 3.9):

$$m\lambda = 2n_{eff}L_p\cos\theta \quad (3.9),$$

Where m is the order of the oscillation, λ is the position of the maximum, n_{eff} is the effective refractive index of the layer, L_p is the physical thickness of the layer and θ is the refraction angle.

For two consecutive maxima, the expressions are:

$$m\lambda_m = 2n_{eff}L_p\cos\theta$$

And

$$(m+1)\lambda_{m+1} = 2n_{eff}L_p\cos\theta \quad (3.10)$$

Therefore, if the position of two conscutive oscillations is known, n_{eff} can be calculated from the reflectance spectrum by the following equation:

$$2n_{eff}L_p\cos\theta\left(\frac{1}{\lambda_{m+1}}-\frac{1}{\lambda_m}\right)=1 \quad (3.11)$$

However, normally the refraction angle θ is not known. For this reason eq. 3.11 has to be transformed so as to be in terms of the incidence angle (θ_0):

$$n_{eff}=\sqrt{\sin^2\theta_0+\left[2L_p\left(\frac{1}{\lambda_{m+1}}-\frac{1}{\lambda_{m+1}}\right)\right]^{-2}} \quad (3.12)$$

Since the n_{eff} can be obtained from F-P oscillations, n_{eff} can be calculated from either reflectance or PL spectra. Figure 3.24 shows the resulting n_{eff} obtained from the analysis of both reflectance and PL spectra of NAA with different thicknesses and porosities. It can be appreciated that both methods display a similar n_{eff} and a linear relationship with the porosity of the NAA film.

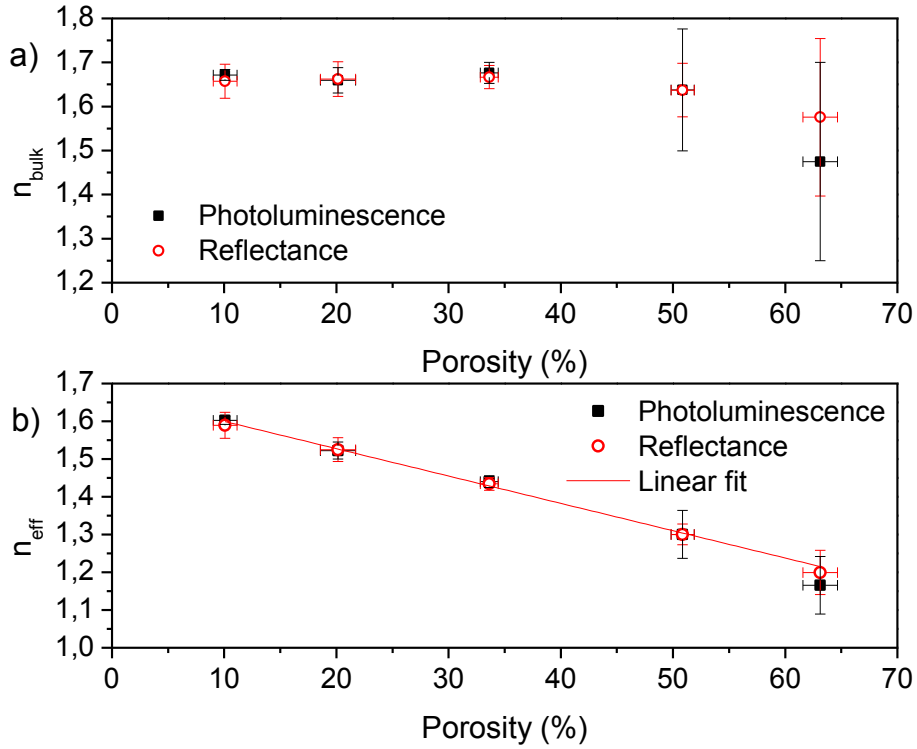

Figure 3.24. Dependence of the refractive index of anodic alumina bulk (n_{bulk}) estimated from the fitting with Bruggema's effective medium approximation (a) and of NAA n_{eff} (b) as a function of porosity. Results are obtained from photoluminescent and reflectance data of four sets of samples with known thickness and porosity estimated from SEM analysis. n_{bulk} data was obtained applying Bruggeman's effective medium approximation and show good agreement with the intercept obtained from the linear fitting of n_{eff} at P = 0 %.

In order to extract the n_{bulk}, it is necessary to know the porosity of the NAA film. If porosity is known, then effective medium approximation can be applied to elucidate n_{bulk}. For this reason, SEM analysis is a must to obtain n_{bulk}. Results presented in figure 3.24 show n_{bulk} calculated from Bruggeman's equation (eq. 3.13):

$$(1-P)\frac{n_{bulk}^2-n_{eff}^2}{n_{bulk}^2+2n_{eff}^2}+P\frac{n_{medium}^2-n_{eff}^2}{n_{medium}^2+2n_{eff}^2}=0 \qquad (3.13)$$

Where P is the porosity of the film, n_{bulk} is the refractive index of bulk alumina, n_{eff} is the effective refractive index of the layer and n_{medium} is the refractive index of the material filling the pores.

The values obtained with Bruggeman's effective medium approximation are in good agreement with the 0 % porosity of linear fitting ($n_{bulk} \approx n_{P=0\%} \approx 1.67$) of the refractive indexes obtained from both reflectance and PL spectra with the F-P relationship (eq. 3.9).

3.5. APPLICATIONS OF NANOPOROUS ANODIC ALUMINA

The unique characteristics of NAA make it an interesting material for the development of novel nanostructured materials. Up to date, NAA has been used as a template for the synthesis of nanomaterials [156, 157], as a mask for the deposition of ordered arrays of nanoparticles [158], as a selective membrane for molecular separation [159, 160], as a reactor for catalysis [161, 162], as a drug delivery system [163], as a sensor [164, 165], and as a scaffold for tissue engineering [166, 167, 168].

CHAPTER IV

INTERFEROMETRIC BIOSENSING WITH NANOPOROUS ANODIC ALUMINA MONOLAYERS

4.1. OPERATING PRINCIPLE OF RIFS

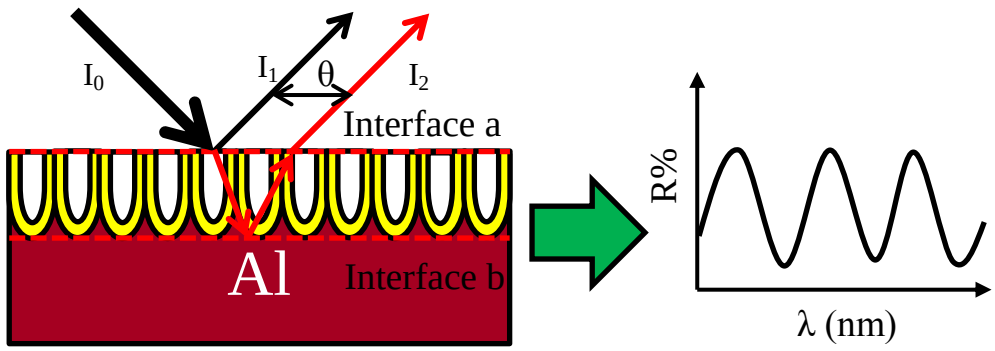

Figure 4.1. Schematic representation of the working principle of NAA monolayer optical interferometric biosensors.

Reflectance interferometric spectroscopy (RIfS) is an optical technique used to analyze the characteristics of thin films by examining their reflection upon white light illumination. As depicted in figure 4.1, when white light (I_0) illuminates the sample, part of the light is reflected (I_1) at the top interface (interface a) and part of the light (I_2) travels through the NAA film until it is reflected at the pores' bottom (interface b). The superposition of these two light waves (i.e. I_1 and I_2) generates a series of constructive and destructive interferences (i.e. an oscillatory fingerprint). The position of these interferometric fringes is governed by the Fabry-Pérot relationship (eq.4.1):

$$m\lambda = 2nL \qquad (4.1)$$

Where m is the order of the oscillation (integers for constructive interference and half integers for destructive interferences), λ is the wavelength of the oscil-

lation, n is the effective refractive index of the thin film and L is the thickness of the film.

According to equation 4.1, shifts in the position of the interferometric fingerprint may be related to either thickness variations or refractive index variations. In an initial work, planar RIfS biosensors were developed. These devices relied on the measurement of thickness variations by matching the refractive index of the thin film with the refractive index of the biochemical adlayer ($n_{layer} \approx n_{biolayer} \approx 1.45$) [169]. Soon after, pSi was proposed as an alternative to planar RIfS [55]. These porous materials resulted in more noticeable shifts in the signal as a result of the higher surface area available for analyte capture. However, their signal was a result not only of the changes in the thickness of the interferometric cavity, but also the changes of the refractive index of the matter filling pores. In fact, the changes in the thickness of the thin film are almost negligible compared to those resulting from the effective refractive index. Nevertheless, in order to avoid distinguishing between analyte binding on top and inside the device, changes are often based on effective optical thickness (EOT = 2nL) shifts.

4.2. BIOSENSING SIGNAL

RIfS-based biosensors can monitor analyte capture using three main approaches as depicted in fig. 4.2: performing a fast Fourier transform of the spectrum [57], plotting the mode versus the inverse of the wavelength position and directly following the position of one of the fringes [10].

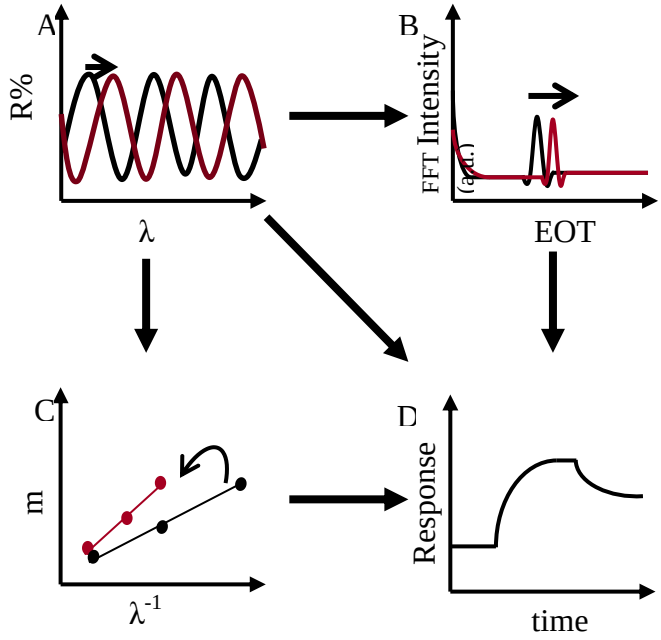

Figure 4.2. Schematic representation of three different ways to obtain the biosensing signal using RIfS. A) shows the shift in the position of the interference fringes as a result of analyte capture; B) shows the fast Fourier transforms of the interferograms in A whose peak allows monitorization of the binding event; C) order versus the inverse of the position of the interference fringes whose slope allows monitorization of the biochemical reaction; and D) direct tracking of the position of one of the interference fringes to monitor analyte capture.

4.2.1. Fast Fourier transform (FFT)

The FFT consists in performing a Fourier transform of the interference spectrum to convert the multiple oscillations into a single lorentzian peak. The resulting peak can be easily tracked and its position corresponds to the EOT of the porous film.

Due to the nonlinear nature of the wavelength spectrum, FFT cannot be performed directly from the acquired spectrum. The following pretreatment of the signal is required [59]:

1. **The wavelength (λ, nm) is converted to wavenumber (λ^{-1}, nm^{-1}) by inverting the x axis of the spectrum.** This renders equispaced oscillations, which is necessary to perform a FFT, but data points are distributed at different intervals.
2. **Then, a cubic interpolation is performed in order to redistribute and redimension the data to 4096 points.** In order to perform a FFT, it is necessary that data points are equispaced on the x axis. This interpolation spaces data points at a fixed interval.
3. **The resulting spectrum is windowed using a Hanning window.** The edges of the interferometric spectrum analyzed are truncated sharply. This normally results in unwanted sidelobes next to the FFT peak. To avoid this, it is necessary that the edges of the data analyzed are equal to 0. Windowing modifies the overall shape of the spectrum without affecting the oscillation frequency.
4. **Finally, the data is zero-padded to the power of two.** This final pretreating step consists in adding 0s at the end of the data. These 0s do not affect the data, but improve the overall resolution of the FFT spectrum.

This technique is approximately correct and sufficient for most sensing applications. Nevertheless, it assumes that the refractive index is constant at all wavelengths. Even though this is not true, if the wavelength range is sufficiently small, the variation of the refractive index within the range studied could be considered constant and the related errors could be regarded as negligible.

4.2.2. MODE VERSUS POSITION

According to eq. 4.1, it is possible to elucidate the EOT from the position of the oscillations in the wavelength spectrum.

$$m\lambda = 2nL \rightarrow m = 2nL\frac{1}{\lambda} \tag{4.2}$$

As seen in eq. 4.2, to find the EOT it is necessary to plot the order m of each oscillation versus the inverse of its position in the wavelength spectrum. This transformation allows us to have a linear relationship between the order of the oscillation and its position (see fig. 4.3).

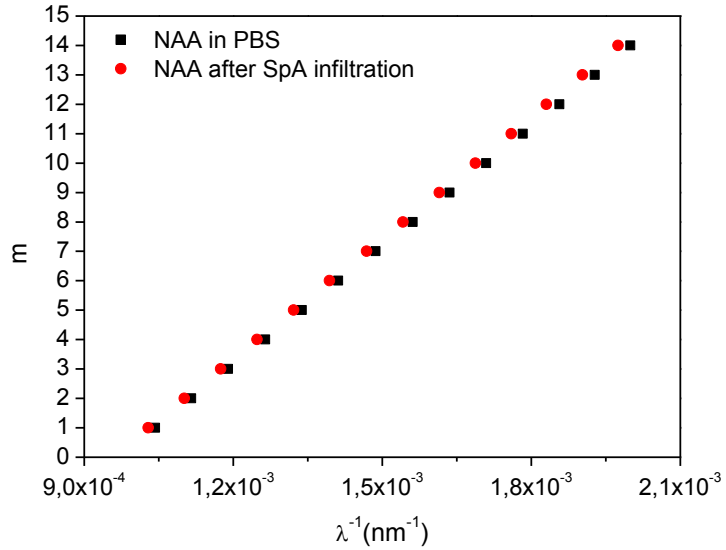

Figure 4.3. Experimental data obtained from a 4-µm thick NAA thin film before and after the infiltration of protein A from staphylococcus aureus using the RIfS setup.

As depicted in fig. 4.3, after protein infiltration there is a shift in the position of the oscillations. With this method, what is actually measured is the slope of the m versus λ^{-1} which according to eq. 4.2 corresponds to the EOT of the layer. Therefore, upon protein immobilization or analyte binding, an increase in the slope would be detected.

This method, even though correct, it is not normally used in the literature. This is due to the fact that the FFT method is superior when analyzing complex interferometric patterns (see chapter V), and it is more complicated than direct fringe monitorization.

4.2.3. DIRECT FRINGE MONITORIZATION

Another method which could be used to monitor the biochemical reaction is directly following the position of one of the oscillations in the spectrum [10]. This is supported by eq. 4.1, as the shift in position of the mode is directly related with a change in the EOT. This method is particularly interesting for thin layers (< 1 μm), as the available oscillations is reduced and therefore insufficient to perform a FFT analysis. Similarly, if the thickness of the film allows a FFT analysis, it is not recommended to perform a direct fringe monitorization. This is so due to the fact that for thick films (i.e. ≥ 4 μm), even though eq. 4.1 is still valid, the greater amount of oscillations in the same region results in reorganization of the interference fringes. This means that some interferences redshift and others blueshift in order to accommodate the new higher EOT.

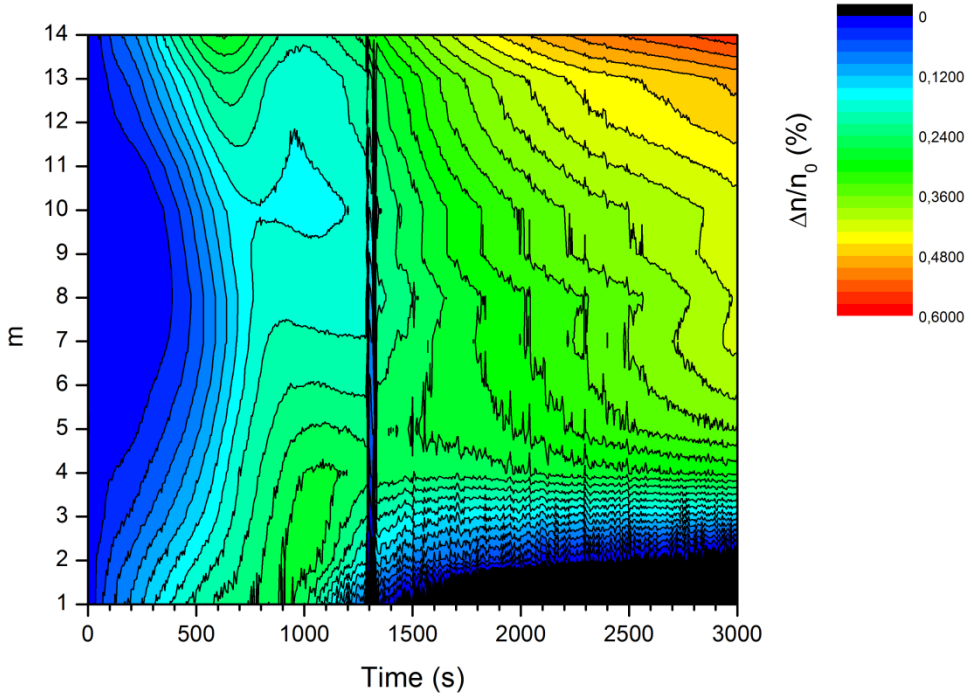

Figure 4.4. Surface plot of the oscillation shift in each of the fringes of a 4-µm thick NAA sample upon drop-wise infiltration of protein A as a function of time. The black thick line at 1300 s marks the start of protein A infiltration.

Fig 4.4 shows an experimental result of direct fringe monitorization of the oscillations in the 400-900 nm range on a 4 µm-thick NAA sample upon infiltration with protein A. It can be observed how each interference fringe has a different response to the infiltration of protein A. Even though most tend to redshift, modes 1 and 2 present a blueshift behavior, and modes 3 and 4 show almost no response to protein A infiltration. Therefore, if these fringes were used to analyze the performance of the biosensor, they would result in false negatives whereas the FFT method would give a more accurate estimation of the biosensing response.

4.3. TRANSDUCER DESIGN

The development of biosensors requires deep knowledge of the properties of the material used in the bioreceptor-loaded interface as well as the detection technique used. In the previous section, we have discussed the operating principles of RIfS biosensing. It has been explained how the interference spectrum arising from white light illumination on a thin film depends on the EOT of the layer (eq. 4.1). Therefore, accurate tuning of the nanostructure of the thin film to match a certain EOT could lead to more accurate and sensitive optical biosensors.

In the case of NAA monolayers, the nanostructure can be easily adjusted by means of interpore distance, pore diameter, layer thickness and metal deposition on top of the layer.

4.3.1. EFFECT OF INTERPORE DISTANCE

One of the key parameters during the fabrication of NAA films is the applied voltage, which in turn, controls the interpore distance. This parameter is crucial as it will limit the possible pore diameters available for the structure.

Fig. 4.5 shows the effect of different interpore distances (50, 100, 150, 200 and 250 nm) in the refractive index of the structure. Larger interpore distances than the ones displayed in fig 4.5 were not studied due to their light scattering properties (see chapter III, fig. 3.18). The values displayed for the different pore diameters studied were calculated using Bruggeman's effective medium approximation. It can be observed how the slope of the refractive index decreases as the applied voltage (i.e. interpore distance) increases. Also, it can be observed

how larger interpore distances allow us to work with a wider range of pore diameters as well as larger pores. These are important features since it can be seen how interpore distance, pore diameter and refractive index are intimately related. Therefore, depending on the size of the molecule we want to detect, an appropriate interpore distance should be chosen, taking into account that smaller interpore distance will lead to more sensitive refractive index variations.

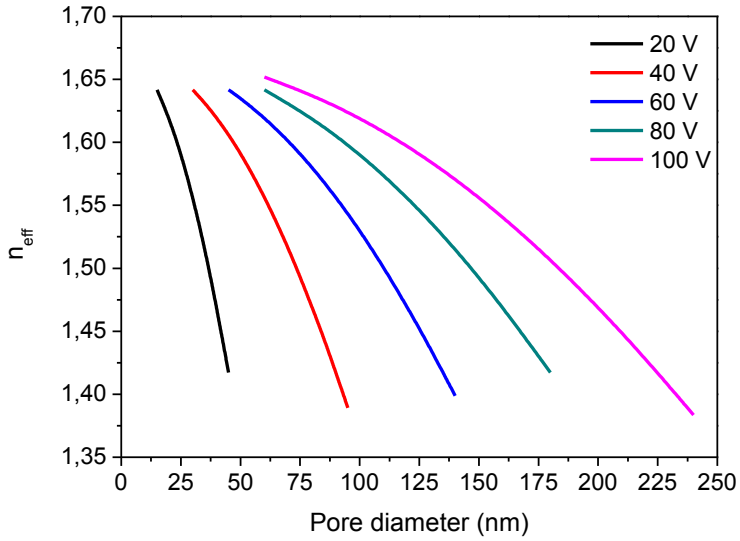

Figure 4.5. Calculated refractive index for NAA films fabricated at 20, 40, 60, 80 and 100 V with their available pore diameters. These applied voltages correspond to 50, 100, 150, 200 and 250 nm interpore distance respectively.

4.3.2. EFFECT OF PORE DIAMETER

As it has been explained in the previous section, interpore distance plays a key role in the refractive index variation slope as well as in the available pore

diameters for biomolecule immobilization. However, once this feature is fixed, the next crucial parameter that plays a key role in the design of NAA-based optical biosensors is the pore diameter [170, 171, 172].

Theory

The EOT of a NAA film measured in reflection depends on the effective refractive index of the layer (n_{eff}) and its thickness (L) (see eq. 4.1). This means that both Δn_{eff} and ΔL can produce a shift in the EOT. However, since for RIfS biosensing thick layers (i.e. > 4 µm) are required, typically the effect of ΔL is negligible when compared to Δn_{eff}. Therefore, we can approximate that $\Delta EOT \approx k\Delta n_{eff}$.

Once we have established that the ΔEOT is directly dependent on n_{eff}, the link between the sensitivity of the NAA film and the pore diameter becomes clearer. Nevertheless, before developing a model, it is necessary to fully understand the working principle of biosensing in NAA films.

The refractive index of a NAA layer depends on the refractive index of the bulk alumina ($n_{alumina} \approx 1.67$), the refractive index of the material filling the pores (in this case PBS pH 7.4, $n_{PBS} \approx 1.33$) and their respective volume fractions.

$$n_{eff} = f_1(n_{alumina}) + f_2(n_{PBS}) \quad (4.3)$$

Where f_1 and f_2 represent the volume fractions of each material.

When a biomolecule is attached, eq. 4.3 changes as some of the PBS is replaced by the biomolecule and therefore a third term corresponding to the biomolecule refractive index must be added ($n_{biomolecule} \approx 1.45$).

$$n_{eff} = f_1(n_{alumina}) + (f_2 - f_3)(n_{PBS}) + f_3(n_{biomolecule}) \quad (4.4)$$

It can be observed how the volume fraction of the bulk alumina remains constant throughout the process, but the volume fraction of the PBS reduces due to the incorporation of the biomolecule. Therefore, since the refractive index of the biomolecule is larger than the refractive index of PBS, the EOT of the NAA film will increase (i.e. redshift) upon infiltration with biomolecular analytes.

Model

In order to simulate the effect of pore diameter on the performance of NAA films for biosensing, a model has been developed a model based on Bruggeman's effective medium approximation [155]:

$$P_1 \frac{n_{alumina}^2 - n_{eff}^2}{n_{alumina}^2 + 2n_{eff}^2} + P_2 \frac{n_{PBS}^2 - n_{eff}^2}{n_{PBS}^2 + 2n_{eff}^2} + P_3 \frac{n_{protein}^2 - n_{eff}^2}{n_{protein}^2 + 2n_{eff}^2} = 0 \quad (4.5)$$

Where P_1, P_2 and P_3 represent the volumetric fractions of alumina, PBS and protein respectively; and $n_{alumina}$, n_{PBS}, $n_{protein}$ and n_{eff} represent the refractive indexes of bulk alumina, PBS, protein and the effective refractive index of the structure respectively.

Thanks to the self-ordering properties of alumina, the porosity (P)can be calculated from its geometric features and extract P_1:

$$P = \frac{\pi}{2\sqrt{3}}\left(\frac{D_p}{D_{int}}\right)^2 \quad (4.6)$$

Where D_p is the pore diameter and D_{int} is the interpore distance.

Knowing the porosity of the NAA sample, it is possible to calculate P_1 as follows:

$$P_1 = 1 - P \quad (4.7)$$

In order to calculate P2 and P3, it is necessary to know the amount of protein inside the structure. To do so, we assumed that the proteins formed a complete monolayer on the inner surface of the pores of NAA. Therefore, P_2 can be calculated as follows:

$$P_2 = \frac{\pi}{2\sqrt{3}}\left(\frac{D_p - 2t}{D_{int}}\right)^2 \quad (4.8)$$

Where t is the thickness of the protein adlayer. This thickness depends on the size of the target protein. A typical protein for biosensing assays is immunoglobulin G (IgG) whose size is roughly 10 nm. However, even with full coverage of the pore surface with IgG, considering a thickness of 10 nm in the adlayer is not appropriate, since the voids between two adjacent proteins, due to inherent shape of the proteins themselves, provoques a certain roughness on the pore surface. For this reason, for the simulation purpose, we assumed a solid thickness t = 5 nm in order to be able to compare the shifts in n_{eff}.

Finally, P_3 can be deducted from equations 4.8 and 4.6.

$$P_3 = P - P_2 = \frac{\pi}{2\sqrt{3}}\left[\left(\frac{D_p}{D_{int}}\right)^2 - \left(\frac{D_p - 2t}{D_{int}}\right)^2\right] \quad (4.9)$$

Thus applying eq. 4.6-4.9 to eq. 4.5 leads to the following expression:

$$\left[1 - \frac{\pi}{2\sqrt{3}}\left(\frac{D_p}{D_{int}}\right)^2\right]\frac{n_{alumina}^2 - n_{eff}^2}{n_{alumina}^2 + 2n_{eff}^2} + \frac{\pi}{2\sqrt{3}}\left(\frac{D_p - 2t}{D_{int}}\right)^2 \frac{n_{PBS}^2 - n_{eff}^2}{n_{PBS}^2 + 2n_{eff}^2} + + \frac{\pi}{2\sqrt{3}}\left[\left(\frac{D_p}{D_{int}}\right)^2 - \left(\frac{D_p - 2t}{D_{int}}\right)^2\right]\frac{n_{protein}^2 - n_{eff}^2}{n_{protein}^2 + 2n_{eff}^2} = 0 \quad (4.10)$$

From eq. 4.10 it is possible to see how n_{eff} is directly connected to the key parameters of the self-ordered NAA pores, namely pore diameter (D_p) and interpore distance (D_{int}). In a previous section we already discussed the effect of D_{int} on the performance of NAA optical sensors and demonstrated how neff was more sensitive for smaller D_{int}. Once this has been stablished, with equation 4.10 it is possible to predict the response of n_{eff} for different pore diameters.

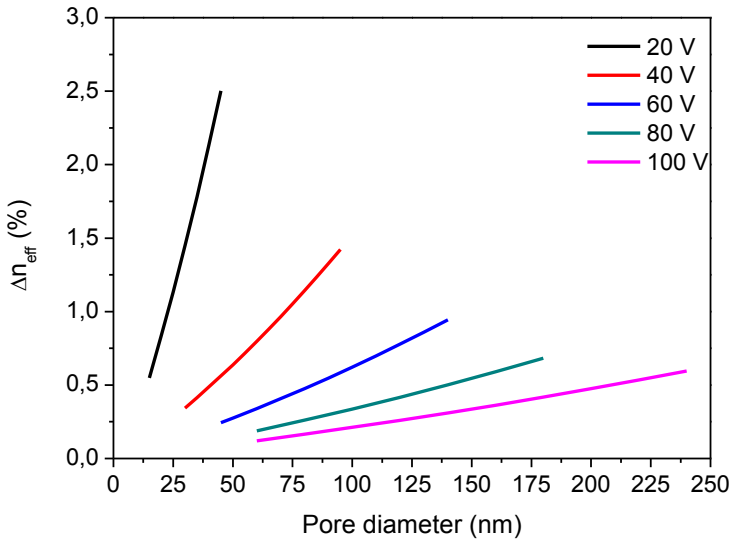

Figure 4.6. Calculated Δn_{eff} upon attachment of a 5 nm-thick biomolecular layer on the pore surface for NAA films anodized between 20 and 100 V as a function of pore diameter.

Fig. 4.6 shows the effect of pore diameter after the attachment of a 5 nm-thick protein layer on the pore surface. This effect is calculated for 5 different anodization conditions (20, 40, 60, 80 and 100 V) which result in interpore distances of 50, 100, 150, 200 and 250 nm. It can be observed how, regardless of the interpore distance used in the calculation, the highest Δn_{eff} observed corresponds to the largest pore diameter.

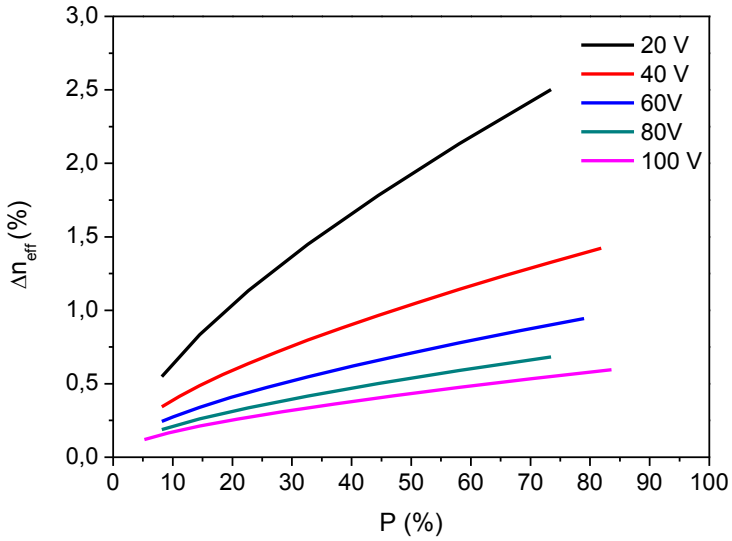

Figure 4.7. Calculated Δn_{eff} upon attachment of a 5 nm-thick biomolecular layer on the pore surface for NAA films anodized between 20 and 100 V as a function of the sample's porosity.

Experimental results

With the model described in the previous section, it has been demonstrated how the pore diameter exerts a major effect on the Δn_{eff} after biomolecule im-

mobilization. However, this model is not perfect and do not assess experimental features such as steric effects. In order to see other possible effects of pore diameter on the performance of NAA optical biosensors, it has been decided to study three different pore diameters and monitor the sequential infiltration of three intereacting model proteins: protein A, human IgG and anti-human IgG [173].

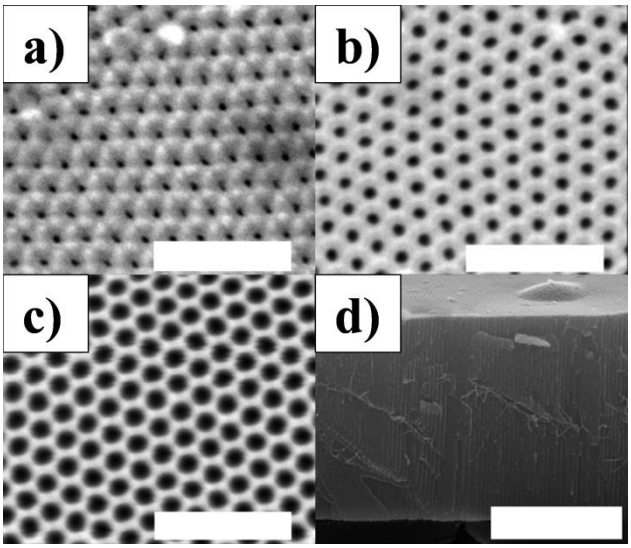

Figure 4.8. SEM micrographs of NAA manufactured under conventional oxalic acid anodization conditions with three different porosities for the optimization of pore diameter in NAA-based RIfS biosensors. A) P = 9.1 ± 2.3 %, B) P = 25.3 ± 3.4 % and C) P = 51.5 ± 4.3 % (scale bar = 500 nm); and D) cross-sectional view of NAA layer depicted in A) showing a Lp = 4.6 ± 0.1 μm (scale bar = 3μm). Adapted from [173]

Fig. 4.8 shows the SEM micrographs of the NAA samples used in this study. The samples were fabricated in 0.3 M $H_2C_2O_4$ using the well-known two-step

anodization procedure already explained in chapter III. The anodization voltage used throughout the fabrication of the NAA films was maintained to 40 V in order to yield a D_{int} = 100 nm. This interpore distance is not the most sensitive depicted in figs. 4.6 and 4.7, but was chosen due to the size of the biomolecules used (≈ 10 nm each). The sum of the three proteins conjugated would result into a biomolecular assembly of roughly 30 nm. Thus, the range of pore diameters that could be studied in NAA samples manufactured at 20 V in sulfuric acid would be reduced to 30-40 nm in order to maintain the structural integrity of the layer.

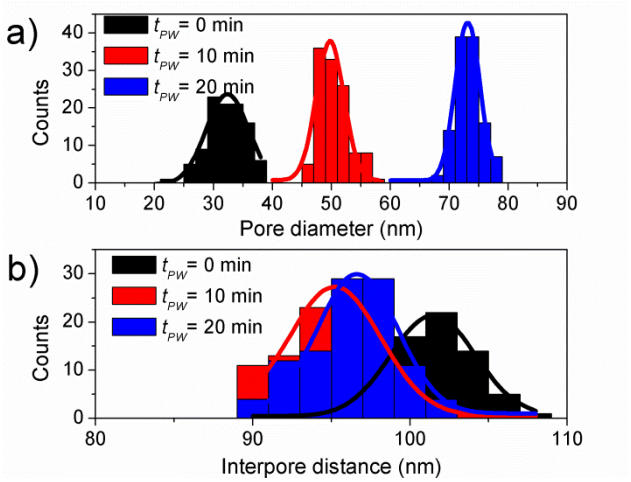

Figure 4.9. Histogram of (a) pore diameter distribution (D_p), and (b) interpore distance (D_{int}) resulting from the image analysis of the micrographs depicted in fig. 4.8. Adapted from [173]

Thanks to the unique self-ordering properties of NAA highly repeatable interpore distances in the range of 90-105 nm can be achieved as shown in figure 4.9. This high repeatability allows us to compare the experimental results from the different samples with minimal error. Moreover, the pore diameter distribu-

tions achieved are narrow (32 ± 4 nm, 50 ± 3 nm and 73 ± 2 nm) and do not intersect with each other. These features ensure that our experiments will be focused on monodispersed pores and will not be biased by interpore diffusion of proteins.

The real-time measurements were performed using an Avantes spectrophotometer and a halogen light source. The infiltration of the proteins inside the porous structure was made in a custom-made flow cell following this procedure:

1. PBS was flowed for 30-60 min in order to acquire a baseline for the biosensing experiment.
2. Then, a 100 $\mu g \cdot mL^{-1}$ SpA solution was flowed until signal stabilization was achieved. SpA is an IgG-binding protein capable of capturing human IgG in a directional manner (i.e. through the cell binding (Fc) portion) that attaches to the pore walls due to electrostatic interactions. Therefore, this step serves as a biofunctionalization step for the NAA surface.
3. A PBS wash of 30 min is then applied to the NAA biosensor. This wash allows us to eliminate unbound or loosely bound SpA from the pore surface.
4. Subsequently, a human IgG solution was flowed into the cell. This step is the sensing step. In this study, we used two different concentrations in order to assess the effect of the pore diameter on the sensitivity of NAA optical biosensors:
    a. 10 $\mu g \cdot mL^{-1}$
    b. 100 $\mu g \cdot mL^{-1}$
5. Then PBS was flushed for 30 min to wash away the unbound and loosely bound human IgG from the porous structure.
6. Afterwards, a fixed concentration of 100 $\mu g \cdot mL^{-1}$ anti-human IgG was flowed. This step serves as an amplification step. This anti-human IgG antibody is able to attach onto the two main aminoacids chains of human IgG: the heavy and the light chain. Since each human IgG molecule has 2 heavy and 2 light

chains, each human IgG molecule provides enough binding sites for 4 anti-human IgG antibodies. This allows us to amplify the resulting signal from step 4.

7. Finally, PBS was flowed again for 30 min to remove the unbound and loosely bound anti-human IgG.

Fig. 4.10 shows the resulting real-time curves for the described experiment. From the real-time measurements, it is possible to observe how during each protein dosing step the ΔEOT increases following a negative exponential trend. This feature is in good agreement with the kinetics explained in chapter II. Also, a slight decrease in the ΔEOT is observed during the PBS washing steps. This could be attributed to either removal of unbound or loosely bound molecules, or unbinding of the target molecule as due to the dissociation process resulting from the lower concentration of target analyte inside the pores (see chapter II, section 2.3.2.). In all the experiments, it is possible to observe how, in all cases, each protein infiltration step results in a further increase of the ΔEOT, showing curves with a characteristic stair-like shape. However, there are some differences between the samples. If we compare the same protein dosing step with different pore diameter, it can be observed how larger diameters lead to higher ΔEOT. And, if we compare samples with the same pore diameter, in all cases, SpA dosing leads to a similar ΔEOT between the two sample experiments, but this does not happen with the other two steps except for samples with Dp = 32 nm. With the other two diameters, the different concentrations of human IgG lead to two different ΔEOT, being this bigger for the larger concentration of human IgG. This effect is maintained during the amplification step with anti-human IgG.

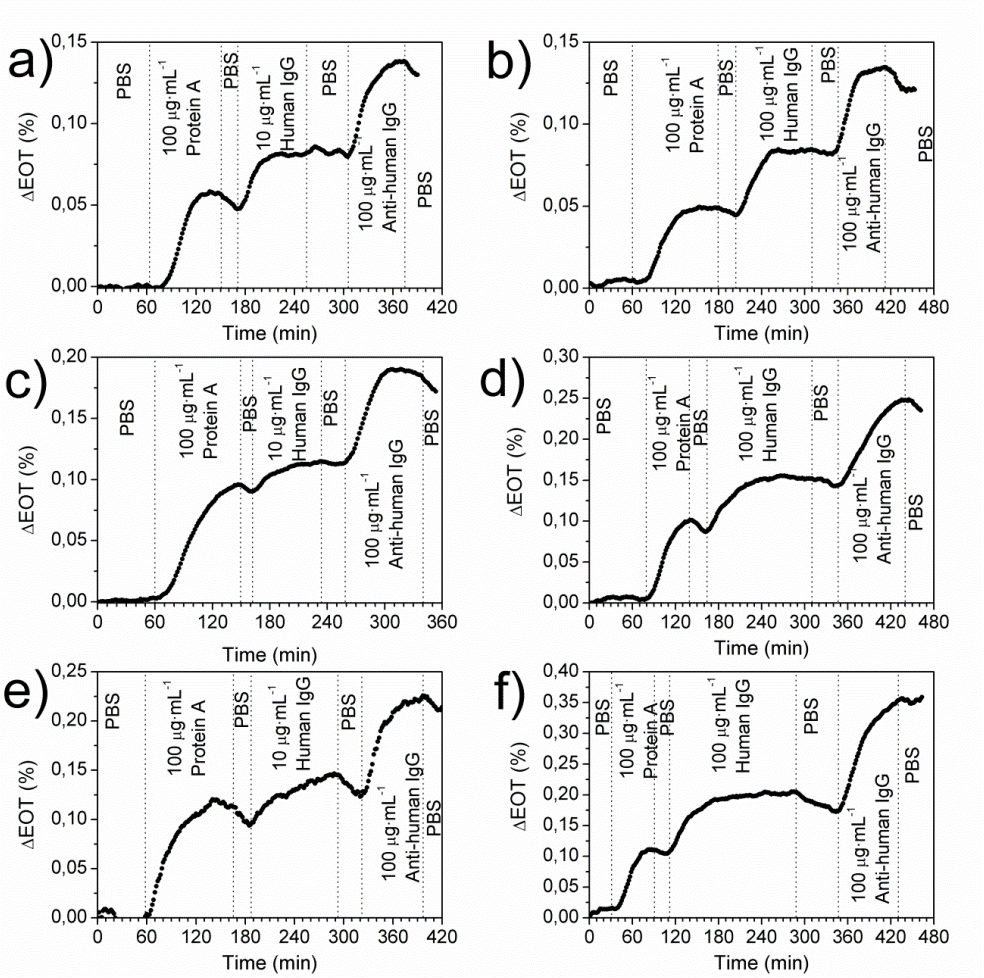

Figure 4.10. Real-time ΔEOT of protein dosing to NAA monolayers; a) and b) are pores of 32 nm, c) and d) pores of 50 nm, and e) and f) are pores of 73 nm. The left column (a), and c) and e)) shows the ΔEOT for 10 μg·mL-1 of human IgG and the right column (b), d) and f)) shows the ΔEOT for 100 μg·mL-1 of human IgG.

Fig. 4.11 resumes the results from fig. 4.10. We have classified the results in three curves designated as "steps" in fig. 4.11. Step I corresponds to the electrostatic attachment of SpA to the pore surface. Step II corresponds to human IgG capture by the SpA-functionalized pores. And step III corresponds to the ampli-

fication step with anti-human IgG. It can be observed how bigger pore diameters result in higher ΔEOT in all steps. It can also be observed how the amplification step effectively enhances the sensitivity of the system by a factor of 1.5-2. Regarding the sensitivity of the system, it can be observed how the difference in ΔEOT also increases with the pore diameter. It is interesting the fact that in pores with D_p = 32 nm there is no difference between the two distinct concentrations of human IgG but still the ΔEOT increases in step III. This feature contradicts the expected behavior of an affinity based biochemical reaction (see chapter II, section 2.3). Since the ΔEOT increased after dosing with anti-human IgG, we assume that human IgG is not denaturalized or damaged in the previous process. Therefore, we assume that the narrow pore diameter plays a major role on the biosensing kinetics but further investigation must be performed before elaborating any theory.

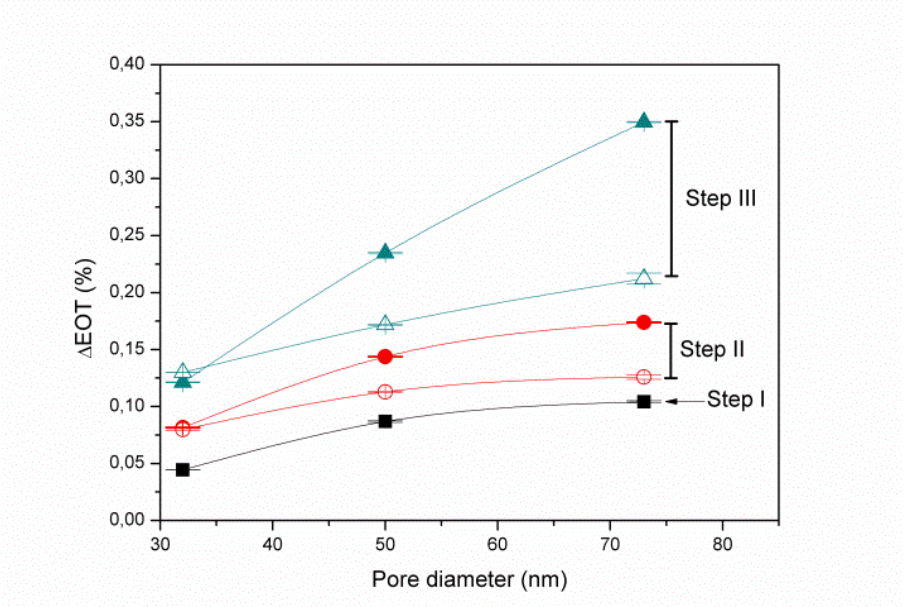

Figure 4.11. Resulting ΔEOT after each immobilization step for each D_p. Black squares represent SpA dosing, red circles represent human IgG dosing

and green triangles represent anti-human IgG dosing. Solid scatter represents for 100 µg·mL^{-1} and void for 10 µg·mL^{-1} of human IgG. Adapted from [173]

4.3.2. EFFECT OF FILM THICKNESS

The thickness of the NAA film (L) also has a direct effect on the EOT of the film as seen by eq. 4.1. In the wavelength spectrum, longer pore lengths result in a larger amount of oscillations which is crucial to perform the FFT. L also increases the EOT and allows to work further from the resonance at 0 nm of the FFT due to the mean shape of the spectral interferogram. However, these are just conclusions extracted from eq. 1. There are more effects of L with respect to the biosensing signal.

With the results from the previous section about pore diameter and eq. 4.1, it is clear that, maintaining the same D_p and D_{int}, thicker NAA layers would yield larger ΔEOT if this is measured in nm. This could be exploited when our peak detection algorithm is unable to detect slight changes in the position of the FFT peak. However, as seen in fig. 4.12, if the ΔEOT is expressed in percentage (%), the effect of L_p does not enhance ΔEOT. In fact, our calculations show how as the samples thickness increases, the effect of porosity towards de ΔEOT decreases. Nevertheless, fig. 4.12 confirms that the two key parameters for the optimization of NAA-based optical biosensors on the basis of ΔEOT are the D_{int} and D_p.

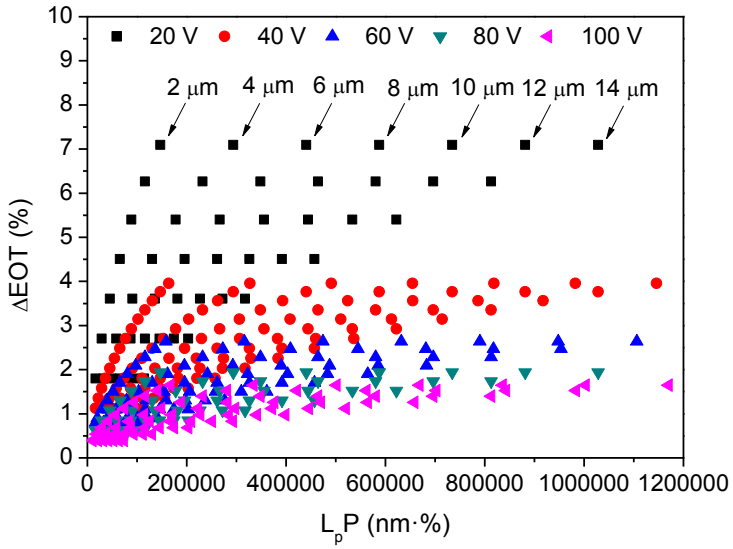

Figure 4.12. Comparative graph of the calculated ΔEOT (%) for samples anodized at 20, 40, 60, 80 and 100 V yielding interpore distances (D_{int}) of 50, 100, 150, 200 and 250 nm respectively.. For each sample type, different layer thicknesses (L_p) and pore diameters (Dp) have been considered. For ease of comparison, the structural parameters D_{int}, D_p and L_p have been synthesized in a single parameter (L_p·P) which concentrates all the information from the NAA sample by multiplying the pore length by the material's porosity.

Up to this point we have demonstrated how L_p does not affect the ΔEOT. However, L_p can still affect the performance of NAA optical biosensors by altering their kinetic behaviors. Essentially, pores can be modelled as a pipe. Therefore, any fluid flowing through the pores should be subjected to losses in their flow due to the friction with the pore walls. This can be calculated with the Darcy-Weisbach equation:

$$h_f = f\frac{L_p V^2}{2D_p g} \qquad (4.11)$$

Where h_f is the loss due to the friction with the pore walls, f is the friction coefficient with the pore walls, L_p is the thickness of the layer, V is the speed of the fluid, D_p is the pore diameter and g is gravity.

From eq. 4.11, it is possible to see that there is a direct relationship between the hydraulic losses in the pores and the thickness of the NAA sample. Therefore, layer thickness should influence the response speed of the optical biosensor, being longer for thicker samples. Recently, this has been confirmed experimentally by means of optical waveguide spectroscopy (OWS) [174].

4.3.3. SAMPLE COATING

Up to this point, we have determined the best geometry of nanoporous anodic alumina for optical biosensing. This structure must include wide nanopores with a small distance between them and with the thinnest depth possible for the analyte of interest. However, this kind of structure has a major inconvenience: large pores result in poor oscillation intensity [172].

From the practical point of view, the oscillation intensity is crucial. Larger oscillation intensities result in better distinction of the interference pattern and allow appropriate application of biosensing signal detection algorithms such as the FFT algorithm. In fact, as-produced NAA films themselves show insufficient interferometric intensity for RIfS, resembling noise to the newbie in NAA-based biosensing. This issue could be overcome by correcting the signal with 0/100% reflection references from calibrated master samples. Nevertheless, for high porosity samples this correction may be insufficient. In order to elucidate a possible solution, it is necessary to understand the factors related with the oscillation intensity. Eq. 4.12 shows the theoretical model of a Fabry-Pérot cavity.

$$R_{(\lambda)} = (\rho_a^2 + \rho_b^2) + 2\rho_a\rho_b \cos(2\delta_{(\lambda)}) \quad (4.12)$$

Where R is the reflectance at wavelength λ, ρ_a and ρ_b are the Fresnel coefficients at interface a (i.e. NAA-medium interface, see fig. 4.1) and b (i.e. NAA-Al interface, see fig. 4.1) respectively, and δ is the phase shift at wavelength λ. This phase shift is dependent on the EOT of the NAA film and is governed by the following relationship:

$$\delta_{(\lambda)} = \frac{2\pi n_{eff} L}{\lambda} = \frac{\pi}{\lambda} EOT \quad (4.13)$$

Where neff is the refractive index of the NAA layer, λ is the wavelength and L is the thickness of the NAA layer.

As it can be deduced from eq. 4.12, the Fresnel coefficients play a major role in both the amplitude of the oscillation and the overall shape of the reflectivity spectrum. These coefficients can be expressed as follows:

$$\rho_a = \frac{n_{med} - n_{eff}}{n_{med} + n_{eff}} \quad (4.14)$$

$$\rho_b = \frac{n_{eff} - n_{Al}}{n_{eff} + n_{Al}} \quad (4.15)$$

Where n_{med} is the refractive index of the media filling the pores (typically air, n_{air} = 1, or PBS, $n_{PBS} \approx 1.33$), n_{eff} is the effective refractive index of the NAA thin film, and n_{Al} is the refractive index of the remaining bulk aluminum. Since the experimental refractive index of NAA ranges between 1.6 and 1.1 (see fig. 3.24), the resulting oscillation amplitude is specially small for high porosity samples where the refractive index contrast ($\Delta n_{(a)}$) at interface a is reduced to a mere $\Delta n_{(a)} = 0.1$.

A possible solution would be to add another extremely thin layer (10-30 nm) on top of the NAA structure in order to increase $\Delta n_{(a)}$ without introducing a sec-

ondary interferometric pattern. By doing so, we are able to substitute the n_{med} in eq. 4.14 by the refractive index of the coating ($n_{coating}$). Among the available materials, metals such as gold are one of the best options. Despite their apparent small refractive index (real component of the refractive index), they exhibit high reflectivity with very thin layers of just a few nanometers due to their large imaginary component. Gold is an especially interesting material since it can be easily deposited through either evaporation or sputtering techniques and has a well-known surface chemistry which enables functionalization of the gold layer using thiolated compounds [175].

In order to study the effect of a gold overlayer on top of the NAA thin films, four samples using the two-step anodization procedure in 0.3 M oxalic acid solution at 40 V and 5 ºC to obtain a thickness of 1.62 µm were prepared. Then, the pores were widened in 5 % wt. H3PO4 for times of t_{pw1} = 0 min, t_{pw2} = 6 min, t_{pw3} = 12 min and t_{pw4} = 18 min yielding porosities of 14.3 %, 23.1 %, 44.6 % and 71.2 % respectively. The reflectance spectrum of these samples was acquired without gold, with 10 nm and with 20 nm of gold to see the effect of this layer on the interferogram. Fig. 4.13 resumes the results.

From these experiments we were able to see how even just 10 nm of gold were sufficient to dramatically increase the intensity of the Fabry-Pérot oscillations in all the studied porosities. This is in good agreement with equations 4.12 and 4.14. Further increase of the gold layer results in a lower maximum reflection in the UV-Vis region due to the strong absorption of gold in the visible region [177]. In the NIR region, two distinct behaviors:

- **For smaller porosities** (i.e. 14.3 and 23.1 %) increasing the thickness of the gold layer to 20 nm reduces the amplitude of the Fabry-Pérot oscillations and results in asymmetric fringes.

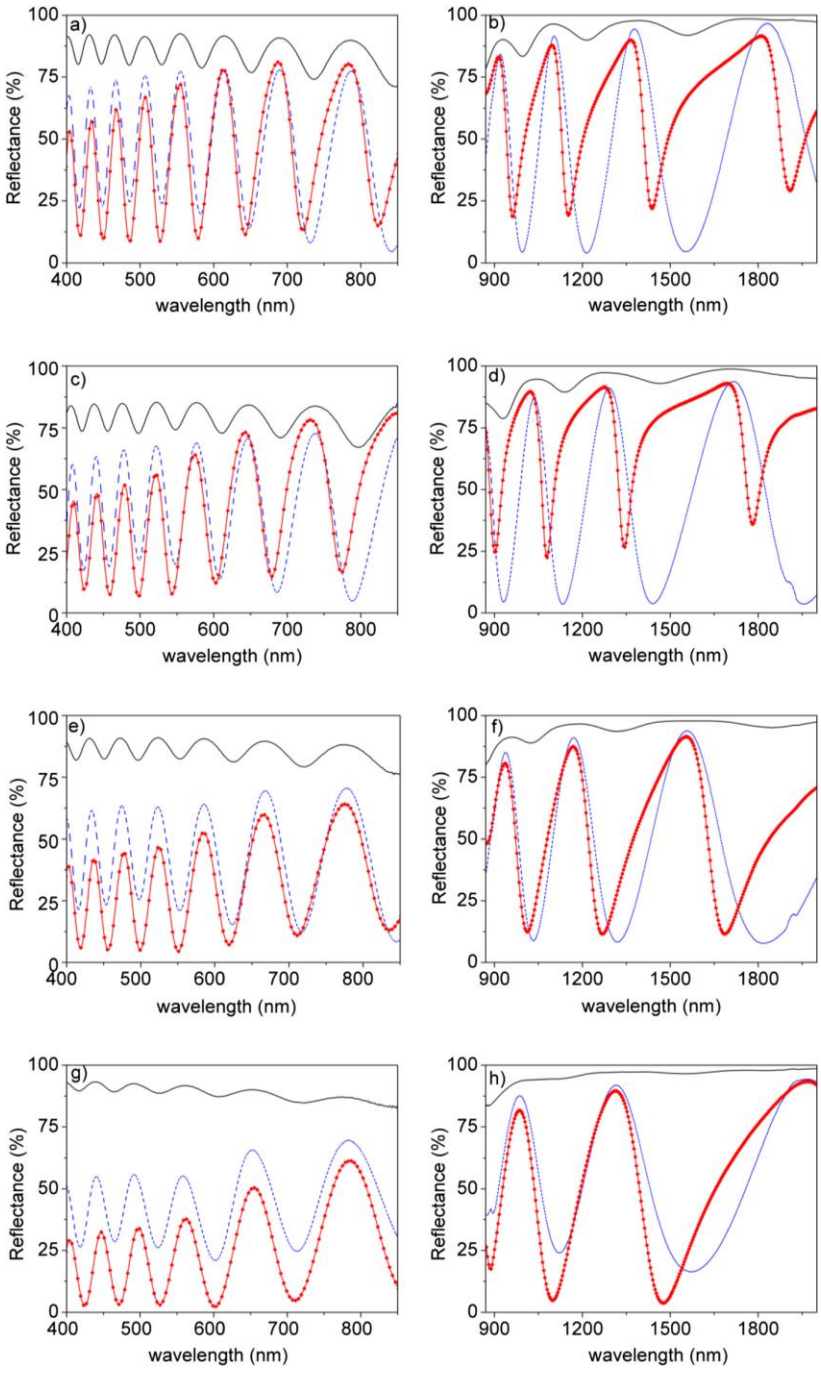

Figure 4.13. Reflectance spectra of samples with different t_{pw} before and after sputtering 10 and 20 nm of gold. Solid black lines represents the NAA samples without gold, dashed blue lines represent the resulting reflectance spectra

after sputtering 10 nm of gold and dotted red lines represent the resulting reflectance spectra after sputtering 20 nm of gold. The graphs on the left show the reflectance spectrum in the UV-Vis region while the graphs on the right represent the NIR region of the spectrum. (a,b) P = 14.3 %, (c,d) P = 23.1 %, (e,f) P = 44.6 % and (g,h) P = 71.2 %. Adapted from [176]

- **For higher porosities** (i.e. 44.6 and 71.2 %) increasing the thickness of the gold layer to 20 nm increases the amplitude of the Fabry-Pérot oscillations without resulting in such asymmetric fringes.

In order to explain all the different behaviors resulting from gold sputtering on top of NAA samples, we developed the model depicted in fig. 4.14 in which we took into account the thickness and porosity of the gold layer and the possibility of gold entering inside the pores.

The least squares fit of the model was able to predict the asymmetry of the NIR fringes by adjusting the thickness of the gold layer and its porosity. Besides, the reduction in the maximum reflection in the UV-Vis could be explained by the small fraction of gold deposited inside the pores during the sputtering process. However, the experimental data still show a higher reduction in the maximum reflection. This could be attributed to other sources of loss not taken into account in our model such as scattering or plasmonic effects. Table 4.1 resumes the results.

The amount of gold deposited inside the pores that was calculated using our model corresponds to 0.1 % for as produced samples while it increases to 1.2 % in samples with pores widened for t_{pw} = 18 min. This is in good agreement with the porosity of the samples, since larger pores allow better penetration of gold inside the porous structure. Similarly, the gold porosity was 55.3 and 59.5 % for samples with t_{pw} = 0 min and t_{pw} = 18 min respectively. This is also consistent with the porosity of the NAA samples.

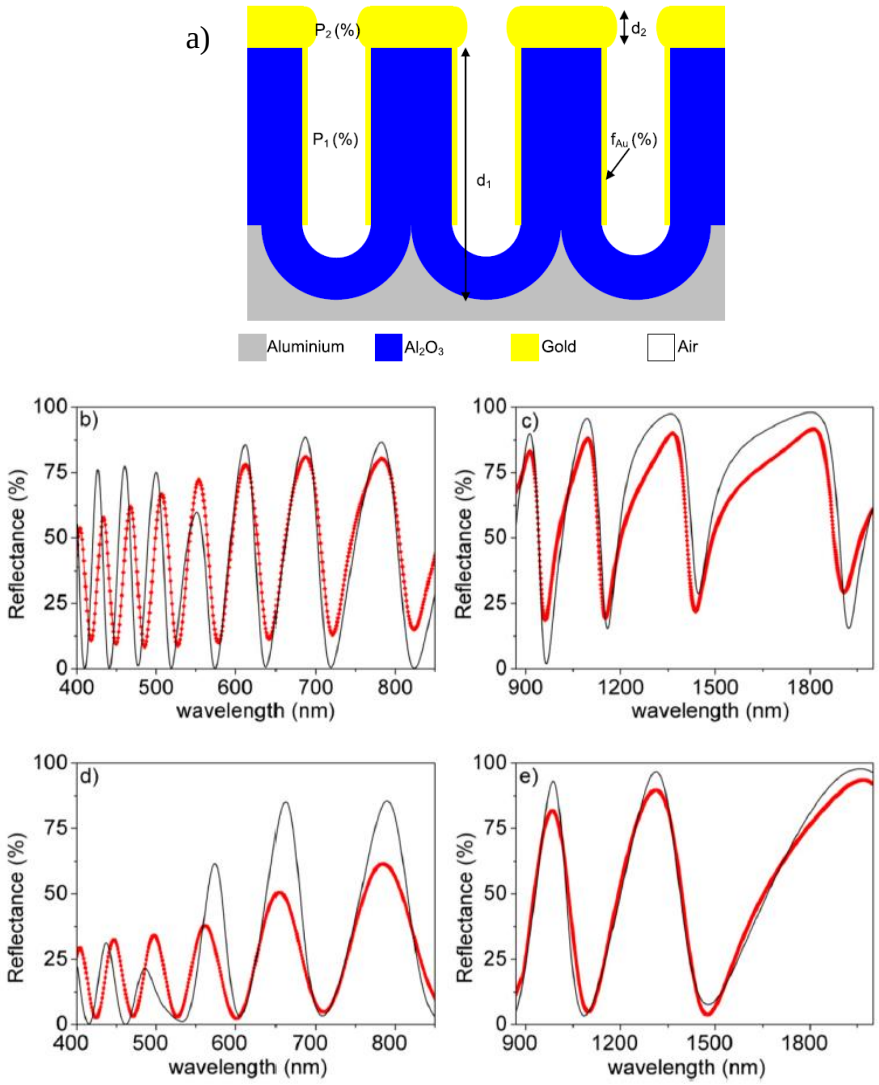

Figure 4.14. Model for gold-coated NAA samples and comparison of the measured and the best least-squares fitting simulated reflectance spectra. (a) Schematic drawing of the proposed theoretical model for gold-coated NAA samples. Red lines represent experimentally measured reflectance spectra. Black lines represent best least-square fit corresponding to simulation. Plots on the left correspond to the UV-Vis spectral region, while plots on the right correspond to

the NIR spectral region. (b, c) t_{pw} = 0 min and (d, e) t_{pw} = 18 min. adapted from [176]

Table 4.1. Results from the optical characterization of the samples with t_{pw} = 0 min and t_{pw} = 18 min after the deposition of 20 nm of gold. Adapted from [176]

t_{pw} (min)	NAA porosity, P_1(%)	Fraction of gold, f_{Au}(%)	NAA thickness, d_1(nm)	Gold porosity, P_2(%)	Gold thickness, d_2(nm)
0	6.8	0.1	1580	55.3	30
18	69.3	1.2	1580	59.5	25

Thanks to this data, we have assessed the effect of coating with a thin layer of gold on top of NAA samples and demonstrated its ability to overcome the reduction of fringe intensity due to the small refractive index contrast at the NAA/air interface.

4.4. SUMMARY

All the work presented in this chapter has resulted in better knowledge of the effect of the key structural parameters of NAA on the optical detection of analytes.

We have demonstrated how smaller interpore distances lead to much more refractive index-sensitive films due to the higher pore density. However, this feature greatly limits the possible application as it results in a smaller range of pores. Therefore, interpore distance should be carefully chosen in order to ensure sufficient volume for the target analyte.

Porosity is also a crucial parameter since larger pores lead to higher ΔEOT. We have demonstrated this issue both theoretically and experimentally. However, higher porosities also result in poor oscillation intensity which could almost result indistinguishable from the overall shape of the reflectance spectrum. Therefore, porosity should be aimed to be the highest value possible which still is able to be discerned in the reflectance spectrum.

Film thickness is also important. Depending on its thickness, different RIfS signal detection algorithms may be applied being direct fringe monitorization most suitable for the thinnest films (<1 μm) and FFT for the thickest samples (>2 μm). Also, thicker samples are less sensitive to porosity when measuring ΔEOT, but still the highest porosity samples show the greatest shifts. Apart from that, pore length has been experimentally and theoretically related with longer biosensing signal stabilization times due to flow resistance.

Finally, deposition of a thin metal layer of around 20 nm (such as the gold coating we described in the previous section) can enhance the oscillation amplitude of the Fabry-Pérot interference. This allows to work with sample porosities that otherwise would not be appropriate for interferometric biosensing.

Therefore, with all stated in this chapter, we can conclude that the most appropriate structure for interferometric biosensing using NAA consist of samples with:

- **D_{int}:** an interpore distance of 50 or 100 nm (i.e. anodized at 20 or 40 V) depending on the target analyte. For small molecules such as biotin and glucose, samples anodized at 20 V would give better results. However, for protein detection 40 V would probably give better ΔEOT as most proteins have a diameter between 5-15 nm and pores resulting from anodization at 20 V would probably hinder the diffusion of these biomolecules.

- **P%:** porosity of 70-80 % in order to have the largest pore possible but still retaining its structural integrity.

- **L_p:** a film thickness as thin as possible since this would allow a faster stabilization of the biosensing signal, but still retaining enough oscillations for applying a FFT algorithm (2-5 μm).

- **Coating:** a sputtered or evaporated metal coating of around 20 nm when the application allows it. Gold coating is a good option since there exists plenty of literature about selective gold functionalization through thiol chemistry and would allow the development of complex samples with dual functionality.

Chapter IV

CHAPTER V

BIOSENSING WITH NANOPOROUS ANODIC ALUMINA BILAYERS

5.1. OPERATING PRINCIPLE OF RIFS IN DOUBLE LAYER INTERFEROMETERS

The main inconvenient of using monolayers in RIfS biosensing is that to track environmental noise, such as temperature fluctuations or solvent composition, it is necessary to use a secondary RIfS sensor working under the same conditions and at the same time throughout the experiment to be used as a reference channel. This typically requires setup duplication, engrossing the overall device size. Recently, it has been shown how, with adequate data processing, two consecutive layers of porous material with distinct structure can work as working and reference channels.

5.1.1. THEORY

Structure

Double layer interferometers consist of two consecutive layers, L_1 and L_2, with their respective refractive indexes n_1 and n_2, resulting in a device with a total thickness of L_3. As depicted in fig 5.1, this structure gives rise to three distinct interfaces, namely a, b and c, where light reflection will occur. As a result, three different light beams appear with different phase shifts, being θ_1 for the light reflected at interface b, and θ_2 (with respect to the reflection at interface b) or θ_3 (with respect to the reflection at interface a) for light reflected at interface c.

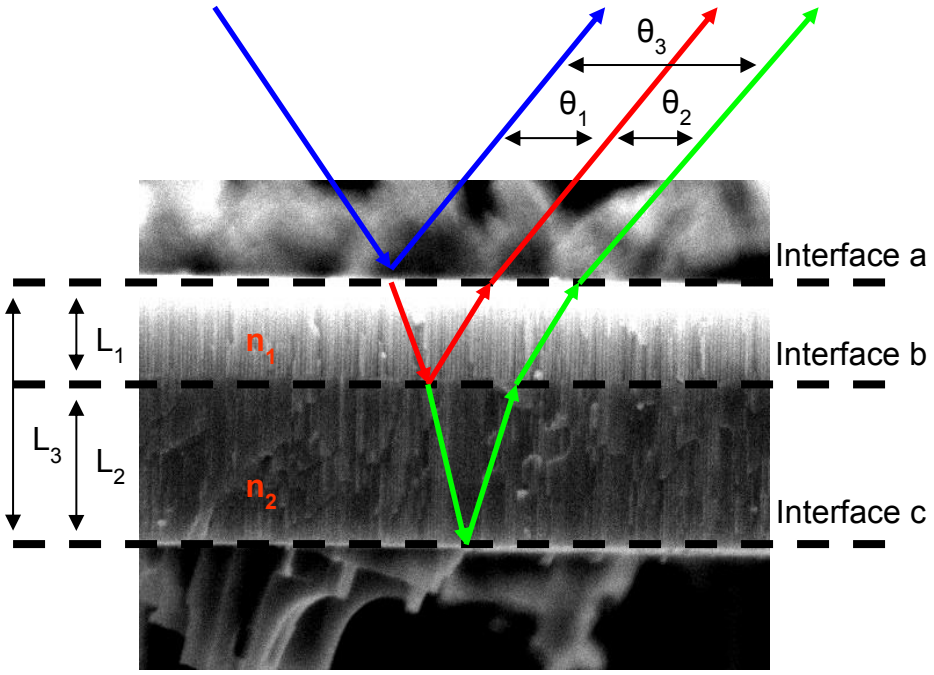

Figure 5.1. SEM of a NAA double layer consisting. Blue arrows represent light reflection at interface a, red arrows represent the reflection at interface b and green arrows represent the reflection at interface c.

Spectrum

As explained in chapter IV, when thin films are exposed to white light illumination, it results in a reflectance spectrum consisting of a series of sinus-like oscillations (see grey and dotted lines in fig. 5.2). However, double layers work slightly different. Since there are two layers, two sinus-like oscillatory patterns arise from the optical structure. The outcome is a complex interferogram (see black line in fig. 5.2) resulting from the sum of the oscillations of the two layers present in the structure.

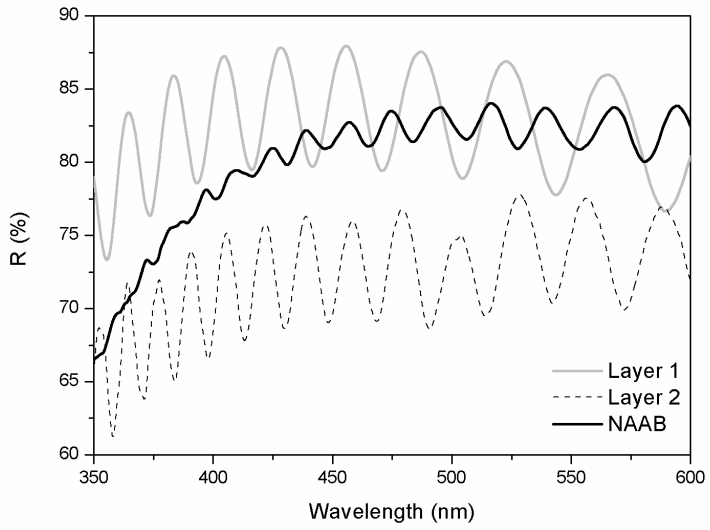

Figure 5.2. Reflectance spectra of two single nanoporous alumina layers and a nanoporous anodic alumina bilayer. Layer 1 and Layer 2 corresponds to a 1.9-µm-thick NAA sample of 41 % porosity and a 4.7-µm-thick NAA sample of 9 % porosity respectively. The NAAB corresponds to a bilayer with layer 1 on top of layer 2. Adapted from [178].

The complex reflectance spectrum of double layers can be explained by the following equation [179]:

$$R_{(\lambda)} = (\rho_a^2 + \rho_b^2 + \rho_c^2) + 2\rho_a\rho_b \cos\left(2\delta_{1\,(\lambda)}\right) + 2\rho_b\rho_c \cos\left(2\delta_{2\,(\lambda)}\right) + 2\rho_a\rho_c \cos\left[2\left(\delta_{1\,(\lambda)} + \delta_{2\,(\lambda)}\right)\right] \quad (5.1)$$

Where δi represents the phase relationship of layer i:

$$\delta_{i(\lambda)} = \frac{2\pi n_i L_i}{\lambda} \quad (5.2)$$

Where n_i represents the refractive index of layer i with thickness L_i. Terms ρ_a, ρ_b, and ρ_c indicate the index contrast at the interfaces (see fig. 5.1):

$$\rho_a = \frac{n_{med}-n_1}{n_{med}+n_1};\ \rho_b = \frac{n_1-n_2}{n_1+n_2};\ \rho_c = \frac{n_2-n_{Al}}{n_2+n_{Al}} \tag{5.3}$$

Where n_{med}, n_1, n_2, and n_{subs} refer to the refractive index of the surrounding medium, layer 1, layer 2 and the substrate respectively.

As it can be observed from eq. 5.1, the mathematical expression of the interference pattern arising from double layer interferometers is much more complex than that of monolayers (see chapter IV, eq.4.12). The resulting interferometric oscillations of double layers consists of the sum of three cosine functions which can be related to the oscillatory pattern of L_1, L_2 and the oscillatory pattern of the combination of both layers which for practical use we have named as L_3 (see fig. 5.1).

5.1.2. BIOSENSING SIGNAL

Given the complexity of the oscillatory reflectance spectrum of double layer interferometers, direct fringe monitorization and mode vs. position algorithms should be avoided to obtain the biosensing signal. While they would certainly work to see if the biochemical interaction takes place, and therefore, would work for biosensing in double layers, they are unable to perform self-correction for environmental fluctuations. This is due to the fact that these two methods are unable to distinguish the signal of the working channel from that of the reference. However, the FFT algorithm is able to distinguish between the different layers and provides the necessary information for self-correction.

FFT algorithm

As explained in the previous chapter, performing a FFT on a reflectance spectrum of oscillatory nature can convert the multiple oscillations into a single peak whose position is the EOT of the layer and its amplitude is related with the refractive indexes at the two interfaces of the layer. Comparing the mathematical expressions of both monolayers (see chapter IV, eq. 4.12) and bilayers (eq. 5.1) it is possible to elucidate the number of peaks that will result from the FFT of the reflectance spectrum. Therefore, double layers would result in three FFT peaks as its mathematical expression is composed of three cosine functions: one for the working channel (L_1), one for the reference channel (L_2) and one for the combination of both (L_3) [179].

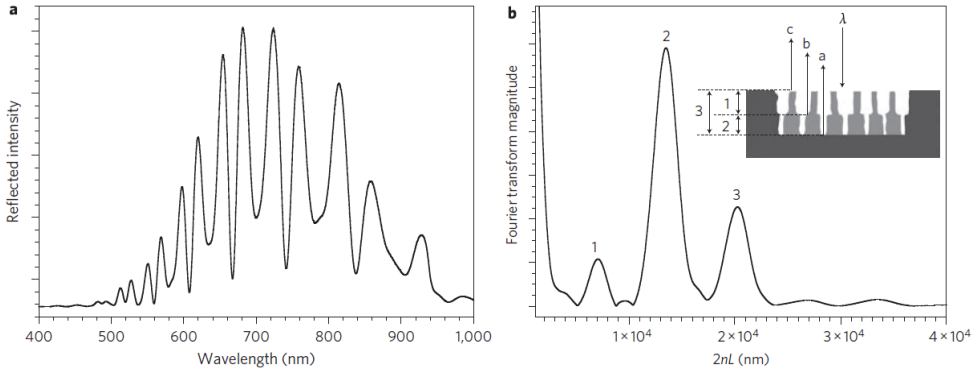

Figure 5.3. a) reflectivity spectrum of a pSi double layer interferometer without correction for instrumental spectral response, b) corresponding Fourier transform of the pSi bilayer. The inset in b) shows schematically the relationship between the FFT peaks and the porous layers of the structure. Adapted from [59].

Also, these FFT peaks will show different intensities depending on the refractive index contrast at both interfaces of the layer giving rise to the FFT peak in question. These intensities can be represented by the following mathematical expression:

$$A_1 = k\rho_a\rho_b;\ A_2 = k\rho_b\rho_c;\ A_3 = k\rho_a\rho_c \quad (5.4)$$

Where A_i is the intensity of the FFT peak i, ρ_i is the Fresnel coefficient at interface i calculated as described in eq. 5.3, and k is a proportionality constant accounting for the experimental conditions.

Detection strategies for porous double layers

Thanks to the FFT algorithm, it is possible to extract information from the working and reference channel of the biosensor. Moreover, the FFT of the reflectance spectrum gives us information about both the EOT of the layers and also about the refractive index at the interfaces of both layers thanks to the information encoded by the intensity of the FFT peak. Both sets of data may be used to track biochemical interaction effects.

Detection of analytes through EOT measurements

The incorporation of the analyte on the top (working) layer L_1 can be performed by computing the difference between the EOT of the top layer and that of the bottom layer (i.e. reference layer) L_2.

$$\Delta EOT_{1-2} = EOT_1 - EOT_2 \quad (5.5)$$

Similarly, the third peak present in the FFT that accounts for the effects of the two layers (i.e. the sum of the EOT of the working and reference layers) can be used to acquire the biosensing signal.

$$\Delta EOT_{3-2} = EOT_3 - EOT_2 \quad (5.6)$$

However, since normally these two layers have different porosities and thicknesses a correction constant γ is introduced to account for such issues [179]. Therefore, eq. 5.5 and 5.6 should be replaced by:

$$\Delta EOT_{1-2} = EOT_1 - \gamma EOT_2 \quad (5.7)$$

and

$$\Delta EOT_{3-2} = EOT_3 - \gamma EOT_2 \quad (5.8)$$

This correction factor assumes that the refractive index of each layer is proportional to its fractional composition. Then, γ indicates the relationship between the optical responses of one of the layers with respect to the other. It can be determined experimentally as follows:

$$\gamma = \frac{EOT_{1(air)} - EOT_{1(buffer)}}{EOT_{2(air)} - EOT_{2(buffer)}} \quad (5.9)$$

For eq. 5.7 and

$$\gamma = \frac{EOT_{3(air)} - EOT_{3(buffer)}}{EOT_{2(air)} - EOT_{2(buffer)}} \quad (5.10)$$

For eq. 5.8. Where $EOT_{i(air)}$ is the EOT of the layer i in air and $EOT_{i(buffer)}$ is the EOT of the layer i in the buffer solution used for the biochemical interaction.

With this data processing and a well-designed double layer interferometer it is possible to achieve discrimination of proteins from small molecules typically present in biological fluids such as glucose.

Chapter V

Detection of analytes through FFT's peak intensity

When the analyte enters the working layer, this layer experiences a change on its refractive index. This change, in turn, results in an altered refractive index contrast at the interfaces of the layer. According to eq. 5.3 and 5.4, this change in refractive index can be monitored by measuring the intensity of the FFT peak. Since the capture of the analyte at layer L_1 results in a change in its refractive index n_1, this binding will result also in a shift in the peak intensity of layer L_2 (see eq. 5.3 and 5.4). This is due to the fact that both layers share a common interface. In order to correct this signal with the data present in the reference layer, it is necessary to perform the following calculation [179]:

$$\frac{A_1}{A_1} = \frac{k\rho_a\rho_b}{k\rho_b\rho_c} = \frac{\rho_a}{\rho_c} \tag{5.11}$$

Eq. 5.11 eliminates the effect of small molecules and solvent allowing a selective response to the analyte. This equation assumes that the FFT peak corresponding to layer L_1 is visible. If this is not the case, the response can be isolated from the peak intensity of layer L_3.

5.2. SELF-REFERENCING IN DOUBLE LAYER INTERFEROMETERS

5.2.1. DUAL FUNCTIONALIZATION

One possible way to be able to self-reference the layers is by applying a selective functionalization approach. This approach consists in applying different functional groups on each layer so that the biological receptor is located in just one of them (i.e. the working channel). The reference channel may be left as produced or functionalized to avoid biofouling.

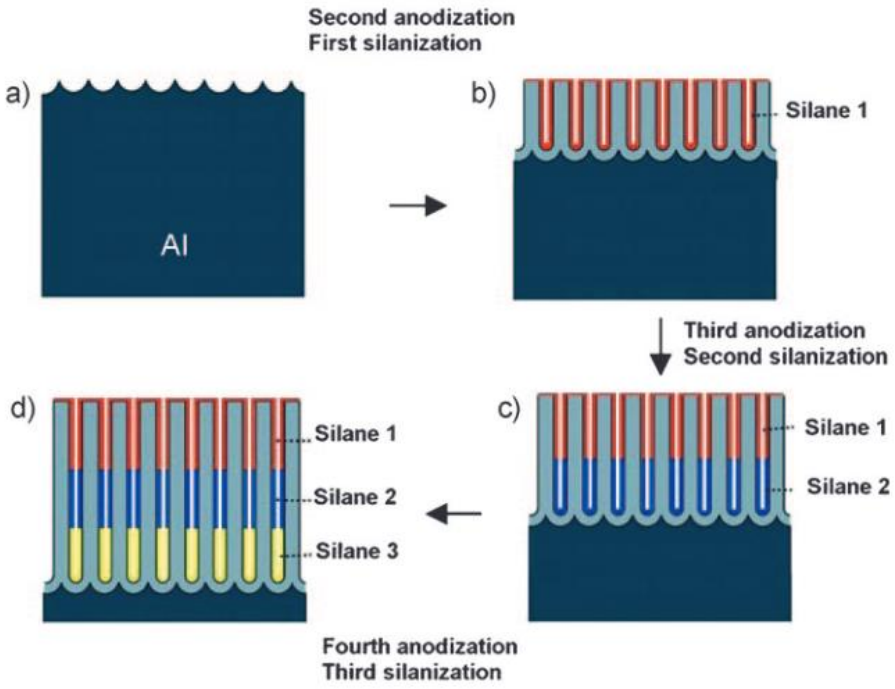

Figure 5.4. Fabrication scheme of NAA layered with 3 different silanes to display multiple surface functionalities. Adapted from [180]

This option is a good for NAA since it has been demonstrated that the anodization conditions do not destroy the silanization of the pore surface [180]. This allows the fabrication of NAA films with multiple layer functionalities by applying subsequent anodization/silanization cycles as depicted in fig. 5.4.

5.2.2. SIZE EXCLUSION

Another possibility for the self-referencing of porous double layer interferometers is by accurately designing the pore diameters of the working and reference films. This can be performed if the size of the target analyte is known. If

that is the case, the bottom layer can be designed with pores small enough to prohibit the entrance of the analyte while still allowing the entrance of solvent molecules [179].

This approach is particularly interesting when the target analyte is a protein. Most proteins have a size in the 5-20 nm range. With electrochemically etched pSi and also with NAA it is possible to perform double layers capable of size-selective exclusion by accurately tuning the etching conditions []. This size exclusion allows the elimination of the effect of variations in solvent composition which may induce false results during the monitorization of the biochemical reaction. This is of great interest for point-of-care devices as biological fluid samples, such as blood, may have enormous differences in solvent composition from patient to patient. The size exclusion double layer would be capable of reducing the error rate of these devices by tracking the effect of small molecules, such as glucose or sucrose (as explained in section 5.1.2), and correcting their effect in the measurement.

5.3. DESIGN OF NANOPOROUS ANODIC ALUMINA DOUBLE LAYERS

In order to be able to develop double layer interferometers for biosensing applications based on NAA, it is necessary to optimize the structure. In this section, we are going to discuss the parameters involved in the design of nanoporous anodic alumina bilayers (NAAB) to obtain devices as the one depicted in fig. 5.5.

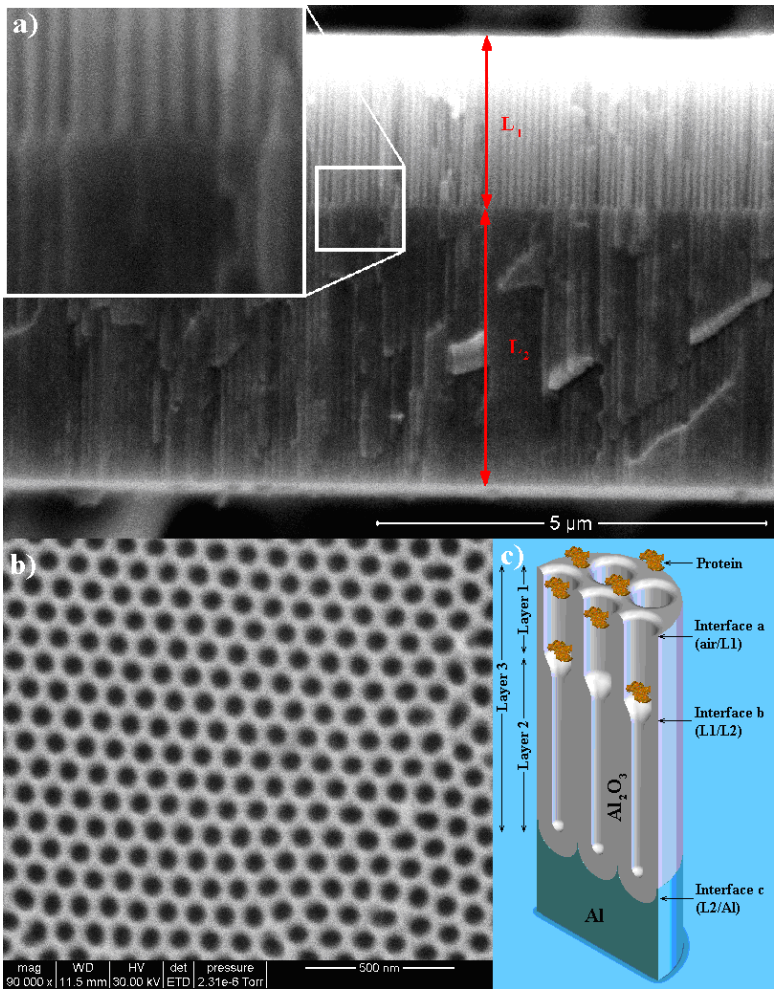

Figure 5.5 Scanning electron microscope (SEM) micrographs of a) cross-sectional view of the NAAB. The inset shows a magnification of the interface between the two layers displaying a funnel structure b) top view of the NAAB. Top layer consists in a self-ordered hexagonal array of pores with a diameter of 68 nm and a thickness of 1.9 µm, while bottom layer present a diameter of 33 nm and a thickness of 4.7 µm. c) schematic representation of the nanoporous anodic alumina bilayer. The interfaces a, b and c represent the zone where the reflections occur resulting in 3 interfering light beams. Adapted from [178].

5.3.1. FABRICATION PROCEDURE

Given the two strategies previously discussed for the self-referencing of double layer interferometers, we think that size exclusion is more interesting. The reason for this special interest is the high sensitivity of nanoporous materials to the refractive index of the filling medium. Therefore, being able to correct for drifts related with solvent composition is of great interest.

To do so, NAA must be performed in a three-step anodization fashion [179]:

1. **1st step anodization:** during this step, we anodize the Al foils for 20 h at 5 ºC at the desired potential and electrolyte (typically 40 V and 0.3M $H_2C_2O_4$). After the anodization, the resulting NAA layer is selectively dissolved and the remaining Al presents an ordered array of concavities which serve as pore nucleating sites for subsequent anodizations.
2. **2nd step anodization:** in this step we grow the first layer of the NAA double layer interferometer which will serve as the working channel. This anodization is conducted under the same conditions as the 1st step to ensure self-ordering of pores. Once the NAA layer has reached the desired thickness, we adjust the pore diameter in 5 % wt. H_3PO_4 in order to obtain pores large enough to accommodate the biomolecule of interest.
3. **3rd step anodization:** this is the final anodization step. In this step we grow the second layer of the double layer interferometer which will serve as the reference channel. This anodization is performed under the same conditions as the 1st and 2nd anodization steps in order to ensure a funnel-like architecture.

5.3.2. LAYER CHARACTERISTICS

Above we have described the protocol for the fabrication of double layer optical interferometers based on NAA. In this section we are going to discuss the desired characteristics of the working and reference layers of the NAAB.

Top (sensing) layer

This layer serves as the working channel of the double layer interferometer. Since our design is based on size exclusion, this layer must be placed on top of the structure and in direct contact with the analyte solution to ensure adequate infiltration of the target biomolecules.

Pore diameter

Given the size exclusion design, this layer requires a higher porosity than the reference layer. However, from the results presented in chapter IV, its sensitivity is directly related with the porosity. Therefore, for maximum sensitivity it is necessary to widen the pores close to its mechanic stability limit. For NAA fabricated in 0.3M $H_2C_2O_4$ at 40 V and 5 ºC this is achieved with pore widening by wet chemical etching in 5 % wt. H_3PO_4 for 15-20 min.

Layer thickness

Since the only available method for the characterization of NAAB is the FFT algorithm, the layer thickness must be kept within a range where it is discernible from the frequency depicted at 0 nm (signal coming from the mean reflectance

shape). But also, it must be taken into account that thick layers result in longer stabilization times. For these reasons, our NAAB have been designed with 2 μm-thick layers.

Bottom (reference) layer

This layer serves as a reference for the correction of the signal of the working layer. Due to the size exclusion principle of action this layer is placed right beneath of the working layer.

Pore diameter

The pore diameter of this layer must be adjusted so as to permit the entrance of the solvent and the small molecules that may be encountered inside (such as glucose) while avoiding the entrance of the target analyte. Since mostof the analytes of interest for biosensor development are proteins, this would mean that, ideally, pores should be below 10 nm in diameter. However, to obtain pores with NAA is rather challenging.

Samples fabricated in 0.3M H_2SO_4 at 20 V and 5 ºC present the smallest self-ordered pores and their mean diameter is around 15 nm. This might be an issue for the development of NAAB biosensors. Nevertheless, it has been demonstrated that protein transport can be inhibited with pores much larger than twice their hydrodynamic radius. This fact allows us to perform working NAAB biosensors with the available pores in NAA fabricated under MA conditions.

Layer thickness

While for the working layer the film thickness had to be limited in order to avoid long stabilization times in the biosensing signal due to hindered diffusion of the proteins, this is not a limitation for the reference layer. The reason for this is that proteins are going to be already inhibited in this layer and only the solvent should enter inside the pores. Therefore, the limitation here is only related with the resolution in the frequency spectrum after the data processing using the FFT algorithm.

It must be noted that the peaks resulting from the FFT processing of the reflectance data are quite wide. This may result in peak overlapping if the ratio (L_1/L_2) between the working (L_1) and the reference (L_2) layers is not appropriately designed. In turn, this overlapping might interfere with the automatic peak detection algorithm resulting in an erratic biosensing signal.

In order to determine experimentally the best L_1/L_2 ratio for NAAB biosensors four NAAB with different L_1/L_2 ratios were fabricated, measured and a FFT was applied to the resulting reflectance spectra. The FFT plots can be observed in fig. 5.6a. Unlike the FFT plots of pSi double layers presented in fig. 5.3b which show three distinct peaks, NAAB just present two peaks. These peaks correspond to layers L_2 (reference) and L_3 (reference + working). The reason for the lack of the peak for layer L_1 is the low reflectivity of L_1. This results in a FFT intensity of the order of the FFT noisemaking impossible to discern L_1's peak. One possible way to overcome this issue and be able to discern L_1's peak in the FFT is by depositing a thin metal layer on top of the structure. This changes dramatically the Δn at the top interface and allows us to see the three peaks in all the studied NAABs (see fig.5.6b). From fig. 5.6a and 5.6b it is possible to see that the L_1/L_2 ratio must be maintained between 0.5 and 0.75 to avoid peak overlapping. Moreover, in fig. 5.6b it can be observed why layers

below 2 µm must be avoided, as L_1 peak of sample S1 overlaps with the frequency at 0. The structural characteristics of samples S1-4 are presented in table 5.1.

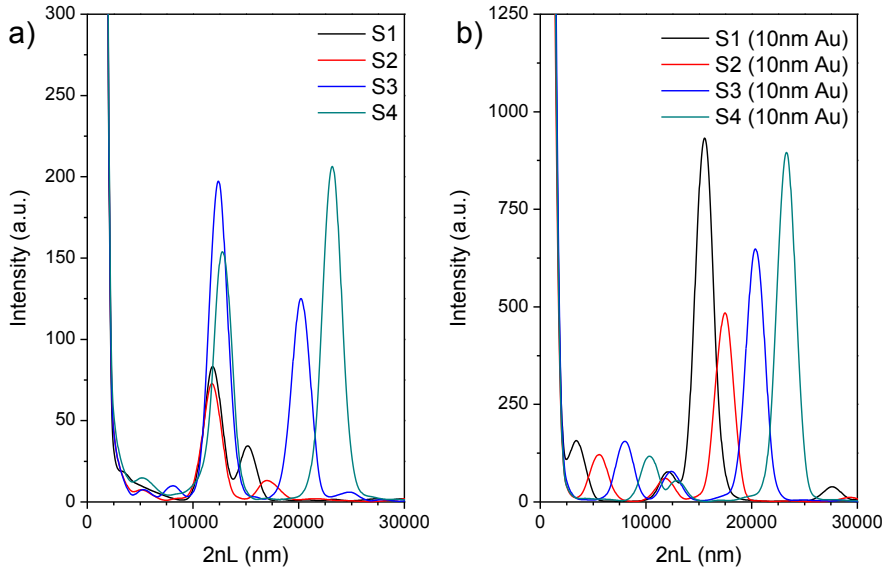

Figure 5.6. FFT plots of NAAB with different L1/L2 ratios for a) as produced NAAB, and b) NAAB after sputtering 10 nm of gold.

Table 5.1. Sample characteristics of the NAAB depicted in fig.5.8.

Sample name	L_1/L_2	Electrolyte	V_{an}(V)	L_1(µm)	t_{pw1}(min)	L_2(µm)	t_{pw2}(min)
S1	0.25	0.3 M $H_2C_2O_4$	40	1	20	4	0
S2	0.5			2			
S3	0.75			3			
S4	1			4			

Metal coating

As seen in fig. 5.6a, the reflectivity of as-produced NAABs is not sufficiently high to show the three distinct peaks expected in the frequency plot after performing a FFT on the acquired reflectance spectra. By depositing a thin metal of gold, this reflectivity could be enhanced (see fig.5.6b). In this section, the effect of this gold sputtering will be discussed.

In the previous sections, pore diameters and layer thicknesses of both the working and the reference layers have been optimized for biosensing. In order to analyze the effect of gold sputtering on top of the structure a NAAB with the optimized parameters was fabricated and measured, at the very same spot, before and after depositing 10 nm of gold. The fabrication conditions and the structural characteristics are described in table 5.2.

Table 5.2. Fabrication conditions and structural characteristics of as produced NAAB.

Step	Electrolyte	V_{an}(V)	t_{an}(h)	t_{pw}(min)	D_p(nm)	D_{int} (nm)	L_p(μm)
1	0.3 M H2C2O4	40	20	N.A.	N.A.	N.A.	N.A.
2			0.5	15	68±2	106±3	≈ 1.9
3			1	0	33±3	105±7	≈ 4.7

*N.A.: Not applicable

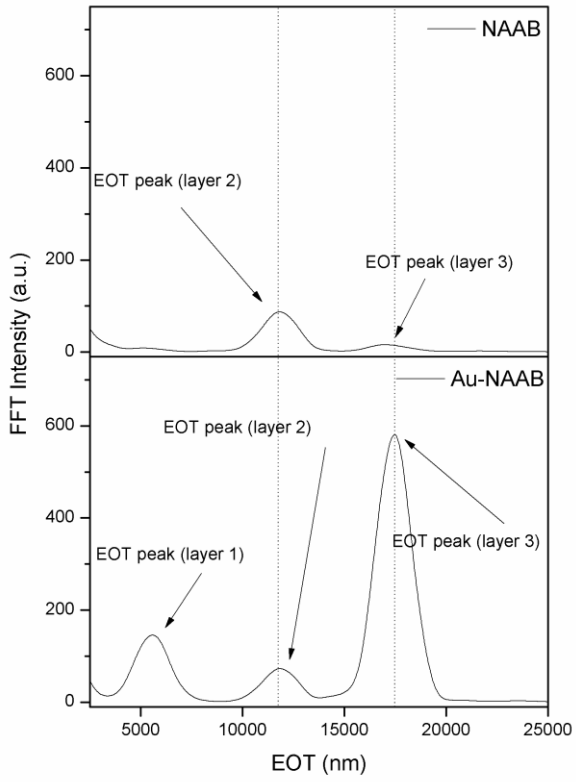

Figure 5.7. Comparison between the FFT plots of a NAAB and Au-NAAB with the same layer thicknesses. The deposition of the metal coating results in an enhancement of the FFT intensity of layer 3 peak and the appearance of the peak 1. Adapted from [178].

Fig. 5.7 shows a comparison between the as-produced NAAB and the NAAB after sputtering 10 nm of gold (Au-NAAB). For the NAAB (fig. 5.7a), the EOT measured for layer 2 and layer 3 are 11700 nm and 16700 nm, and exhibit peak intensities of 85 and 15 respectively. From the EOT data of the NAAB, it is possible to estimate that the EOT of layer 1 should be around 5000 nm. After the deposition of 10 nm of gold (fig. 5.7b), a dramatic enhancement of the FFT in-

tensity is observed for layer 3 and the peak from layer 1 becomes visible. In this case, the EOT measured are EOT_1 = 5856 nm, EOT_2 = 11700 nm and EOT_3 = 17600 nm. Peak 1 does not appear exactly in the expected position, but this is due to the fact that the total thickness of layer 1 has been modified by the gold deposition. Moreover, the EOT is the combination of the EOT of the gold layer and the EOT of the NAA layer. The sum of these factors could explain the difference between the measured EOT_1 in the Au-NAAB and the expected EOT_1 calculated from the EOT_2 and EOT_3 measured in NAAB. It must be noted how peak 2 is not affected by the sputtering of gold in either EOT or FFT intensity. This is so because the interfaces that affect the performance of layer 2 are interfaces b and c, which are inaccessible to the gold. As a result, peak 2 remains unaffected. On the other hand, peak 3 does present a shift in its EOT of ≈ 5 %. This shift can be attributed to the gold adlayer deposited at interface a. The most interesting feature of peak 3 after gold sputtering is the tremendous enhancement of its intensity, which is increased by a factor of 38.

5.4. SIZE EXCLUSION IN NAA BILAYERS

In order to check the size exclusion performance of NAABs during biosensing, two types of samples were manufactured following the fabrication conditions presented in table 5.2. One set consisted of as-produced NAA double layers (NAAB) and the second set was coated with 10 nm gold (Au-NAAB). To check the ability of NAAB and Au-NAAB to prohibit the entrance of proteins in the reference layer, an infiltration experiment with bovine serum albumin (BSA) was designed.

5.4.1. BSA INFILTRATION EXPERIMENT

BSA is a model protein commonly used in biosensing as a blocking agent to limit biofouling due to non-specific biomolecular binding to the sensing substrate. Its largest dimension is roughly 8 nm and at pH 7 is negatively charged [179]. Comparing the size of BSA (8 nm) with the pore diameter of the reference layer (30-35 nm), the pores supply sufficient volume for the accommodation of BSA. However, protein diffusion in nanoporous substrates can be significantly limited with pore diameters much larger than the hydrodynamic radius of the protein [181]. Therefore, no BSA should enter layer 2 even with the pore diameter of layer 2. Moreover, since BSA adsorption to the pore walls could occur due to electrostatic interactions [182], prior to the infiltration experiment, the NAA double layer structure was blocked with BSA [179]. If any BSA would enter the reference layer with the 30 nm pores, this BSA blocking would coat the surface of the reference layer further reducing the effective pore diameter to roughly 15 nm, limiting even more the diffusion of BSA into the reference layer.

Infiltration protocol

Infiltration of BSA was performed in a two-step fashion:

1. **Step 1:** NAABs and Au-NAABs were incubated with 1 $mgml^{-1}$ solution of BSA in PBS for 2 h at 5 °C. This procedure allows us to block the porous surface with BSA by electrostatic interaction and to the gold overlayer through thiol chemistry. Thanks to this step it is possible to eliminate artifacts in the measurements arising from other effects than the steric exclusion of BSA into the reference layer. Then, the NAABs and Au-NAABs were thoroughly rinsed with PBS to remove any free BSA that did not attach to the porous surface and

immediately after with DI water. Prior to measuring, the remaining solvent was carefully removed and was left to dry. Once the double layers were dried, their reflectance was measured using a Perkin Elmer λ950 spectrophotometer.

2. **Step 2:** subsequently, the NAABs and Au-NAABs were incubated with 1 $mgml^{-1}$ solution of BSA in PBS for 2 h at 5 °C. This step allows us to verify the size exclusion performance of the NAA double layers. Prior to reflectance measurements, the remaining solution was carefully removed to avoid the development of a thick protein layer on top of the structure. Then, the NAABs and Au-NAABs were left to dry. Once they were completely dried, their reflectance was measured at the same spot.

BSA infiltration results

Fig. 5.8 shows the resulting FFT of an Au-NAAB before the infiltration of BSA (grey line) and after the infiltration of BSA (black line). Note that the Au-NAAB depicted in fig. 5.8 is not the as-produced Au-NAAB, but the Au-NAAB after the 1^{st} step infiltration with BSA to block both the pore surface and the gold overlayer. As a general feature, the infiltration of BSA resulted in an overall decrease of the intensity in the whole FFT spectrum. This is a result from the BSA trapped in layer 1. The addition of BSA in layer 1 increases the overall refractive index of layer 1 and consequently diminishes the refractive index contrast in the double layer. Apart from that, the FFT peaks of layers 1 and 3 present an increase in their EOT, which is also a result from the BSA present in the working layer. On the other hand, the peak for layer 2 seems unaltered at naked eye, but a small shift of 19 nm can be observed. This small shift, compared to the shift from layer 1 (ΔEOT_1 = 708 nm) and layer 3 (ΔEOT_3 = 835 nm) is almost negligible and could be attributed to either an artifact of the FFT algorithm or to a small inhomogeneity in the sample.

The same structure without gold was also tested. The main difference is the lack of the peak for layer 1. Therefore, the size exclusion performance can only be checked by the FFT peak corresponding to layer 3. Also, the measured ΔEOT_3 is of just 84 nm. Comparing the results of the Au-NAAB with the NAAB, the Au-NAAB exhibits a ΔEOT an order of magnitude higher.

Apart from the EOT analysis, peak intensity can also be used for the detection of BSA (see section 5.1.2.2.2). To do so, either A_1/A_2 or A_3/A_2 ratios must be calculated in order to correct for the environmental drifts. Of these two ratios, the only one comparable in the two structures is the ratio A_3/A_2 due to the lack of peak 1 in the NAAB. For the NAAB, the shift in the amplitude ratio ($\Delta A_3/A_2$) displayed after the infiltration of BSA is of 0.02, while for the Au-NAAB, this $\Delta A_3/A_2$ is 19.83. It can be observed how a deposition of just 10 nm of gold increases dramatically the response of NAA-based double layer biosensors. All these results are summarized in table 5.3.

Table 5.3. Experimental results from the FFT analysis of the NAAB and the Au-NAAB before and after being infiltrated with BSA. Adapted from [178].

Sample	ΔEOT_1	ΔEOT_2	ΔEOT_3	A_1/A_2	A_3/A_2	A_1 (a.u.)	A_2 (a.u.)	A_3 (a.u.)
NAAB	N.A.	N.A.	N.A.	N.A.	1.27	N.A.	2787	3554
NAAB + BSA	N.A.	47	84	N.A.	1.29	N.A.	2776	3571
Au-NAAB	N.A.	N.A.	N.A.	2.25	12.87	2310	1026	13206
Au-NAAB + BSA	708	19	835	2.18	32.70	510	234	7652

*N.A.: Not applicable

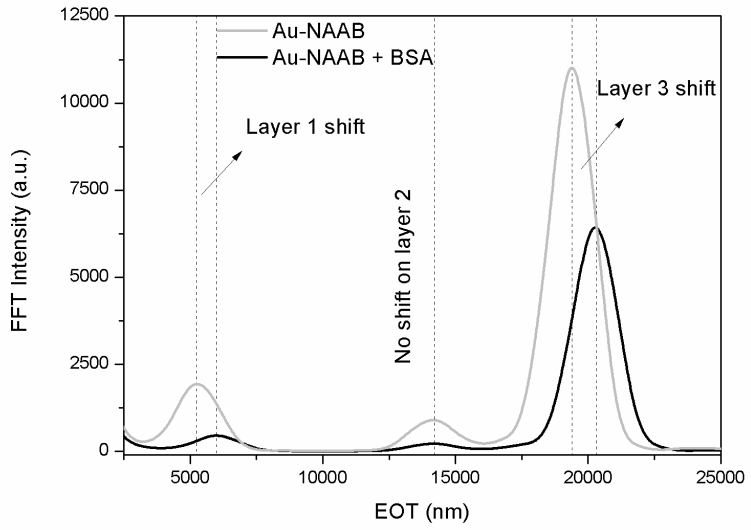

Fig. 5.8. FFT plot of the optical response of the Au-NAAB before and after the introduction of BSA protein. A decrease in the intensity of the FFT peak in all three layers is observed after the entrance of BSA protein the structure. The EOT only varies for layers 1 and 3 after the infiltration of BSA protein. Adapted from [178].

5.4. SUMMARY

In this chapter we have presented a novel optical structure for its use as a biosensor. This structure consists in a double layer interferometer in which the top layer acts as the working channel, while the bottom layer acts as a reference channel. This configuration allows self-correction of the signal for environmental drifts such as temperature or solvent composition.

To achieve self-correction, a size exclusion structural design has been presented in which BSA (a model analyte) was prohibited to the reference layer by means of steric hindrance.

This complex structure can be fabricated using a 3-step anodization procedure. The first anodization generates pore self-ordering, the second creates the working layer and allows fine tuning of its porosity through wet chemical etching in 5 % wt. H_3PO_4 and finally, the third anodization grows the reference layer that permits the self-correction of the biosensing signal. Since this double layer interferometer requires the application of the FFT algorithm explained in chapter IV, section 4.2.1, the layer thicknesses have to be adapted in order to fulfill the requirements of this data processing algorithm. From all the data presented in this chapter, this means that:

- **For the top layer (i.e. the working channel):** the layer thickness must be around 2 μm. Thicker films would result in longer infiltration times that would lead to longer biosensing experiments, and thinner films would result in overlapping of peak 1 with the peak at 0 nm in the FFT spectrum. Regarding the porosity, this should be kept to the highest value possible that maintains the straight pore structure. For samples fabricated in 0.3M $H_2C_2O_4$ at 40V and 5°C this requires an etching with 5 % wt. H_3PO_4 at 35 °C for 15-20 min.
- **For the bottom layer (i.e. the reference channel):** the layer thickness should provide sufficient spacing between the FFT peaks after the data processing to ensure no overlapping of the peaks. This will avoid errors during the peak picking step of the FFT algorithm. To achieve this spacing, the thickness ratio between the top and bottom layers (L_1/L_2) must be between 0.5 and 0.75 (i.e. $L_2 \approx 4$ μm). Regarding the porosity, in this case it should be kept to the minimum (i.e. as produced porosity). The optimal case would be the one that ensures a pore diameter smaller than

the size of the analyte, but pores up to 30-35 nm seem to work fine with NAAB.

Finally, it has been demonstrated how a deposition of just 10 nm of gold is able to improve the refractive index contrast of the double layer structure. This signal enhancement allows the detection of the FFT peak for the top layer 1 which would otherwise be invisible due to the small refractive index contrast. Moreover, this 10 nm of gold also result in a much more sensitive detection of BSA in both EOT and FFT intensity measurements.

Chapter V

CHAPTER VI

SENSING WITH NANOPOROUS ANODIC ALUMINA RUGATE FILTERS

6.1. INTRODUCTION

6.1.1. WHAT IS A PHOTONIC CRYSTAL?

Photonic crystals (PCs)are periodic dielectric structures that are able to modulate light in a way that they are able prohibit the propagation of a certain frequency range of light. This frequency region of the electromagnetic spectrum whose propagation is prohibited by the dielectric structure is called the photonic band gap (PBG).

6.1.2. TYPES OF PHOTONIC CRYSTALS

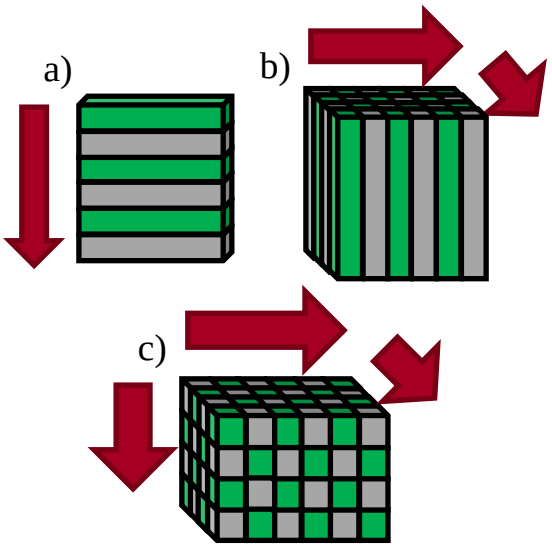

Figure 6.1. Schematic structure of the three kinds of photonic crystals: a) 1-D, b) 2-D, and c) 3-D. Red arrows display the directions in which the PBG exist in each structure.

Chapter VI

PCs are interferometric structures that take advantage of the optical properties of materials to create PBGs by accurately adjusting the structure of these crystals. Fig. 6.1 shows the different possible structures for the development of PCs. Depending on the number of dimensions in which de PBG exists, PCs can be classified as:

- **1-D PCs:** as depicted in fig. 6.1a, 1-D PCs consist of alternating two materials of refractive index n_1 and n_2. They are typically fabricated by alternate deposition of the materials onto a glass substrate. The PBG displayed by these PCs is only observed perpendicularly to the deposition plane. If thicknesses t_1 and t_2 are appropriately designed, the combined reflection of the multilayer stack will result in a PBG. The most common 1-D photonic crystal is the distributed Bragg reflector (DBR). DBRs consist of a multilayer stack in which all the layers match the following relationship [105]:

$$m\lambda = 2(n_1 t_1 + n_2 t_2) \quad (6.1)$$

Where m is the order of the Bragg condition, λ is the central wavelength of the PBG, n_i is the refractive index of the layer and t_i is the thickness of the layer.

- **2-D PCs:** depicted in fig. 6.1b, 2-D PCs display two PBGs: one in the x direction and the other in the y direction. Compared with 1-D PCs, 2-D PCs resemble a stack of 1-D PCs. However, the most common way to fabricate 2-D PCs is by drilling holes onto a substrate by combining lithographic and etching techniques [83]. In fact, NAA layers can be considered as 2-D PCs, but only NAA samples anodized at high voltages may display a PBG in the visible region due to the refractive index of anodic alumina ($n_{NAAbulk} \approx 1.67$).

- **3-D PCs:** a schematic representation of 3-D PCs is shown in fig. 6.1c. Similarly to 2-D PCs, 3-D PCs consist of a stack of 2-D PCs. This structural design allows the device to present a PBG in the three directions x, y and z. Common 3-D PCs are opals and inverse opals. Increasing the number of dimen-

sions in which a PC exist increases also the complexity and cost of the techniques required for the fabrication of such structures. This is especially true for 3-D PCs. However, bottom-up methods based on the self-assembly of monodisperse spherical nanoparticles has not only simplified the fabrication considerably but also reduced the costs [83].

6.2. OPERATING PRINCIPLE OF RUGATE FILTERS

Rugate filters are a specific kind of 1-D PCs. Similar to DBRs, rugate filters show a periodic variation of their refractive index that results in a PBG in the direction of the variation. However, this refractive index modulation is not stepwise, as in DBRs, but has a sinusoidal shape. This feature results in a single PBG without the harmonics or the sidelobes present in DBRs. Moreover, thanks to this sinusoidal variation of the refractive index, it is possible to fabricate rugate filters with complex optical responses by superimposing multiple refractive index profiles.

In order to fabricate rugate filters with a stop band centered at a desired wavelength λ_0, it is necessary to design the refractive index profile so that the refractive index reproduces the following expression [183]:

$$n(x) = n_0 + \frac{\Delta n}{2}\sin\left(\frac{4\pi x}{\lambda_0}\right) \qquad (6.2)$$

Where x is the optical path (i.e. the distance in the direction in which the PBG will be generated), n_0 is the average refractive index of the photonic structure, and Δn is the refractive index contrast.

As it can be observed from eq. 6.2, the position λ_0 of the PBG in rugate filters is very sensitive to the refractive index of the structure and frequency of the si-

nusoidal variation. This allows fine tuning of the position of λ_0 by either modifying n_0 or the oscillating frequency $4\pi x$. Moreover, if a porous material, such as pSi or NAA, is used for the fabrication of rugate filters, these photonic structures can be used as sensors thanks to their porous nature [184, 185, 186, 187, 188, 189]. This is thanks to the dependency of the effective refractive index n_{eff} in porous materials to the material filling the pores. Therefore, if a given porous rugate filter fabricated with a sinusoidal frequency f_0, centered at λ_0, and displaying a refractive index in air of n_{eff0}, is immersed in water, the effective refractive index will be shifted to n_{eff1} so that $n_{eff1} > n_{eff0}$ resulting in a redshift from λ_0 to λ_1.

6.3. FABRICATION OF RUGATE FILTERS WITH NANOPOROUS ANODIC ALUMINA

The fabrication of complex optical structures with porous materials requires precise modulation of the porosity along the film thickness. However, porosity modulation in NAA has been challenging due to the thick insulating barrier layer at the pore bottom.

The first technique developed for porosity modulation during the anodization of NAA was pulse anodization [102, 103, 104]. This technique combined mild and hard anodization regimes by using short voltage pulses that turned the anodization from mild to hard conditions. This allowed great changes in the porosity along the direction of the anodization thanks to the short pulses that avoided the stabilization of the barrier layer alumina at the pore bottom. However, despite the fact that no optical characterization was made on this innovative approach, mild to hard anodization transitions would result in abrupt refractive index variations that would not fit the requirements of eq. 6.2. Recently, current

controlled anodization procedures have been developed in order to have better control over the pore growth and fabricate PC based on NAA [109]. This novel technique shows promising results for the fabrication of complex PC by accurately designing the current profile.

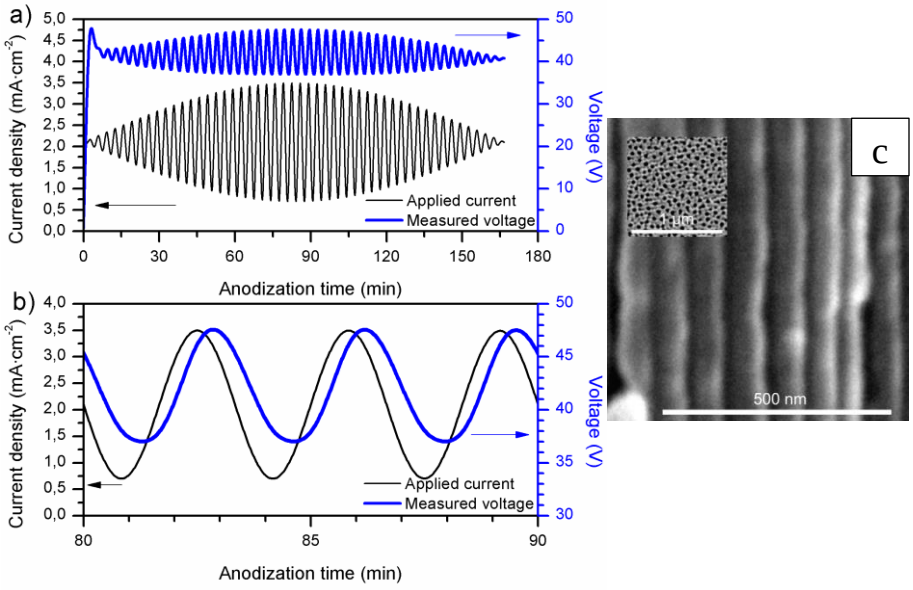

Figure 6.2. Fabrication of NAA rugate filters by means of small current variations. a) full experimental data showing the characteristic current and voltage evolution during the fabrication of an apodized NAA rugate filter; b) amplification of the region with maximum amplitude of the current profile; and c) cross sectional SEM micrograph of NAA rugate filter anodized for 300 cycles with an apodized sinusoidal current profile as seen in a), the inset shows the top view of the structure (scale bar = 1 µm). Adapted from [142].

Fig. 6.2a shows the characteristic current profile used in our facilities for the fabrication of NAA rugate filters. Our work focused on the development of ru-

gate filters under mild anodization conditions using 0.3 M $H_2C_2O_4$ as the electrolyte. To do so, the current modulation was adjusted in order to maintain a small voltage oscillation that would avoid pore branching. This oscillatory current consisted in a direct current (DC) component of 2.05 $mA \cdot cm^{-2}$ and a sinusoidal alternating current (AC) component whose maximum amplitude was 1.45 $mA \cdot cm^{-2}$ [142]. The resulting voltage depicted in fig. 6.2a shows how the current profile applied during the anodization results in an initial transitory voltage that corresponds to the BLA growth. After stabilization of the BLA, the voltage remains stable within the 37-48 V range and follows the current profile with a small delay as shown in fig. 6.2b. Thanks to this current profile, the voltage variation can be maintained within a range that avoids pore branching but still results in periodic modulation of the porosity depicted in fig. 6.2c as a smooth variation of the pore diameter along the pore axis.

These initial experiments showed really good results, but still more work needed to be done in order to fully understand the effect of NAA's structural parameters in the generation of rugate filter-based PBGs. In the following sections we are going to discuss the effect of pore ordering, number of cycles, apodization, aluminium bulk, porosity, and period time.

6.3.1. EFFECT OF PORE ORDERING

One of the most well-known features of NAA is its ability to undergo self-ordering by applying a two-step anodization procedure. In this section we are going to assess the effect of pore ordering in the performance of NAA rugate filters. In order to avoid the effects of other parameters, we analyzed the simplest current profile for rugate filter fabrication: a sine wave without apodization.

To assess the effect of pore ordering, two samples were fabricated. One of them (sample OE1) was directly anodized with the sinusoidal current profile (2.05 ± 1.45 mA·cm^{-2}) after electropolishing in EtOH:$HClO_4$ (4:1, v:v) at 20 V and 5 °C for 4 min. The other sample (sample OE2) was anodized at a constant voltage of 40 V for 20 h in order to induce pore self-ordering after electropolishing under the same conditions as sample OE1. This sacrificial layer was then selectively dissolved in a mixture of 0.4 M H3PO4 and 0.2 M H2CrO4 at 70 °C for 3 h. Finally, the resulting patterned Al foil was anodized using the same sinusoidal current profile as sample OE1. A summary of the fabrication conditions is presented in table 6.1.

Table 6.1. Fabrication conditions of the samples used for the assessment of the effect of pore ordering in NAA based rugate filters.

Sample	Electrolyte	Frequency (Hz)	1st step	Current density (mA/cm^2)	Cycles	Expected thickness (µm)
OE1	$H_2C_2O_4$ (0.3 M)	0.05	No	2.05±1.45	50	7.6
OE2			Yes		50	7.6

Fabrication curves

Fig. 6.3 and 6.4 show the experimental fabrication curves of samples OE1 and OE2 respectively. The first difference between OE1 and OE2 is their behavior during voltage stabilization. Sample OE1 shows an initial voltage peak of 57.9 V before stabilizing at 42.6 ± 4.5 V whereas for sample OE2 the initial voltage peak is 46.8 V and then displays a mean voltage of 40.3 ± 4.3 V. It can be observed also how voltage in sample OE1 is more stable than in sample OE2,

where there is a clear drift of the mean voltage after stabilization from 39.5 V to 41.1 V. These differences in the behavior is introduced by the nanostructured aluminum foil which helps to restrict the resulting mean voltage to values close to the potential used in the 1st step. However, the voltage drift may be introduced by the mean applied current, which may be not appropriate for maintaining a 40 V mean voltage throughout the anodization procedure. The amplitude of the voltage oscillation is almost the same in the two cases decreasing only by 0.2 V in sample OE2. The similar voltage amplitudes show a clear dependency with the current amplitude. Nevertheless, the slightly smaller amplitude appreciated in sample OE2 may be introduced by the 1st step which may help to maintain pore ordering in depth.

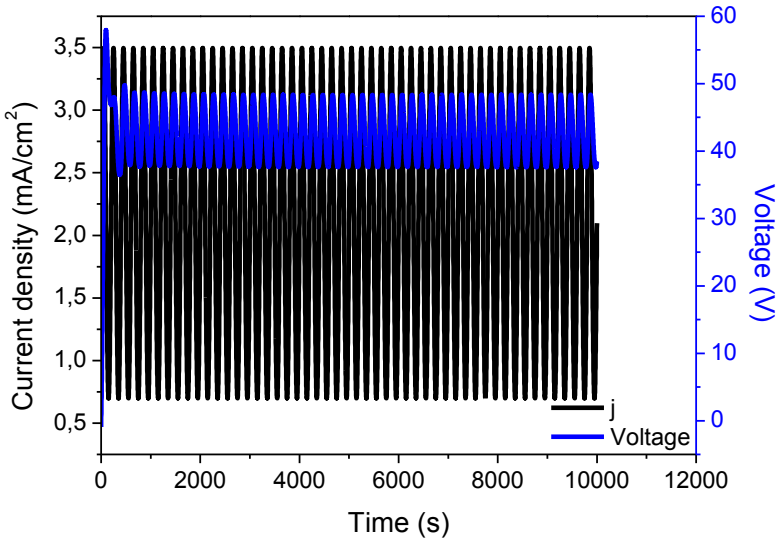

Figure 6.3. Evolution of voltage and current density (j) during the anodization of sample OE1 using a sinusoïdal current wave for 50 cycles in a sample just electropolished prior to rugate filter anodization.

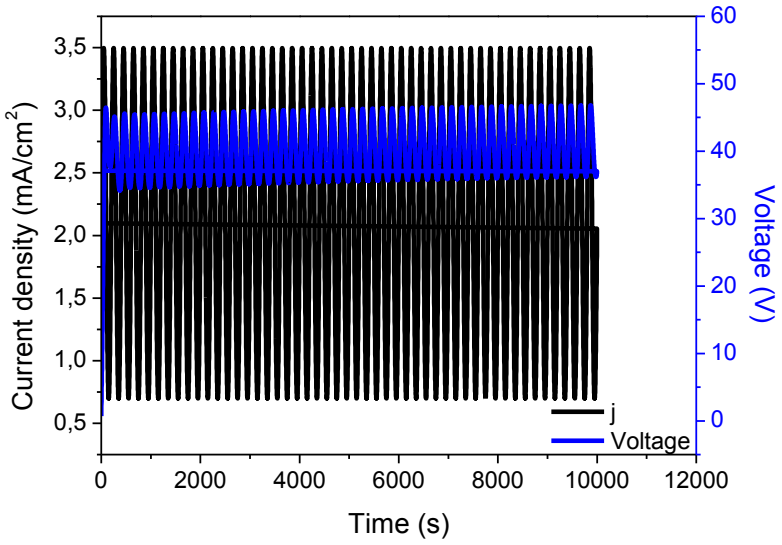

Figure 6.4. Evolution of voltage and current density (j) during the anodization of sample OE2 using a sinusoïdal current wave for 50 cycles in a sample with 1st step anodization prior to rugate filter fabrication.

Optical characterization

The reflectance of samples OE1 and OE2 was measured in the UV-Vis-NIR region to determine the effect of pore ordering on the resulting PBG. The results are shown in fig 6.5. It can be observed how in both OE1 and OE2 the position of the PBG is almost the same. This is related with the frequency (or period) of the current profile. The Fabry-Pérot oscillation present in the spectrum due to the overall thickness of the NAA rugate filter is more noticeable in OE1 than in OE2. However, the PBG is more noticeable in OE1 than in OE2. This result shows that samples manufactured in 0.3 M H2C2O4 under mild anodization conditions display better PBGs with disordered pores. This may be attributed to the 2-D PC properties of self-ordered pores which may interfere with the effi-

ciency of the PC structure along the pore axis, but more experiments should be made in order to verify this theory.

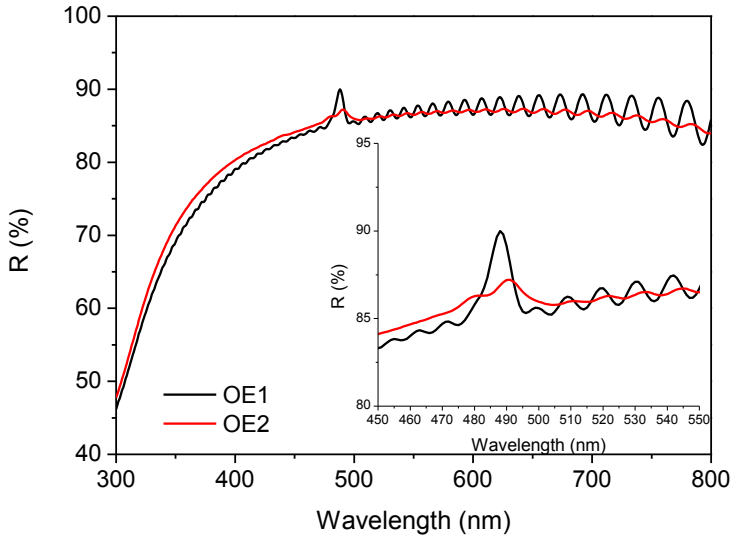

Figure 6.5. Reflectance spectra of samples OE1-OE2 with the aluminium (Al) bulk obtained with a Perkin Elmer λ 950 UV-Vis-NIR spectrophotometer coupled with the Universal Reflectance Accessory (URA). Inset shows a magnification of the resonance region.

6.3.2. EFFECT OF NUMBER OF CYCLES

Another important feature of 1-D PC is the amount of layers (or in this case, cycles) required to display a PBG [183]. This is especially interesting for biosensing applications. As we explained in section 4.3.2, thick porous layers may result in long stabilization times for biosensing experiments [174].

To experimentally determine the amount of cycles required for NAA based rugate filters to display a PBG, 4 different samples (CO1-CO4) were fabricated. Table 6.2 resumes the fabrication conditions.

Table 6.2. Fabrication conditions of NAA rugate filters anodized fabricated for the optimization of the number of cycles required for PBG generation. An expected thickness is also supplied based on our total charge calibration curve (see chapter III, section 3.4.1).

Sample	Electrolyte	Frequency (Hz)	1st step	Current density (mA/cm^2)	Cycles	Expected thickness (μm)
CO1	$H_2C_2O_4$ (0.3 M)	0.05	No	2.05±1.45	25	3.8
CO2					50	7.6
CO3					100	15.2
CO4					200	30.4

Optical characterization

Samples CO1-CO4 were measured in reflectance in the UV-Vis-NIR region to see the effect of the number of cycles in the PBG. The resulting spectra are depicted in fig. 6.6. It can be observed how as the number of cycles increases, the number of Fabry-Pérot oscillations increments and their amplitude decrease until their complete disappearance in sample CO4. This is a result of the increasing layer thickness with the number of cycles. It must also be noted that the reflection at 300 nm is strongly affected by the number of cycles. This is related with the absorption of alumina in the UV. Therefore, thicker samples result in stronger absorption in the UV region. Regarding the PBG, in all 4 samples it can

be distinguished. However, the reflecting intensity of the PBG in sample CO1 is similar to that of the Fabry-Pérot oscillations. If the number of cycles were further diminished, no PBG would be appreciated since the Fabry-Pérot oscillations would certainly mask it. It must also be noted that increasing the number of cycles results in a slight blue-shift of the PBG and also a widening of the band. This may be attributed to chemical dissolution of the pore walls of the initial layers during the anodization [108]. This dissolution may hamper the efficiency of the stop band. Therefore, further work in NAA based rugate filters should include in situ correction of the dissolution by adjusting the current profile with time.

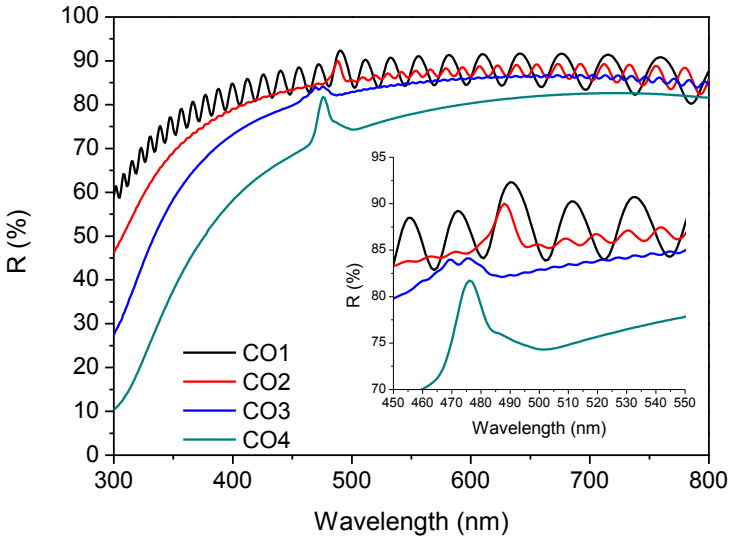

Figure 6.6. Reflectance spectra of samples CO1-CO4 with the aluminium (Al) bulk obtained with a Perkin Elmer λ 950 UV-Vis-NIR spectrophotometer coupled with the Universal Reflectance Accessory (URA). Inset shows a magnification of the ressonance region.

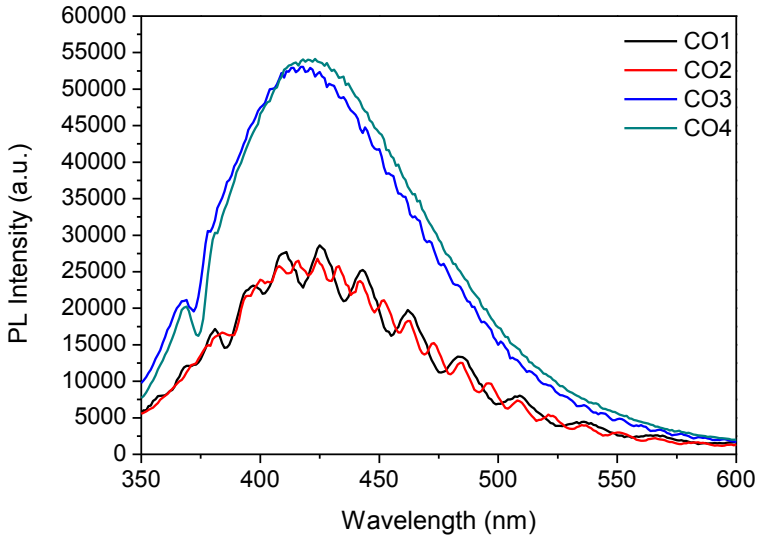

Figure 6.7. Photoluminescence spectra of samples CO1-CO4 with the aluminium (Al) bulk. The ressonance band seen in the reflectance spectra can be appreciated as a sharp localized decrease of the emission spectrum in all 4 samples.

The photoluminescent properties of samples CO1-CO4 were also studied. Given the nice reflection bands obtained in these samples, it was interesting to test their effect on the photoluminescence (PL) spectrum of NAA. As explained in section 3.4.2.2, NAA manufactured in oxalic acid under mild anodization conditions display a bright blue (≈ 425 nm) PL in the 350-600 nm region. Therefore, if a PBG is created in this region, the resulting PL spectrum should be altered. Fig. 6.7 shows the results. It can be observed how, as expected, the overall PL intensity increases with the thickness of the sample. The most interesting feature however, is the apparition of a PL dip in all four samples. It can be observed how this dip is more pronounced as the number of cycles increase. Also, the position of the dip is blue-shifted for the two thickest samples as it happened

in the reflection measurements shown in fig. 6.6. The difference between the position of the PL dips in fig. 6.7 and the stop bands in fig. 6.6 is due to the different measurement angles in the two techniques (i.e. 6 ° for reflectance and 270° for PL).

6.3.3. EFFECT OF APODIZATION

Performing an apodization on the sinusoidal current profile used for the fabrication of rugate filters is a common technique used to eliminate the sidelobes of a PBG.

Apodization consists in the modulation of the current profile. In our case, this is performed by applying a cosine function on the amplitude of the sinusoidal current wave [183]. This modulation can be performed in two ways: increasing/decreasing the amplitude of the current wave (from now on "positive" apodization), or decreasing/increasing the amplitude of the current wave (from now on "negative" apodization).

Table 6.3. Fabrication conditions of the samples used for evaluating the effect of cosine function apodization of the current wave in the performance of NAA rugate filters.

Sample	Electrolyte	Frequency (Hz)	1st step	Current density (mA/cm^2)	Cycles	Apodization	Expected thickness (µm)
AO1	$H_2C_2O_4$ (0.3 M)	0.05	Yes	2.05±1.45	50	None	7.6
AO2						Negative	
AO3						Positive	

In order to check the best apodization for the fabrication of NAA rugate filters, 3 different samples were fabricated: without apodization (control), with positive apodization and with negative apodization. The fabrication conditions of the NAA rugate filters fabricated for this optimization study are summarized in table 6.3.

No apodization

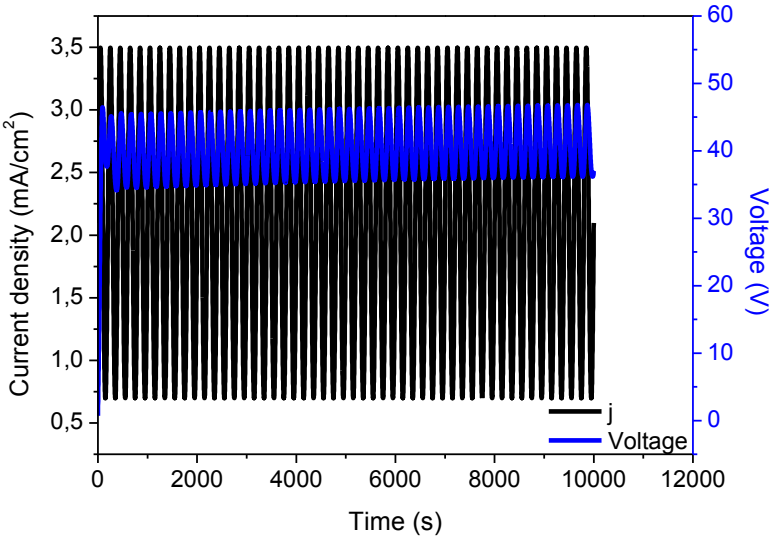

Figure 6.8. Evolution of voltage and current density (j) during the anodization using a sinusoïdal current wave for 50 cycles in a sample with 1st step anodization prior to rugate filter fabrication and no apodization of the current wave.

The experimental data from the anodization procedure of sample AO1 is shown in fig. 6.8. As it can be observed, it shows the same behavior as sample

OE2 in fig. 6.4: a stable sinusoidal variation of the voltage with a small voltage increase drift as a result of the 1st step anodization.

"Negative" apodization

The data acquired during the fabrication of sample AO2 is presented in fig. 6.9. It can be observed how "negative" apodization results in a bow-tie shaped current profile. Similarly to the other samples presented in this chapter, the voltage developed follows the shape of the current profile with a small delay. Even though the oscillatory shape of the voltage partially masks it, the mean voltage developed is not stable, it follows the shape of the cosine function used to apodize the current wave decreasing toa mean voltage value of 37.5 V in the middle of the anodization.

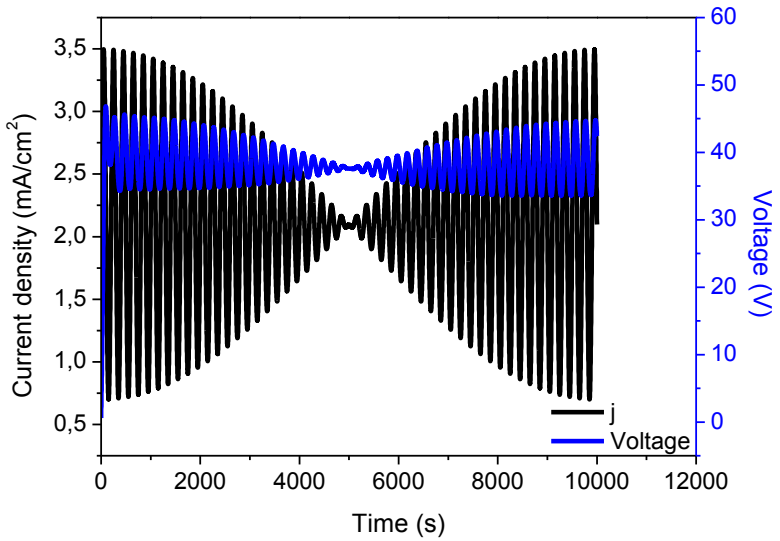

Figure 6.9. Evolution of voltage and current density (j) during the anodization using a sinusoïdal current wave for 50 cycles in a sample with 1st step ano-

dization prior to rugate filter fabrication and positive apodization of the current wave.

"Positive" apodization

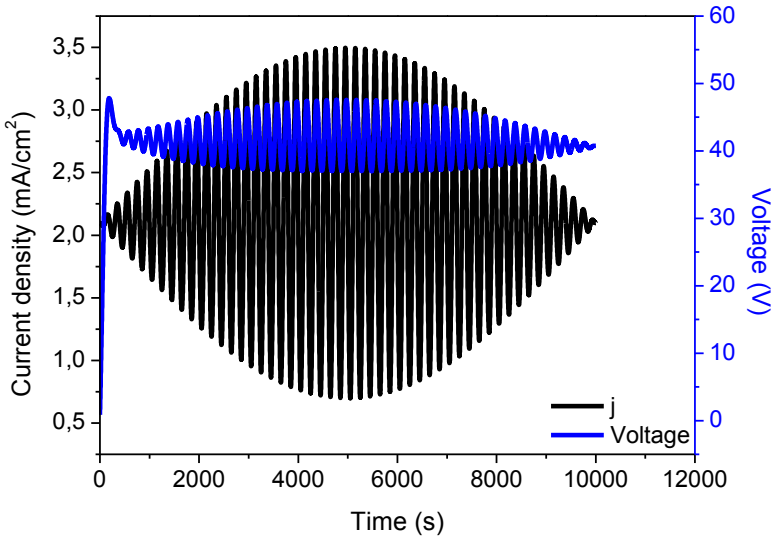

Figure 6.10. Evolution of voltage and current density (j) during the anodization using a sinusoïdal current wave for 50 cycles in a sample with 1st step anodization prior to rugate filter fabrication and negative apodization of the current wave.

Experimental data from the anodization of sample AO3 is presented in fig. 6.10. In this case, the shape of the voltage profile is not exactly the same as the one from the applied current. This is due to the fact that, similarly to AO2, the mean voltage value follows the shape of the cosine apodization function, reach-

ing a maximum mean voltage value of 41.8 V in the middle of the anodization procedure.

Results

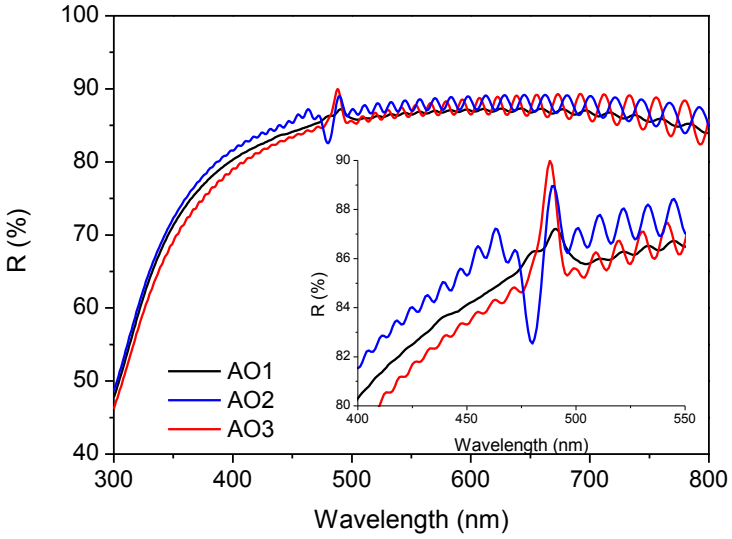

Figure 6.11. Reflectance spectra of samples AO1-AO3 with the aluminium (Al) bulk obtained with a Perkin Elmer λ 950 UV-Vis-NIR spectrophotometer coupled with the Universal Reflectance Accessory (URA). Inset shows a magnification of the resonance region**.**

In order to assess the effect of apodization on the PBG of NAA rugate filters, samples AO1-AO3 were measured in reflectance. The resulting reflectance spectra are shown in fig. 6.11. Sample AO1 was anodized with a simple sinusoidal current wave to act as a control for samples AO2 and AO3. It can be observed how the overall shape of the three samples is almost the same in the stud-

ied region and the tiny differences observed may be attributed to sample inhomogeneity rather than an effect of the current apodization. It can also be observed how the three samples show a reflection band around 480 nm, showing the good repeatability of the process for samples anodized for the same time period. Comparing samples AO2 and AO3 with the control AO1, it can be seen how samples anodized under an apodized current profile result in higher reflectivity of the stop band despite the higher amplitude of the Fabry-Pérot oscillations displayed by these samples. An interesting behavior is shown by sample AO2. Apart from displaying a reflectance band, it also presents a sharp reflectance valley immediately before. This is due to the 0 mA amplitude region in the negatively apodized current profile of sample AO2. This region could have generated a defect in the PC structure of the NAA rugate filter creating a microcavity-like structure. However, more work needs to be done in order to verify this hypothesis.

6.3.4. EFFECT OF PERIOD TIME

As explained by eq. 6.2, given a mean refractive index n and a fixed refractive index variation Δn, the frequency at which the refractive index is modulated in depth is the key parameter for tuning the position of the stop band. Therefore, according to eq. 6.2, calibration of the position of the PBG can be performed experimentally by fabricating several NAA rugate filters under different frequencies. However, since the growth of NAA is very slow, the frequency differences between the samples are very small. For this reason, in this section the period time of the current wave will be used instead of the frequency to enhance the clarity of the data.

In order to prove the possibility of tuning the PBG of NAA rugate filters by adjusting the period of the current wave, three sets of samples with periods of t_1 =200 s, t_2 = 250 s and t_3 = 300 s were fabricated. Further details on the fabrication conditions are presented in table 6.4.

Table 6.4. Fabrication conditions of the samples used for the calibration of the position of the PBG in NAA rugate filters as a function of period time.

Period time (s)	Electrolyte	Temperature (°C)	Apodization	1st step	Current density (mA/cm^2)	Cycles
200	$H_2C_2O_4$ (0.3 M)	5	None	No	2.05±1.45	50
250						
300						

Fig. 6.12a, the resulting reflectance spectra of samples NAA rugate filters anodized with period times of t_1 =200 s, t_2 = 250 s and t_3 = 300 s are presented. It can be observed how longer period times results in a redshift of the PBG. This happens because longer period times result in longer pore diameter variations along the pore axis, which result in layers with longer optical thicknesses. These longer optical thicknesses are the reason for the redshift of the PBG. Moreover, as the period time increases, the reflectance bands widen. This may be a result of the chemical etching of the porous structure due to the longer anodization times in the samples with longer periods. A calibration of the position of the PBG is shown in fig. 6.12b. The period time shows a linear relationship with the position of the reflectance band with a slope of 2.4 $nm \cdot s^{-1}$[142].

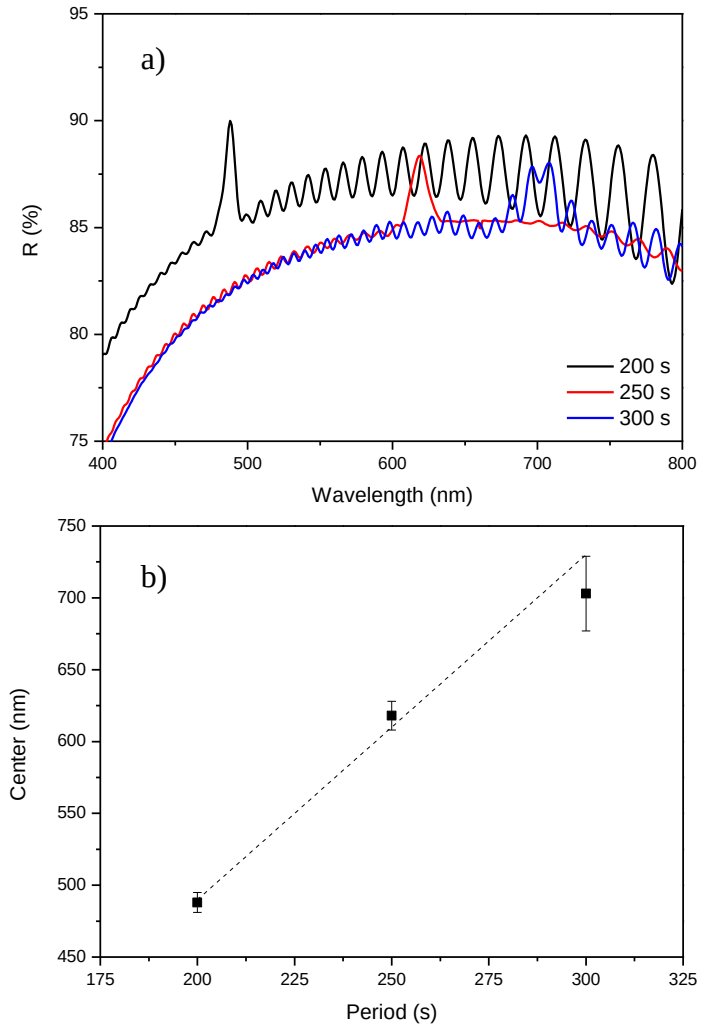

Figure 6.12. Calibration results for the fabrication of rugate filters. a) reflectance spectra of NAA rugate filters anodized with a period of 200, 250 and 300 s for 50 cycles; and b) calibration curve of the position of the ressonance band. Increasing the period time results in a red-shift of the ressonance band. Also, longer period times results in wider ressonance bands. Adapted from [142].

6.3.5. EFFECT OF PORE WIDENING

Pore widening post treatments have a direct influence on the average refractive index n of the NAA rugate filter. However, this may not be the only effect. It has been proven that NAA dissolution rate is directly dependent on the applied voltage used during the fabrication of NAA films [141]. Our approach for the fabrication of NAA rugate filters does not apply voltage, but current. Nevertheless, still voltage variations can be measured during the anodization and may result in heterogeneous dissolution of the pore walls upon pore widening post-treatment with 5 % wt. H_3PO_4 at 35 °C.

In order to assess the effect of pore widening, 4 sets of samples were fabricated and their pores widened by wet chemical etching in 5 % wt. H_3PO_4 at 35 °C for t_{pw1} = 0 min, t_{pw2} = 5 min, t_{pw3} = 10 min and t_{pw4} = 15 min. More details on the fabrication conditions of the NAA rugate filters is shown in table 6.5.

Table 6.5. Fabrication conditions of the samples used to assess the effect of pore widening post-treatments in the PBG of NAA rugate filters.

t_{pw} (min)	Electrolyte	Temperature (°C)	Apodization	1st step	Current density (mA/cm^2)	Period (s)	Cycles
0	$H_2C_2O_4$ (0.3 M)	5	None	No	2.05±1.45	200	300
5							
10							
15							

The spectra displayed in fig. 6.13 shows the resulting reflectance in the 350-800 nm range of the samples presented in table 6.5. As expected from eq. 6.2, the pore widening post-treatment resulted in a blueshift of the stop band as a result of the decrease of the refractive index due to the partial dissolution of the pore walls. Also, increasing pore widening times resulted in wider bands. This broadening is due to the refractive index contrast (Δn). The higher the Δn , the wider the stop band. As it was commented at the beginning of this section, this Δn increase is due to the heterogeneous dissolution of the pore walls as a result of the oscillatory voltage profile developed by the samples during the anodization. This voltage profile resulted in multiple dissolution rates along the pore axis depending on the voltage developed. As a result, NAA rugate filters are able to increase their Δn by the pore widening process.

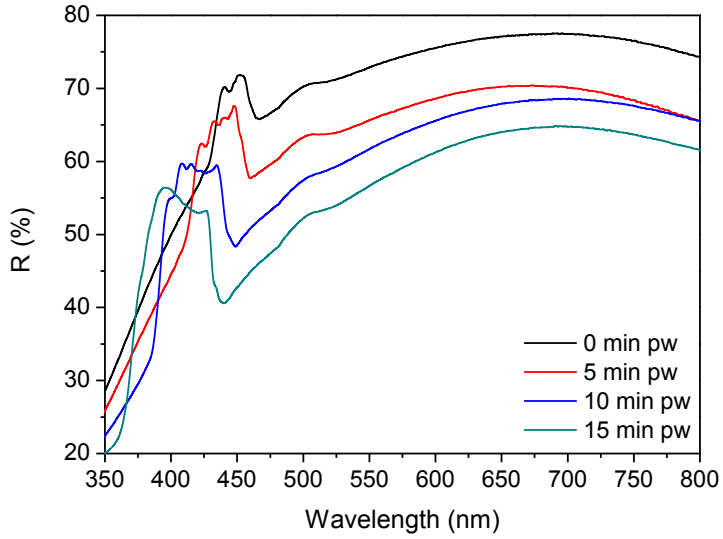

Figure 6.13. Reflectance spectra of NAA rugate filters anodized for 300 cycles, with an apodized sinusoidal current profile with a period time of 200 s. The samples were post-treated in H_3PO_4 5 % wt. at 35 ºC for 0, 5, 10 and 15 min in

order to evaluate the effect of porosity on the performance of the rugate filters. Increasing the pore widening time resulted in a blue-shift as well as in a widening of the stop band. Also, a higher porosity results in a decrease of the overall reflectivity of the sample.

6.3.6. EFFECT OF ALUMINIUM BULK

All the reflectance spectra presented so far have shown an overall high reflectance in the 400-800 nm range. This may be attributed to the high transparency of NAA manufactured in oxalic acid that allows us to see the reflectance of the Al bulk also. This high reflectance may affect the measurement of the reflectivity of the stop band due to the combination of the reflectance of the NAA rugate filter and the reflectance of the remaining Al bulk. In order to eliminate the effect of the Al bulk, the remaining Al of the samples presented in table 6.5 was selectively dissolved using a HCl/CuCl-saturated solution and the resulting samples were measured in reflectance. The results are shown in fig. 6.14.

Fig. 6.13 and 6.14 show the same NAA rugate filters before and after the dissolution of the Al bulk. It can be observed how the trend in the height of the stop band changes completely from fig. 6.13 to fig. 6.14. On the other hand, no significant shifts can be observed in the position or the width of the PBGs. This confirms the fact that the intensity of the reflectance is strongly influenced by the Al present at the bottom of the porous structure.

The elimination of the Al not only allowed a better visibility of the reflectance band, but also opened the possibility to measure the NAA rugate filters in transmission and test the performance of the PBG in light blocking. The results of the transmission measurements of NAA rugate filters are shown in fig. 6.15.

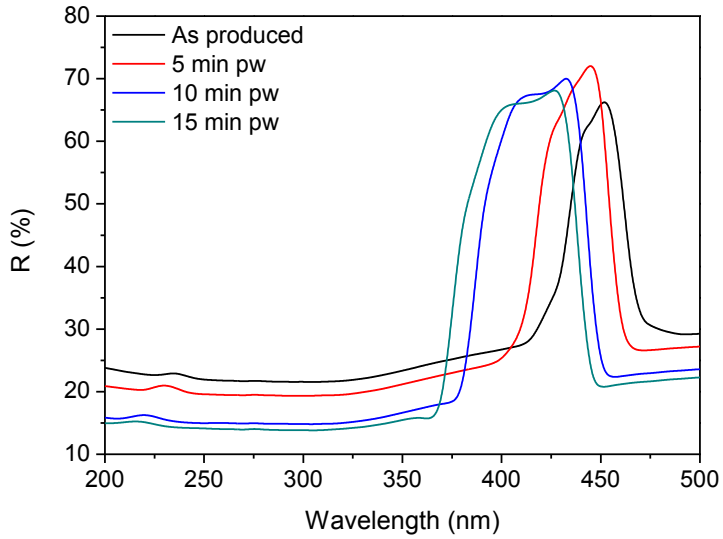

Figure 6.14. Reflectance spectra of NAA rugate filters anodized for 300 cycles, with an apodized sinusoidal current profile with a period time of 200 s. The samples were post-treated in H_3PO_4 5 % wt. at 35 ºC for 0, 5, 10 and 15 min and the remaining Al was selectively dissolved in a mixture of HCl and CuCl in order to evaluate the effect of the Al substrate on the reflectance spectra of the rugate filters. The results show that most of the reflectance outside the resonance band is due to light reflection in the NAA rugate filter/Al interface. Once the Al substrate is eliminated, the resonance band is more visible. Adapted from [142].

Transmission measurements show how the pore widening post-treatment improves the performance of the PBG. Longer pore widening times resulted in lower transmission in the stop band as well as less steep edges in the UV region, possibly due to a combination of scattering losses and the absorption of alumina. Even though the results presented do not show a perfect PBG (i.e. with a 0 % transmission in the center of the band), the tendency shows that 0 % transmis-

sion may be obtained with longer pore widening treatments in the order of 20-25 min.

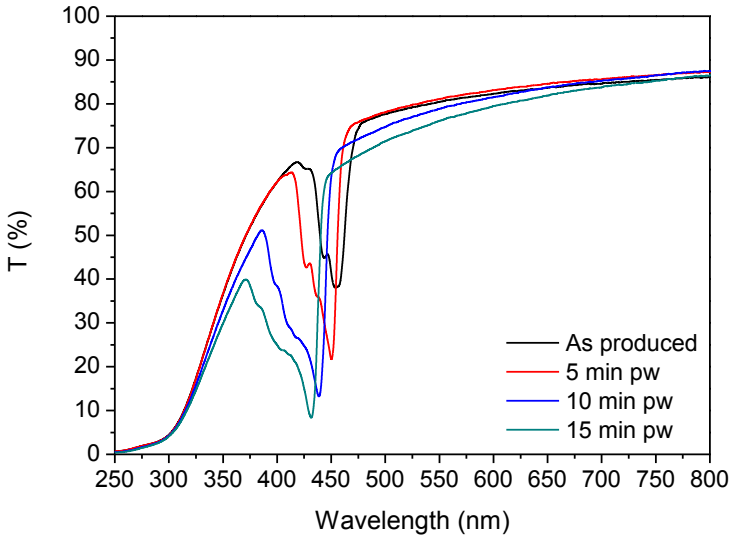

Figure 6.15. Transmitance spectra of NAA rugate filters anodized for 300 cycles, with an apodized sinusoïdal current profile with a period time of 200 s. The samples were post-treated in H_3PO_4 5 % wt. at 35 ºC for 0, 5, 10 and 15 min. As in the reflectance spectra, increasing the porosity results in a blue-shift and a widening of the ressonance band. After 15 min of pore widening, the NAA rugate filters allows just a 10 % of transmission in its ressonance band. Further chemical etching of the pores could result in a stop-band in the resso-nance region. Adapted from [142].

6.4. SENSING WITH NAA RUGATE FILTERS

In the previous section, the basics of the fabrication and the effect of the key parameters involved in the generation of NAA rugate filters have been present-ed. This photonic structure, combined with the properties of NAA, shows prom-ising results for the development of optical biosensors.

To determine the possibilities of NAA rugate filters for optical biosensing, a real-time detection experiment was performed with a sample from table 6.5. In order to decide which NAA rugate filter was better for the sensing experiment, a Gaussian fit of the stop band was performed in each of the spectra after Al removal in order to extract the central wavelength (λ_0), the full width at half maximum (FWHM) and the height of the reflectance band (h). With these data, it was possible to calculate the quality factor (Q_f) of the four kinds of NAA rugate filters as follows:

$$Q_f = \frac{\lambda_0}{FWHM} \tag{6.3}$$

Where Q_f is the quality factor, λ_0 is the wavelength at which the stop band is centered and FWHM is the full width at half maximum obtained from the Gaussian fitting.

Since the detection algorithms may also be influenced by the contrast (i.e. the height of the reflectance band), the decision was not solely made on the Q_f value but on the combination of the height (h) of the reflectance band and the Q_f (i.e. $h \cdot Q_f$). As seen in table 6.6, the sample with the highest $h \cdot Qf$ is the one with a pore widening of 5 min.

Table 6.6. Results from the Gaussian fitting on the spectra shown in fig. 6.14 and the corresponding quality factors for each of the NAA rugate filters.

t_{pw} (min)	λ_0 (nm)	FWHM (nm)	h (%)	Qf	$h \cdot Q_f$
0	448	27	43.4	16.6	720.1
5	438	31	52.7	14.1	744.6
10	418	43	58.1	9.7	564.8
15	411	46	57.8	8.9	516.4

Once determined that the best NAA rugate filter consisted in 300 cycles, t_{pw} = 5 min and without Al, a proof of concept real-time sensing experiment was performed. This experiment consisted in the monitorization of the reflectance band in real time in a custom-made flow cell under different filling mediums. First of all, a reference signal was obtained for the sample in air. Then EtOH was flowed under a constant rate of 1 ml·min^{-1}. Subsequently, DI water was flowed into the chamber at the same flow rate in order to check if the structure was sensitive enough to detect the small refractive index change between EtOH and DI water. Finally, EtOH was flowed again to verify the repeatability of the system. The measured position of the reflectance band during the experiment is shown in fig. 6.16.

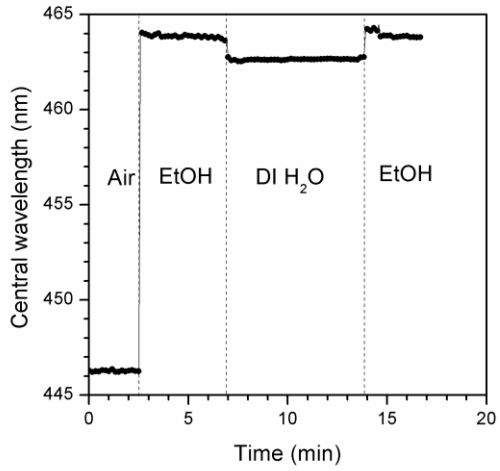

Figure 6.16. Real-time measurement of a NAA rugate filter in a flow-cell where EtOH, de-ionized water and EtOH were serially flushed in to the chamber. Adapted from [142].

The results of the real-time measurements show that the structure can clearly difference between the three distinct filling media (air, DI water and EtOH) with

a highly stable signal that shows no significant drift within the time studied as well as a low noise level of just 0.04 nm. Moreover, being able to distinguish between two liquids with a similar refractive index such as DI water (nwater = 1.333) and EtOH (nEtOH = 1.362) means that the structure is readily able to detect changes of 0.029 RIU (refractive index units) with a sensitivity of 48.8 $nm \cdot RIU^{-1}$. Also, the second EtOH infiltration resulted in the reflection band returning to the position of the first EtOH infiltration after a short transitory time thus indicating the high reproducibility of the system [142].

6.5. SUMMARY

In this chapter we have presented a novel photonic structure in NAA for sensing applications: the rugate filter. This photonic structure is a specific kind of 1-D PC. It consists of a layer of NAA in which the refractive index is modulated sinusoidally so that the reflection of a specific wavelength is enhanced, thus resulting in a PBG.

The fabrication procedure of NAA consisted in the anodization of aluminum foils in oxalic acid under mild anodization conditions using a sinusoidal current wave displaying small variations of just 1.45 $mA \cdot cm^{-2}$ on a DC component of 2.05 $mA \cdot cm^{-2}$. Also, the position of the stop band arising from the multilayer structure can be finely tuned by adjusting the period time of the current oscillations. The parameters involved in the fabrication of NAA rugate filters have been studied in detail to determine their effect on the PBG of the structure. The optimized structure for sensing applications would be the following:

- **Disordered pores:** our results show that better definition of the PBG is achieved when the nanopores display a disordered arrangement.

- **Anodized during 50 cycles:** the number of cycles is critical, since too few cycles would result in no PBG and too many cycles would result in samples too thick to be able to respond fast upon infiltration of the analyte solution. Even though our results show that with 25 cycles it is enough to see a PBG, it is advisable to perform the anodization for a total of 50 cycles to obtain a clearer PBG without having an excessive thickness.
- **"Positive" apodization of the current wave:** from all the three apodization possibilities studied, the so-called "positive" apodization shows the best PBG without sidelobes. "Negative" apodization is also an interesting structure, but it resembles more to a microcavity than a rugate filter. For that reason, "negative" apodization was discarded. However, more work should be performed in this structure in order to determine its possible applications.
- **Without Al bulk:** due to the high transparency of NAA, if the remaining Al is not removed, the resulting reflectance would be the combination of the stop band arising from the PC structure and the response from the reflection at the NAA/Al interface. This combination of reflections partially mask the reflectance band and may interfere with the peak detection algorithms.
- **5 min of pore widening:** our results show that the best $h \cdot Q_f$ is achieved for samples where the pores were widened for 5 min by wet chemical etching. However, even though the performance of optical resonators is strongly influenced by their quality factor, the pores should also provide sufficient volume for both the bioreceptor and the analyte of interest. Therefore, these 5 min of pore widening should be taken as a recommendation and not as a necessary feature, as wider pores may be required depending on the analyte of interest.

Moreover, a NAA rugate filter structure consisting of 300 cycles at a period time of t = 200 s and 5 min of pore widening was tested in a flow cell to determine its sensitivity to refractive index variations by serial infiltration of EtOH/DI water/EtOH. The real-time measurement showed that the NAA rugate

filter structure displays a highly stable and repeatable signal with a noise level of just 0.04 nm and a sensitivity of 48.8 nm·RIU^{-1}. These are promising results for the sensing applications of NAA rugate filters fabricated under small current variations, but still more work has to be done in order to develop fully functional biosensors based on this photonic structure.

Chapter VI

CHAPTER VII

CONCLUSIONS

In this Ph.D. thesis it has been presented the possibility to use NAA as a nanostructured substrate for the development of label-free optical biosensors. Among the available techniques for biosensing presented in chapter II, optical biosensing was chosen due to its high sensitivity. From the optical techniques presented for the detection of biomolecular interactions, this work has focused on the use of RIfS for the detection of binding events, which is a very sensitive technique that allows the measurement of the thin films in reflectance. With this technique, three different structures of increasing complexity have been presented and tested to assess their sensing capabilities: monolayers, bilayers and rugate filters.

Chapter III has presented the basics of NAA fabrication. Several techniques have been discussed such as ordering techniques (i.e. nanoimprinting or two-step anodization), and anodization techniques (i.e. mild and hard anodization). Also, the calibration curves used throughout this thesis for precise manufacture of NAA thin films with high repeatability are shown for layer thickness (either with time or total charge control) and for pore widening in phosphoric acid. Finally, optical characterization has been presented showing the basic effects of structural parameters, such as layer thickness and porosity, on the refractive index of the thin films as well as their photoluminescence properties.

Chapter IV has shown all the work made with NAA monolayers for biosensing purposes. After a brief introduction of the working principle of NAA monolayers for biosensing and the available data processing algorithms, a systematic review of the effect of the structural parameters on the sensing performance is presented. It has been shown how interpore distance, layer thickness, and pore diameter play a major role on the sensitivity of the monolayers. Moreover, the effect of pore diameters is supported by experimental data. The conclusions from this analysis showed that, for optimum

and fast detection, NAA biosensors should be manufactured so that interpore distance is kept as small as possible (while still providing pores large enough for the accommodation of the receptor and the target analyte), with the highest porosity possible that avoids collapsing of the porous structure and the smallest layer thickness possible which, for FFT algorithms is 2 µm. However, the experimental results also showed that this optimum structure resulted in poor resolution of the interferometric oscillations. Nevertheless, this issue is also assessed, and can be solved by deposition of a thin layer of metal, such as gold, to enhance the oscillatory pattern.

In chapter V, an innovative NAA structure is presented: the double layer interferometer. This optical device allows self-referencing for the correction of environmental drifts without requiring a secondary device. After an introductory section explaining the working principle and the data processing required, two possible techniques for self-referencing are discussed: dual functionalization and size exclusion. The technique chosen for the design of NAA bilayers was size-exclusion for the ability to separate proteins from the solvent and address the sole effect of solvent composition during the biosensing experiment. With this purpose, the biosensor design was optimized and tested with BSA to determine its size exclusion performance. The results showed that 30 nm were enough to exclude BSA from the reference layer. However, it would be recommended to diminish this diameter even further to obtain better excluding performances. As a conclusion, the optimal structure should consist of a top layer of a 2-µm thick film with the highest porosity possible, and a bottom layer consisting of a 4-µm thick film with pores with a diameter below 30 nm. Finally, a thin metal deposition on the top of the layer would be advisable to enhance the visibility of the oscillations.

Chapter VI shows the results of an even more complex structure. This structure is a 1-D photonic crystal manufactured by making a smooth sinusoidal variation of the refractive index along the pore axis. This structure is also known as a rugate filter. This innovative structure was fabricated by an innovative procedure developed during the Ph.D. consisting in applying a sinusoidal current profile. The effect of ordering, number of sinus cycles, apodization, pore widening, period time and aluminum bulk have been experimentally assessed in order to obtain well resolved reflectance bands. Moreover, the structure has been tested to determine its sensitivity to refractive index by real-time monitorization of the position of the reflectance band upon infiltration with DI water and EtOH. Results showed a sensitivity of 48.8 $nm \cdot RIU^{-1}$. Based on the results, a preliminary optimum structure for sensing applications has been proposed. This structure consisted on disordered pores anodized for a total of 50 cycles using a "positively" apodized sinusoridal current profile. Also, for full observation of the band, the aluminum bulk has to be dissolved. Regarding the porosity, the best $h \cdot Q_f$ factor achieved was after 5 min of pore widening. However, this should not be used as a mandatory condition but as a recommendation and should be modified in order to supply sufficient space for the diffusion of the target analyte.

All the data presented in this work has the potential of enhancing the sensitivity of NAA optical biosensors. By appropriately applying the recommendations arising from the results presented, faster and more sensitive devices may be developed. However, this work just focused on electrostatically based biosensing surface modification. Therefore, further developments in this field should focus on the optimization of surface chemical modification and the subsequent covalent attachment of bioreceptors on the pore

walls in a directional manner. This would significantly improve even further the sensitivity and selectivity of the optical biosensors based on NAA.

As a concluding remark, the humble opinion of the writer is that further research in the design of optical biosensors based on NAA should be focused on improving rugate filters. The work presented here has assessed most of the issues but there is still room for improving it. At first sight, this may be controversial, as the fabrication procedure is more complex to perform. The reason for this remark is based mainly on the simplicity of the data processing algorithm. The most accepted procedure for analyzing mono and bilayers of NAA is based on applying a FFT and afterwards, monitoring the resulting frequency peak whose position is the EOT of the film. This algorithm is complex and limits the speed at which the real-time detection can be performed due to its computational effort. Moreover, some errors may be introduced due to the approximations assumed and the resolution of the resulting FFT plot. However, real-time monitorization of rugate filters is much simpler, since it avoids mathematical transformation of the raw data. Therefore, resolution is just limited by the device (i.e. the spectrophotometer).

REFERENCES

1. Clark L. C. Monitor and control of blood and tissue oxygen tensions. *Trans. Am. Soc. Art. Int. Org.* **1956**, *2*, 41-48.
2. Clark L. C., Lyons C. Electrode systems for continuous monitoring in cardiovascular surgery. *Ann. NY Acad. Sci.* **1962**, *102*, 29-45.
3. Bergveld P. Development of an ion-sensitive solid-state device for neurophysiological measurements. *IEEE Trans. Bio. Med. Eng.* **1970**, *BME-17*, 70-71.
4. Guilbault G. G., Montalvo J. G. An enzyme electrode for the substrate urea. *J. Am. Chem. Soc.* **1970**, *92*, 2533-2538.
5. Mosbach K., Danielsson B. An enzyme thermistor. *Biochim. Biophys. Acta* **1974**, *364*, 140-145.
6. Divis C. Notes on ethanol oxidation by a microbial electrode Acetobacter zylinum. *Ann. Microbiol.* **1975**, *126*, 175-186.
7. Lubbers D. W., Opitz N. The pCO2-/pO2 optode: a new probe for measurement of pCO2 or pO2 in fluids and gases. *Z. Res. Nat. C* **1975**, *30*, 532-533.
8. Liedberg W., Nylander C., Lundstern I. Surface plasmon resonance for gas detection and biosensing. *Sensor Actuators A Phys.* **1983**, *4*, 299-304.
9. Cass A. E. , Davis G., Francis G. D., Hill H. A., Aston W. J., Higgins I. J., Plotkin E. V., Scott L. D., Turner A. P. Ferrocene-mediated enzyme electrode for amperometric determination of glucose. *Anal. Chem.* **1984**, *56*, 667-671.
10. Gauglitz G., Krause-Bonte J. Spectral Interference Refractometry by Diode Array Spectrometry. *Anal. Chem.* **1988**, *60*, 2609-2612.

References

11. IUPAC. Compendium of Chemical Terminology, 2nd ed. (the "Gold Book"). Compiled by A. D. McNaught and A. Wilkinson. Blackwell Scientific Publications, Oxford (1997). XML on-line corrected version: http://goldbook.iupac.org (2006-) created by M. Nic, J. Jirat, B. Kosata; updates compiled by A. Jenkins. ISBN 0-9678550-9-8. doi:10.1351/goldbook. Last update: 2014-02-24; version: 2.3.3.
12. Daniels J.S., Pourmand N. Label-Free Impedance Biosensors: Opportunities and Challenges. *Electroanal.* **2007**, *19*, 1239-1257.
13. Thakur M.S., Ragavan K.V. Biosensors in food processing. *J. Food Sci. Technol.* **2013**, *50*, 625-641.
14. Ibupoto Z.H., Elhag S., AlSalhi M.S., Nur O., Willander M. Effect of Urea on the Morphology of Co_3O_4 Nanostructures and Their Application for Potentiometric Glucose Biosensor. *Electroanal.* **2014**, *26*, 1773-1781.
15. Yang Z., Zhang C., Zhang J., Bai W. Potentiometric glucose biosensor based on core-shell Fe_3O_4-enzyme-polypyrrole nanoparticles. *Biosens. Bioelectron.* **2014**, *51*, 268-273.
16. Hernández R., Vallés C., Benito A.M., Maser W.K., Rius F.X., Riu J. Graphene-based potentiometric biosensor for the immediate detection of living bacteria. *Biosens. Bioelectron.* **2014**, *54*, 553-557.
17. Marchenko S.V., Kucherenko I.S., Hereshko A.N., Panasiuk I.V., Soldatkin O.O., El'skaya A.V., Soldatkin A.P. Application of potentiometric biosensor based on recombinant urease for urea determination in blood serum and hemodialyzate. *Sensor. Actuat. B-Chem.* **2014**, In press.
18. Belluzo M.S., Ribone M.E., Lagier C.M. Assembling Amperometric Biosensors for Clinical Diagnostics. *Sensors* **2008**, *8*, 1366-1399.
19. Kaçar C., Dalkiran B., Erden P.E., Kiliç E. An amperometric hydrogen peroxide biosensor based on Co_3O_4 nanoparticles and multiwalled car-

bon nanotube modified glassy carbon electrode. *Appl. Surf. Sci*. **2014**, *311*, 139-146.

20. Eletxigerra U., Martinez-Perdiguero J., Merino S., Villalonga R., Pingarrón J.M., Campuzano S. Amperometric magnetoimmunoassay for the direct detection of tumor necrosis factor alpha biomarker in human serum. *Anal. Chim. Acta* **2014**, *838*, 37-44.
21. Campos P.P., Moraes M.L., Volpati D., Miranda P.B., Oliveira O.N.Jr., Ferreira M. Amperometric Detection of Lactose Using β-Galactosidase Immobilized in Layer-by-Layer Films. *ACS Appl. Mater. Interfaces* **2014**, *6*, 11657-11664.
22. Nouira W., Maaref A., Elaissari A., Vocanson F., Siadat M., Jaffrezic-Renault N. Enhanced Response of Proteinas K-Based Conductometric Biosensor Using Nanoparticles. *Sensors* **2014**, *14*, 13298-13307.
23. Zhang Z., Luo L., Chen G., Ding Y., Deng D., Fan C. Tryptamine functionalized reduced graphene oxide for label-free DNA impedimetric biosensing. *Biosens. Bioelectron.* **2014**, *60*, 161-165.
24. Tak M., Gupta V., Tomar M. Flower´like ZnO nanostructure based electrochemical DNA biosensor for bacterial meningitis detection. *Biosens. Bioelectron.* **2014**, *59*, 200-207.
25. Wang Y., Ye Z., Ping J., Jing S., Ying Y. Development of an aptamer-based impedimetric bioassay using microfluidic system and magnetic separation for protein detection. Biosens. Bioelectron 2014, 59, 106-111.
26. Tsouti V., Boutopoulos C., Zergioti I., Chatzandroulis S. Capacitive microsystems for biological sensing. *Biosens. Bioelectron.* **2011**, *27*, 1-11.
27. Mahadhy A., Stähl-Wernersson E., Mattiasson B., Hedström M. Use of a capacitive affinity biosensor for sensitive and selective detection and quantification of DNA-A model study. *Biotechnol. Rep.* **2014**, *3*, 42-48.

28. Altintas Z., Kallempudi S.S., Gurbuz Y. Gold nanoparticle modified capacitive sensor platform for multiple marker detection. *Talanta* **2014**, *118*, 270-276.
29. Alizadeh, T., Akbari A. A capaitive biosensor for ultra-trace level urea determination based on nano-sized urea-imprinted polymer receptors coated on graphite electrode surface. *Biosens. Bioelectron.* **2013**, *43*, 321-327.
30. Xu S. Electromechanical biosensors for pathogen detection. *Microchim. Acta* **2012**, *178*, 245-260.
31. Wang X., Yu H., Lu D., Zhang J., Deng W. Label free detection of the breast cancer biomarker CA15.3 using ZnO nanorods coated quartz crystal microbalance. *Sensor. Actuat. B-Chem.* **2014**, *195*, 630-634.
32. Shan W., Pan Y., Fang H., Guo M., Nie Z., Huang Y., Yao S. An aptamer-based quartz crystal microbalance biosensor for sensitive and selective detection of leukemia cells using silver-enhanced gold nanoparticle label. *Talanta* **2014**, *126*, 103-135.
33. Kim S., Choi S.-J. A lipid-based method for the preparation of a piezoelectric DNA biosensor. *Anal. Biochem.* **2014**, *458*, 1-3.
34. Alenus J., Ethirajan A., Horemans F., Weustenraed A., Csipai P., Gruber J., Peeters M., Cleij T.J., Wagner P. Molecularly imprinted polymers as synthetic receptors for the QCM-D-based detection of L-nicotine in diluted saliva and urine samples. *Anal. Bioanal. Chem.* **2013**, *405*, 6479-6487.
35. Zhang G. Nanostructure-Enhanced Surface Acoustic Waves Biosensor and Its Computational Modeling. *J. Sens.* **2009**, *2009*, 215085
36. Sankaranarayanan S.K.R.S., Singh R., Bhethanabotla V.R. Acoustic streaming induced elimination of nonspecifically bound proteins from a Surface acoustic wave biosensor: Mechanism prediction using fluid-structure interaction models. *J. Appl. Phys.* **2010**, *108*, 104507.

37. Fu Y.Q., Luo J.K., Du X.Y., Flewitt A.J., Li Y., Markx G.H., Walton A.J., Milne W.I. Recent developments on ZnO films for acoustic wave based bio-sensing and microfluidic applications: a review. *Sensor. Actuat. B-Chem.* **2010**, *143*, 606-619.
38. Bröker P., Lücke K., Perpeet M., Gronewold T.M.A. A nanostructured SAW chip-based biosensor detecting cancer cells. *Sensor. Actuat. B-Chem.* **2012**, *165*, 1-6.
39. Ma L., Wang C., Zhang M. Detecting protein adsorption and binding using magnetic nanoparticle probes. *Sensor. Actuat. B-Chem.* **2011**, *160*, 650-655.
40. Ghosh S., Mishra S., Mukhopadhyay R. Enhancing sensitivity in a piezoresistive cantilever-based label-free DNA detection using ssPNA sensor probes. *J. Mater. Chem. B* **2014**, *2*, 960-970.
41. Johnson B.N., Mutharasan R. Biosensing using dynamic-mode cantilever sensors: A review. *Biosens. Bioelectron.* **2012**, *32*, 1-18.
42. Cui X., Gao G., Qiu Y. Accelerated myotube formation using bioprinting technology for biosensor applications. *Biotechnol. Lett.* **2013**, *35*, 315-320.
43. Tomkins M.R., Chow J., Lai Y., Docoslis A. A coupled cantilever-microelectrode biosensor for enhanced pathogen detection. *Sensor. Actuat. B-Chem.* **2013**, *176*, 248-252.
44. Gauglitz G. Direct optical detection in bioanalysis: an update. *Anal. Bioanal. Chem.* **2010**, *398*, 2363-2372.
45. Estevez M.-C., Otte M.A., Sepulveda B., Lechuga L.M. Trends and challenges of refractometric nanoplasmonic biosensors: A review. *Anal. Chim. Acta.* **2014**, *806*, 55-73.
46. Hamers D., van Voorst Vader L., Borst J.W., Goedhart J. Development of FRET biosensors for mammalian and plant systems. *Protoplasma* **2014**, *251*, 333-347.

47. Gingras A., Sarette J., Shawler E., Lee T., Freund S., Holwitt E., Hicks B.W. Fluorescent proteins as biosensors by quenching resonance energy transfer from endogenous tryptophan: Detection of nitroaromatic explosives. *Biosens. Bioelectron.* **2013**, *48*, 251-257.
48. Su. D., Teoh C.L., Sahu S., Das R.K., Chang Y.-T. Live cells imaging using a turn-on FRET-based BODIPY probe for biothiols. *Biomaterials* **2014**, *35*, 6078-6085.
49. Sanders M., Lin Y., Wei J., Bono T., Lindquist R.G. An enhanced LSPR fiber-optic nanoprobe for ultrasensitive detection of protein biomarkers. *Biosens. Bioelectron.* **2014**, *61*, 95-101.
50. Grego S., Gilchrist K.H., Carlson J.B., Stoner B.R. A compact and multichannel optical biosensor based on a wavelength interrogated grating coupler. *Sensor. Actuat. B-Chem.* **2012**, *161*, 721-727.
51. Hulme J., Malins C., Singh K., Fielden P.R., Goddard N.J. Internally-referenced resonant mirror for chemical and biochemical sensing. *Analyst* **2002**, *127*, 1233-1236.
52. Sarkar S., Gunda N.S.K., Jamal I., Mitra S.K. Optical biosensors with an integrated Mach-Zehnder Interferometer for detection of listeria monocytogenes. *Biomed. Miacrodevices* **2014**, *16*, 509-520.
53. Schmitt K., Schirmer B., Hoffmann C., Brandenburg A., Meyrueis P. Interferometric biosensor based on planar optical waveguide sensor chips for label-free detection of surface bound bioreactions. *Biosens. Bioelectron.* **2007**, *22*, 2591-2597.
54. Bertucci A., Manicardi A., Candiani A., Giannetti S., Cucinotta A., Spoto G., Konstantaki M., Pissadakis S., Selleri S., Corradini R. Detection of unamplified genomic DNA by a PNA-based microstructured optical fiber (MOF) Bragg-grating optofluidic system. *Biosens. Bioelectron.* **2015**, *63*, 248-254.

55. Lin V.S.-Y., Motesharei K., Dancil K.-P.S., Sailor M.J., Ghadiri M.R. A Porous Silicon-Based Optical Interferometric Biosensor. *Science* **1997**, *278*, 840-843.
56. Krismastuti F.S.H., Brooks W.L.A., Sweetman M.J.m Sumerlin B.S., Voelcker N.H. A photonic glucose biosensor for chronic wound prognostics. *J. Mater. Chem. B* **2014**, *2*, 3972-3983.
57. Mun K.-S., Alvarez S.D., Choi W.-Y., Sailor M.J. A Stable, Label-free Optical Interferometric Biosensor Base don TiO2 Nanotube Arrays. *ACSNano* **2010**, *4*, 2070-2076.
58. Kumeria T., Santos A., Losic D. Nanoporous Anodic Alumina Platforms: Engineered Surface Chemistry and Structure for Optical Sensing Applications. *Sensors* **2014**, *14*, 11878-11918.
59. Orosco M.M., Pacholski C., Sailor M.J. Real-time monitoring of enzyme activity in a mesoporous silicon double layer. Nat. Nanotechnol. 2009, 4, 255-258.
60. Kilian K.A., Böcking T., Gaus K., Gal M., Gooding J.J. Peptide-Modified Optical Filters for Detecting Protease Activity. *ACSNano* **2007**, *1*, 355-361.
61. Zhang H., Jia Z., Lv X., Zhou J., Chen L., Liu R., Ma J. Porous silicon optical microcavity biosensor on silicon-on-insulator wafer for sensitive DNA detection. *Biosens. Bioelectron.* **2013**, *44*, 89-94.
62. Tamanaha C.R., Mulvaney S.P., Rife J.C., Whitman L.J. Magnetic labeling, detection and system integration. *Biosens. Bioelectron.* **2008**, *24*, 1-13.
63. Kriz K., Ibraimi F., Lu M., Hansson L.-O., Kriz D. Detection of C-Reactive Protein Utilizing Magnetic Permeability Detection Based Immunoassays. *Anal. Chem.* **2005**, *77*, 5920-5924.
64. Chai Y., Wikle H.C., Wang Z., Horikawa S., Best S., Cheng Z., Dyer D.F., Chin B.A. Design of a surface-scanning cooil detector for direct

bacteria detection on food surfaces using a magnetoelastic biosensor. *J. Appl. Phys.* **2013**, *114*, 104504.

65. Sarangi S., Tan I.C., Brazdeikis A. Magnetic imaging method base don magnetic relaxation of magnetic nanoparticles. *J. Appl. Phys.* **2009**, *105*, 093926.
66. Adolphi N.L., Butler K.S., Lovato D.M., Tessier T.E., Trujillo J.E., Hathaway H.J., Fegan D.L., Monson T.C., Stevens T.E., Huber D.L., Ramu J., Milne M.L., Altobelli S.A., Bryant H.C., Larson R.S., Flynn E.R. Imaging of Her2-targeted magnetic nanoparticles for breast cancer detection: comparison of SQUID-detected magnetic relaxometry and MRI. *Contrast Media Mol. Imaging* **2012**, *7*, 308-319.
67. Thompson W. On the Electro-dynamic Qualities of Metals:-Effects of Magnetization on the Electric Conductivity of Nickel and of Iron. *Proc. R. Soc. Lond.* **1857**, *8*, 546-550.
68. Lee C.-P., Lai M.-F., Huang H.-T., Lin C.-W., Wei Z.-H. Wheatstione bridge giant-magnetoresistance based cell counter. *Biosens. Bioelectron.* **2014**, *57*, 48-53.
69. Miller M.M., Prinz G.A., Cheng S.-F., Bounnak S. Detection of a micron-sized magnetic sphere using a ring-shaped anisotropic magnetoresistance-based sensor: A model for magnetoresistance-based biosensor. *Appl. Phys. Lett.* **2002**, *81*, 2211-2213.
70. Cardoso F.A., Germano J., Ferreira R., Cardoso S., Martins V.C., Freitas P.P.,Piedade M.S., Sousa L. Detection of 130 nm magnetic particles by a portable electronic platform using spin valve and magnetic tunnel junction sensors. *J. Appl. Phys.* **2008**, *103*, 07A310.
71. Parkin S.S.P., Kaiser C., Panchula A., Rice P.M., Hughes B., Samant M., Yang S.-H. Giant tunneling magnetoresistance at room temperature with MgO (100) tunnel barriers. *Nat. Mater.* **2004**, *3*, 862-867.

72. Li F., Kosel J. An efficient biosensor made of an electromagnetic trap and a magneto-resistive sensor. *Biosens. Bioelectron.* **2014**, *59*, 145-150.
73. Sandhu A., Kumagai Y., Lapicki A., Sakamoto S., Abe M., Handa H. High efficiency Hall effect micro-biosensor platform for detection of magnetically labeled biomolecules. *Biosens. Bioelectron.* **2007**, *22*, 2115-2120.
74. Osterberg F.W., Rizzi G., Zardán Gómez de la Torre T., Strömberg M., Stromme M., Svedlindh P., Hansen M.F. Measurements of Brownian relaxation of magnetic nanobeads using planar Hall effect bridge sensors. *Biosens. Bioelectron.* **2013**, *40*, 147-152.
75. Sinha B., Ramulu T.S., Kim K.W., Venu R., Lee J.J., Kim C.G. Planar Hall magnetoresistive aptasensor for thrombin detection. *Biosens. Bioelectron.* **2014**, *59*, 140-144.
76. Yakovleva M., Bhand S., Danielsson B. The enzyme thermistor-A realistic biosensor concept. A critical review. *Anal. Chim. Acta* **2013**, *766*, 1-12.
77. Qie Z., Ning B., Liu M., Bai J., Peng Y., Song N., Lv Z., Wang Y., Sun S., Su X., Zhang Y., Gao Z. Fast detection of atrazine in corn using thermometric biosensors. *Analyst* **2013**, *138*, 5151-5156.
78. Saha B., Evers T.H., Prins M.W.J. How Antibody Surface Coverage on Nanoparticles Determines the Activity and Kinetics of Antigen Capturing for Biosensing. *Anal. Chem.* **2014**, *86*, 8158-8166.
79. Edwards, P.R., Leatherbarrow R.J. Determination of Association Rate Constants by an Optical Biosensor Using Initial Rate Analysis. Anal. Biochem. **1997**, *246*, 1-6.
80. Gonçalves A.M. Pedro A.Q., Santos F.M., Martins L.M., Maia C.J., Queiroz J.A., Passarinha L.A. Trends in Protein-Based Biosensor Assemblies for Drug Screening and Pharmaceutical Kinetic Studies. *Molecules* **2014**, *19*, 12461-12485.

81. Méjard R., Griesser H.J., Thierry B. Optical biosensing for label-free cellular studies. *Trends Anal. Chem.* **2014**, *53*, 178-186.
82. Chong S.S., Aziz A.R.A., Harun S.W. Fibre Optic Sensors for Selected Wastewater Characteristics. *Sensors* **2013**, *13*, 8640-8668.
83. Fenzl C., Hirsch T., Wolfbeis O.S. Photonic Crystals for Chemical Sensing and biosensing. *Angew. Chem. Int. Ed.* **2014**, *53*, 3318-3335.
84. Yáñez-Sedeño P., Agüí L., Villalonga R., Pingarrón J.M. Biosensors in forensic analysis. A review. *Anal. Chim. Acta* **2014**, *823*, 1-19.
85. Fracchiola N.S., Artuso S., Cortelezzi A. Biosensors in Clinical Practice: Focus on Oncohematology. *Sensors* **2013**, *13*, 6423-6447.
86. Kaushik A., Vasudev A., Arya S.K., Pasha S.K., Bhansali S. Recent advances in cortisol sensing technologies for point-of-care application. *Biosens. Bioelectron.* **2014**, *53*, 499-512.
87. British Patent 223994 (1923).
88. British Patent 290901 (1927).
89. Italian Patent 741753 (1936).
90. Keller F., Hunter M.S., Robinson D.L. Structural features of oxide coatings on aluminum. *J. Electrochem. Soc.* **1953**, *100*, 411-419.
91. Diggle J.W., Downie T.C., Coulding C.W. Anodic oxide films on aluminum. *Chem. Rev.* **1969**, *69*, 365-405.
92. O'Sullivan J.P., Wood G.C. The morphology and mechanism of formation of porous anodic films on aluminium. *Proc. R. Soc. Lon. Ser. A Math. Phys. Sci.* **1970**, *317*, 511-543.
93. Thompson G.E., Wood G.C. Porous anodic film formation on aluminum. *Nature* **1981**, *290*, 230-232.
94. Thompson G.E., Wood G.C. Anodic films on aluminum. *In treatise on materials science and technology* **1983**, *23*, Academic Press, New York.
95. Thompson G.E., Xu Y., Skeldon P., Shimizu K., Han S.H., Wood G.C. Anodic oxidation of aluminium, *Philos. Mag. B* **1987**, *55*, 651-667.

96. Shimizu K., Kobayashi K., Thompson G.E., Wood G.C. A novel marker for the determination of transport numbers during anodic barrier oxide growth on aluminium, *Philos. Mag. B* **1991**, *64*, 345-353.
97. Wood G.C., Skeldon P., Thompson G.E., Shimizu K. A model for the incorporation of electrolyte species into anodic alumina, *J. Electrochem. Soc.* **1996**, *143*, 74-83.
98. Skeldon, P., Thompson G.E., Wood G.C., Zhou X., Habazaki H., Shimizu K. Evidence of oxygen bubbles formed within anodic films on aluminium-copper alloys. *Philos. Mag. A* **1997**, *76*, 729-741.
99. Thompson, G.E., Porous anodic alumina: Fabrication, characterization and applications. *Thin Solid Films* **1997**, *297*, 192-201.
100. Masuda H., Fukuda K. Ordered metal nanohole arrays made by a two-step replication of honeycomb structures of anodic alumina. *Science* **1995**, *268*, 1466-1468.
101. Nielsch K., Choi J., Schwim K., Wehrspohn R.B., Gösele U. Self-ordering regimes of porous alumina: The 10% Porosity Rule. *Nano Lett.* **2002**, *2*, 677-680.
102. Lee W., Ji R., Gösele U., Nielsch K. Fast fabrication of long-range porous alumina membranes by hard anodization. *Nat. Mater.* **2006**, *5*, 741–747.
103. Lee W., Kim J.-C. Highly ordered porous alumina with tailor-made pore structures fabricated by pulse anodization. *Nanotechnology* **2010**, *21*, 485304.
104. Santos A., Vojkuvka L., Alba M., Valderrama V.S., Ferré-Borrull J., Pallarès J., Marsal L.F. Understanding and morphology control of pore modulations in nanoporous anodic alumina by discontinuous anodization. *Phys. Status Solidi A* **2012**, *209*, 2045–2048.

105. Zheng W.J., Fei G.T., Wang B., Jin Z., Zhang L.D. Distributed Bragg reflector made of anodic alumina membrane. *Mater. Lett.* **2009**, *63*, 706–708.

106. Su Y., Fei G.T., Zhang Y., Yan P., Li H., Shang G.L., Zhang L.D. Controllable preparation of the ordered pore arrays anodic alumina with high-quality photonic band gaps. *Mater. Lett.* **2011**, *65*, 2693–2695.

107. Rahman M.M., Marsal L.F., Pallarès J., Ferré-Borrull J. Tuning the photonic stop bands of nanoporous anodic alumina-based distributed Bragg reflectors by pore widening. *ACS Appl. Mater. Interfaces* **2013**, *5*, 13375–13381.

108. Yisen L., Yi C., Zhiyuan L., Xing H., Yi L. Structural coloring of aluminium. *Electrochem. Commun.* **2011**, *13*, 1336–1339.

109. Yan P., Fei G.T., Shang G.L., Wu B., Zhang L.D. Fabrication of one-dimensional alumina photonic crystals with a narrow band gap and their application to high-sensitivity sensors. *J. Mater. Chem. C* **2013**, *1*, 1659–1664.

110. Li F. Nanostructure of anodic porous alumina films of interest in magnetic recording. *The University of Alabama* **1998**.

111. Santos A. Structural engineering of nanoporous anodic alumina and applications. *LAP Lambert Academic Publishing* **2011**.

112. Hoar T.P., Mott N.F. A mechanism for the formation of porous anodic oxide films on aluminium. *J. Phys. Chem. Solids* **1959**, *9*, 97-99.

113. Patermarakis G., Lenas P., Karavassilis C.H., Papayiannis G. Kinetics of growth of porous anodic Al2O3 films on Al metal. *Electrochim. Acta* **1991**, *36*, 709-725.

114. Parkhutik V.P., Shershulsky V.I. Theoretical modelling of porous oxide growth on aluminum. *J. Phys. D: Appl. Phys.* **1992**, *25*, 1258-1263.

115. Patermarakis G., Papandreadis N. Study on the kinetics of growth of porous anodic Al2O3 films on Al metal. *Electrochim. Acta* **1993**, *38*, 2351-2361.

116. Patermarakis G., Tzouvelekis D. Development of a strict kinetic model for the growth of porous anodic Al2O3 films on Aluminium. *Electrochim. Acta* **1994**, *39*, 2419-2429.

117. Patermarakis G., Karayannis H.S. The mechanism of growth of porous anodic Al2O3 films on aluminium at high film thicknesses. *Electrochim. Acta* **1995**, *40*, 2647-2656.

118. Randon J., Mardilovich P.P., Govyadinov A.N., Paterson R. Computer simulation of inorganic membrane morphology Part 3 anodic alumina films and membranes. *J. Colloid Interface Sci.* **1995**, *169*, 335-341.

119. Patermarakis G., Transformation of the overall strict kinetic model governing the growth of porous anodic Al2O3 films on aluminium to a form applicable to the non-stirred bath film growth. *Electrochim. Acta* **1996**, *41*, 2601-2611.

120. Thamida S.K., Chang H.C. Nanoscale pore formation dynamics during aluminum anodization. *Chaos* **2002**, *12*, 240-251.

121. Pashchanka M., Schneider J.J. Origin of self-organization in porous anodic alumina films derived from analogy with Rayleigh-Bénard convection cells. *J. Mater. Chem.* **2011**, *21*, 18761-18767.

122. Pashchanka M., Schneider J.J. Experimental validation of the novel theory explaining self-organization in porous anodic alumina films. *Phys. Chem. Chem. Phys.* **2013**, *15*, 7070-7074.

123. Stepniowski W.J., Norek M., Michalska-Domanska M., Forbot D., Król A. Study on the correlation between criterion number derived from Rayleigh-Bénard convective cells and arrangement of nanoporous anodic aluminum oxide. *Mater. Lett.* **2014**, *125*, 124-127.

References

124. Chi J., Wherspohn R. B., Gösele U. Mechanism of guided self-organization producing quasi-monodomain porous alumina. *Electrochim. Acta* **2005**, *50*, 2591-2595.

125. Kwon N., Kim K., Heo J., Chung I. Fabrication of ordered anodic aluminum oxide with matrix arrays of pores using nanoimprint. *J. Vac. Sci. Technol. A* **2009**, *27*, 803-807.

126. Kustandi T. S., Loh W. W., Gao H., Low H. Y. Wafer-Scale Near-Perfect Ordered Porous Alumina on Substrates by Step and Flash Imprint Lithography. *ACSNano* **2010**, *4*, 2561-2568.

127. Montero-Moreno J. M., Waleczek M., Martens S., Zierold R., Görlitz D., Vega-Martínez V., Prida V. M., Nielsch K. Constrained Order in Nanoporous Alumina with High Aspect Ratio: Smart Combination of Interference Lithography and Hard Anodization. *Adv. Funct. Mater.* **2014**, *24*, 1857-1863.

128. Jessensky O., Muller F., Gösele U. Self-organized formation of hexagonal pore arrays in anodic alumina. *Appl. Phys. Lett.* **1998**, *72*, 1173–1175.

129. Li A. P., Muller F., Birner A., Nielsch K., U. Gösele U. Hexagonal pore arrays with a 50-420 nm interpore distance formed by self-organization in anodic alumina," J. Appl. Phys. 1998, 84, 6023–6026.

130. Chen W., Wu J.-S., Xia X.-H. Porous Anodic Alumina with Continuously Manipulated Pore/Cell Size. *ACS Nano* **2008**, *2*, 959-965.

131. Manzano C.V., Martín J., Martín-González M.S. Ultra-narrow 12 nm pore diameter self-ordered anodic alumina templates. *Micropor. Mesopor. Mat.* **2014**, *187*, 177-183.

132. Stepniowski W.J., Forbot D., Norek M., Michalska-Domanska M., Król A. The impact of viscosity of the electrolyte on the formation of nanoporous anodic aluminum oxide. *Electrochim. Acta* **2014**, *133*, 57-64.

133. Kim B., Lee J.S. Effect of Aluminum Purity on the Pore Formation of Anodic Alumina. *Bull. Korean Chem. Soc.* **2014**, *35*, 349-352.

134. Rahimi M.H., Tabaian S.H., Marashi S.P.H., Saramad S., Arab M., Hemasian A. Heat treatment of aluminum in preparing porous anodic alumina templates. *Micro Nano Lett.* **2012**, *7*, 125-129.

135. Alam K.M., Singh A.P., Bodepudi S.C., Pramanik S. Fabrication of hexagonally ordered nanopores in anodic alumina: An alternative pretreatment. *Surf. Sci.* **2011**, *605*, 441-449.

136. Santos A., Montero-Moreno J.M., Bachmann J., Nielsch K., Formentín P., Ferré-Borrull J., Pallarès J., Marsal L.F. Understanding Pore Rearrangement during Mild to Hard Transition in Bilayered Porous Anodic Alumina Membranes. *ACS Appl. Mater. Interfaces* **2011**, *3*, 1925-1932.

137. Santos A., Formentín P., Pallarès J., Ferré-Borrull J., Marsal L.F. Structural engineering of nanoporous anodic alumina funnels with high aspect ratio. *J. Electroanal. Chem.* **2011**, *655*, 73-78.

138. Nanoporous anodic alumina barcodes: Toward smart optical biosensors. *Adv. Mater.* **2012**, *24*, 1050-1054.

139. Santos A., Alba M., Rahman M.M., Formentín P., Ferré-Borrull J., Pallarès J., Marsal L.F. Structural tuning of photoluminescence in nanoporous anodic alumina by hard anodization in oxalic and malonic acids. *Nanoscale Res. Lett.* **2012**, *7*, 228.

140. Santos A., Balderrama V.S., Alba M., Formentín P., Ferré-Borrull J., Pallarès J., Marsal L.F. Tunable Fabry-Pérot interferometer base don nanoporous anodic alumina for optical biosensing purposes. *Nanoscale Res. Lett.* **2012**, *7*, 1-10.

141. Rahman M.M., García-Caurel E., Santos A., Marsal L.F., Pallarès J., Ferré-Borrull J. Effect of the anodization voltage on the pore-

widening rate of nanoporous anodic alumina. *Nanoscale Res. Lett.* **2012**, *7*, 474.

142. Macias G., Ferré-Borrull J., Pallarès J., Marsal L.F. 1-D nanoporous anodic alumina rugate filters by means of small current variations for real-time sensing applications. *Nanoscale Res. Lett.* **2014**, *9*, 315.

143. Du Y., Cai W.L., Mo C.M. Chen J., Zhang L.D., Zhu X.G. Preparation and photoluminescence of alumina membranes with ordered pore arrays. *Appl. Phys. Lett.* **1999**, *74*, 2951

144. Chen J.H., Huang C.P., Chao C.G., Chen T.M. the investigation of photoluminescence centers in porous alumina membranes. *Appl-Phys. A* **2006**, *84*, 297-300.

145. Li Z., Huang K. The effect of high-temperature annealing on optical properties of porous anodic alumina formed in oxalic acid. *Luminescence* **2007**, *22*, 355-361.

146. Li Z., Huang K. Optical properties of alumina membranes prepared by anodic oxidation process. *J. Lumin.* **2007**, *127*, 435-440.

147. Vrublevsky I., Jagminas A., Hemeltjen S., Goedel W.A. Effect of heat treatment on the structure of incorporated oxalate species and photoluminescent properties of porous alumina films formed in oxalic acid. *Appl. Surf. Sci.* **2008**, *254*, 7326-7330.

148. Wang J., Wang C.-W., Li S.-Y., Zhou F. The effect of oxalic and sulfuric ions on the photoluminescence of anodic aluminum oxide formed in a mixture of sulfuric and oxalic acid. *Appl. Phys. A* **2009**, *94*, 939-942.

149. Liu Y.-F- Tu Y.-F., Huang S.-Y., Sang J.-P., Zou X.-W. Effect of etch-treatment upon the intensity and peak position of photoluminescence spectra for anodic alumina films with ordered nanopore array. *J. Mater. Sci.* **2009**, *44*, 3370-3375.

150. Nee T.-E., Fang C.-H., Chen Y.-R., Wang J.-C., Fan P.-L., Jiang J.-A. Characterization of the anomalous luminescence properties from self-ordered porous anodic alumina with oxalic acid electrolytes. *Thin Solid Films* **2009**, *518*, 1439-1442.

151. Vrublevsky I., Jagminas A., Hemeltjen S., Goedel W.A. Photoluminescent behavior of heat-treated porous alumina films formed in malonic acid. *Appl. Surf. Sci.* **2010**, *256*, 2013-2017.

152. Mukhurov N.I., Zhvavyi S.P., Gasenkova I.V., Terekhov S.N., Pershukevich P.P., Orlovich V.A. Photoluminescence of F-enters in films of anodic alumina. *J. Appl. Spectrosc*. **2010**, *77*, 549-555.

153. Vrublevsky I., Chernyakova K., Ispas A., Bund A., Gaponik N., Dubavik A. Photoluminescence properties of heat-treated porous alumina films formed in oxalic acid. *J. Lumin.* **2011**, *131*, 938-942.

154. Santos A., Alba M., Rahman M.M., Formentín P., Ferré-Borrull J., Pallarès J., Marsal L.F. Structural tuning of photoluminescence in nanoporous anodic alumina by hard anodization in oxalic and malonic acids. *Nanoscale Res. Lett.* **2012**, *7*, 228.

155. Santos A., Balderrama V.S., Alba M., Formentín P., Ferré-Borrull J., Pallarès J., Marsal L.F. Nanoporous Anodic Alumina Barcodes: Toward Smart Optical Biosensors. *Adv. Mater.* **2012**, *24*, 1050-1054.

156. Wu H., Yang J., Cao S., Huang L., Chen L. Ordered Organic Nanostructures Fabricated from Anodic Alumina Oxide Templates for Organic Bulk-Heterojunction Photovoltaics. *Macromol. Chem. Phys.* **2014**, *215*, 584-596.

157. Chahrour K.M., Ahmed N.M., Hashim M.R., Elfadill N.G., Qaeed M.A. Controllable fabrication of highly ordered thin AAO template on Si substrate for electrodeposition of nanostructures. *Appl. Phys. A* **2014**, In press.

158. Zhan Z., Lei Y. Sub-100-nm Nanoparticle Arrays with Perfect Ordering and Tunable and Uniform Dimensions Fabricated by Combining Nanoimprinting with Ultrathin Alumina Membrane Technique. *ACSNano* **2014**, *8*, 3862-3868.

159. Martin C.R., Siwy Z. Molecular filters: Pores within pores. *Nat. Mater.* **2004**, *3*, 284-285.

160. Osmanbeyoglu H.U., Hur T.B., Kim H.K. Thin alumina nanoporous membranes for similar size biomolecule separation. *J. Membrane Sci.* **2009**, *343*,1-6.

161. Wang L., Tran T.P., Vo D.V., Sakurai M., Kameyama H. Design of novel Pt-structured catalyst on anodic aluminum support for VOC's catalytic combustion. *Appl. Catal. A Gen.* **2008**, *350*, 150-156.

162. Zhou L., Guo Y., Yagi M., Sakurai M., Kameyama H. Investigation of a novel porous anodic alumina plate for methane steam reforming: Hydrothermal stability, electrical heating possibility and reforming reactivity. *Int. J. Hydrogen Energ.* **2009**, *34*, 844-858.

163. Wang Y., Santos A., Kaur G., Evdokiou A., Losic D. Structurally engineered anodic alumina nanotubes as nano-carriers for delivery of anticancer therapeutics. *Biomaterials* **2014**, *35*, 5517-5526.

164. Kumeria T., Santos A., Losic D. Nanoporous Anodic Alumina Platforms: Engineered Surface Chemistry and Structure for Optical Sensing Applications. *Sensors* **2014**, *14*, 11878-11918.

165. Ferré-Borrull J., Pallarès J., Macias G., Marsal L.F. Nanostructural Engineering of Nanoporous Anodic Alumina for Biosensing Applications. *Materials* **2014**, *7*, 5225-5253.

166. Kant K., Low S.P., Marshal A., Shapter J.G., Losic D. Nanopore Gradients on Porous Aluminum Oxide Generated by Nonuniform Anodization of Aluminum. *ACS Appl. Mater. Interfaces* **2010**, *2*, 3447-3454.

167. Hu J., Tian J.H., Shi J., Zhang F., He D.L., Liu L., Jung D.J., Bai J.B., Chen Y. Cell culture on AAO nanoporous substrates with and without geometry constrains. *Microelectron. Eng.* **2011**, *88*, 1714-1717.

168. Poinern G.E.J., Shackleton R., Mamun S.I., Fawcett D. Significance of novel bioinorganic anodic aluminum oxide nanoscaffolds for promoting cellular response. *Nanotechnol. Sci. Appl.* **2011**, *4*, 11-24.

169. Piehler J., Brecht A., Gauglitz G. Affinity Detection of Low Molecular Weight Analytes. *Anal. Chem.* **1996**, *68*, 139-143.

170. Tinsley-Bown, A. M.; Canham, L.T.; Hollings, M.; Anderson, M.H.; Reeves, C.L.; Cox, T.I.; Nicklin, S.; Squirrell, D.J.; Perkins, E.; Hutchinson, A.; Sailor, M. J.; Wun, A. Tuning the Pore Size and Surface Chemistry of Porous Silicon for Immunoassays. *Phys. Stat. Sol. (a)* **2000**, *182*, 547-553.

171. Hotta, K.; Yamaguchi, A.; Teramae, N. Properties of A Metal Clad Waveguide Sensor Based on A Nanoporous-Metal-Oxide/Metal Multilayer Film. *Anal. Chem.* **2010**, *82*, 6066-6073.

172. Kumeria, T.; Losic, D. Controlling interferometric properties of nanoporous anodic aluminium oxide. *Nanoscale Res. Lett.* **2012**, *7*, 88-10.

173. Macias G., Ferré-Borrull J., Pallarès J., Marsal L.F., Effect of pore diameter in nanoporous anodic alumina optical biosensors. *Analyst*, **2015**, DOI: 10.1039/C4AN01408A

174. Lazzara T.D., Mey I., Steinem C., Janshoff A. Benefits and limitations of porous substrates as biosensors for protein adsorption. *Anal. Chem.*, **2011**, *83*, 5624-5630.

175. Joshi S., Pellacani P., Van Beek T.A., Zuilhof H., Nielen M.W.F. Surface characterization and antifouling properties of nanostructured gold chips for imaging surface plasmon resonance biosensing. *Sens. Actuat. B Chem.*, **2015**, *209*, 505-514.

176. Hernández-Eguía L.P., Ferré-Borrull J., Macias G., Pallarès J., Marsal L.F. engineering optical properties of gold-coated nanoporous anodic alumina for biosensing. *Nanoscale Res. Lett.* **2014**, *9*, 414.

177. Ahmad N., Stokes J., Fox N.A., Teng M., Cryan M.J. Ultra-thin metal films for enhanced solar absorption. *Nano Energy*, **2012**, *1*, 777-782.

178. Macias G., Hernández-Eguía L.P., Ferré-Borrull J., Pallarès J., Marsal L.F. Gold-Coated Ordered Nanoporous Anodic Alumina Bilayers for Future Label-Free Interferometric Biosensors. *ACS Appl. Mater. Interfaces* **2013**, *5*, 8093-8098.

179. Pacholski C., Sartor M, Sailor M.J., Cunin F., Miskelly G.M. Biosensing using porous silicon double-layer interferometers: Reflective interferometric Fourier transform spectroscopy. *J. Am. Chem. Soc.*, **2005**, *127*, 11636-11645.

180. Jani A.M.M., Kempson I.M., Losic D., Voelcker N.H. Dressing in layers: Layering surface functionalities in nanoporous aluminum oxide membranes. *Angew. Chem.-Int. Ed.* **2010**, *49*, 7933-7937.

181. Gutenwik J., Nilsson, B. Axelsson A. Effect of hindered diffusion on the adsorption of proteins in agarose gel using a pore model. *J. Chromatogr. A*, **2004**, *1046*, 161-172.

182. Alvarez S.D., Li C.-P., Chiang C.E., Schuller I.K., Sailor M.J. A Label-Free Porous Alumina Interferometric Immunosensor. *ACS Nano*, **2009**, *3*, 3301-3307.

183. Lorenzo E., Oton C.J., Capuj N.E., Ghulinyan M., Navarro-Urrios D., Gaburro Z., Pavesi L. Porous silicon-based rugate filters. *Appl. Optics*, **2005**, *44*, 5415-5421.

184. Orosco M. M., Pacholski C. Miskelly M., Sailor M.J.: Protein-coated porous silicon photonic crystals for amplified optical detection of protease activity. *Adv. Mater.,* **2006**, *18,* 1393-1396.

185. Pacholski C., Sailor M. J.: Sensing with porous silicon double layers: a general approach for background suppression. *Phys. Stat. Sol. C*, **2007**, *4*, 2088-2092.

186. Salem M. S., Sailor M. J., Fukami K., Sakka T., Ogata Y. H.: Sensitivity of porous silicon rugate filters for chemical vapour detection. *J. Appl. Phys.*, **2008**, *103*, 083516-7.

187. Ruminski A. M., King B. H., Salonen J., Snyder J. L., Sailor M. J.: Porous silicon-based optical microsensors for volatile organic analytes: Effect of surface chemistry on stability and specificity. *Adv. Funct. Mater.*, **2010**, *20*, 2874-2883.

188. Kelly T. L., Gao T., Sailor M. J.: Carbon and carbon/silicon composites templated in rugate filters for the adsorption and detection of organic vapors. *Adv. Mater.*, **2011**, *23*, 1776-1781.

189. Li S., Hu D., Huang J., Cai L.: Optical sensing nanostructures for porous silicon rugate filters. *Nanoscale Res. Lett.*, **2012**, *7*, 79.

References

PUBLICATIONS RELATED TO THIS THESIS

Santos A., Macias G., Ferré-Borrull J., Pallarès J., Marsal L.F. Photoluminescent Enzymatic Sensor Base don Nanoporous Anodic Alumina. *ACS Appl. Mater. Interfaces* **2012**, *4*, 3584-3588.

Macias G., Hernández-Eguía L.P., Ferré-Borrull J., Pallarès J., Marsal L.F. Gold-Coated Ordered Nanoporous Anodic Alumina Bilayers for Future Label-Free Interferometric Biosensors. *ACS Appl. Mater. Interfaces* **2013**, *5*, 8093-8098.

Macias G., Ferré-Borrull J., Pallarès J., Marsal L.F. 1-D nanoporous anodic alumina rugate filters by means of small current variations for real-time sensing applications. *Nanoscale Res. Lett.* **2014**, *9*, 315.

Baranowska M., Slota A.J., Eravuchira P.J., Macias G., Xifré-Pérez E., Pallarès J., Ferré-Borrull J., Marsal L.F. Protein attachment to nanoporous anodic alumina for biotechnological applications: Influence of pore size, protein size and functionalization path. *Colloid Surface* B **2014**, *122*, 375-383.

Ferré-Borrull J., Pallarès J., Macias G., Marsal L.F. Nanostructural Engineering of Nanoporous Anodic Alumina for Biosensing Applications. *Materials* **2014**, *7*, 5225-5253.

Hernández-Eguía L.P., Ferré-Borrull J., Macias G., Pallarès J., Marsal L.F. engineering optical properties of gold-coated nanoporous anodic alumina for biosensing. *Nanoscale Res. Lett.* **2014**, *9*, 414.

Publications related to this thesis

Macias G., Ferré-Borrull J., Pallarès J., Marsal L.F., Effect of pore diameter in nanoporous anodic alumina optical biosensors. *Analyst*, **2015**, DOI: 10.1039/C4AN01408A

CONFERENCES

Hernndez-Eguía´L.P., Macias G., Ferré-Borrull J., Marsal L.F. Tailoring the optical properties of nanoporous anodic alumina with geometry modification for further sensing applications. *Conferencia Española de Nanofotónica*, **2012**.

Macias G., Hernández-Eguía L.P., Ferré-Borrull J., Pallarès J., Formentin P., Marsal L.F. Fabrication and characterization of nanoporous anodic alumina bi-layers for biosensing applications. *Conferencia Española de Nanofotónica*, **2012**.

Marsal L.F., Santos A., Formentin P., Hernández L., Macias G., Alba M., Pallares J., Ferré-Borrull J. Structural engineering of micro and nanoporous silicon and nanoporous alumina for biosensing applications. *Conferencia Española de Nanofotónica*, **2012**.

Marsal L.F., Santos A., Formentin P., Granero P., Macias G., Alba M., Pallares J., Ferre-Borrull J. Architectural design of nanoporous anodic materials for bio-technological Applications. *7th International Conference on Optical, Optoelectronic and Photonic Materials and Applications*, **2012**.

Macias G., Ferré-Borrull J., Pallarès J., Marsal L.F. Highly reflective UV-blue band in nanoporous anodic alumina rugate filters. *Porous Semiconductors-Science and Technology*, **2014**.

Marsal L.F., Alba M., Macias G., Formentin P., Ferré-Borrull J. Label-Free and Real-Time Photonic Sensors As Analytical Platforms for Environmental Monitoring of Pollutants and Medical Diagnosis. *225th ECS Meeting*, **2014**.

Conferences

LIST OF FIGURES

List of figures

LIST OF TABLES